

Dissertation

submitted to the
Combined Faculty of Mathematics, Engineering and Natural Sciences of
Heidelberg University, Germany
for the degree of
Doctor of Natural Sciences

Put forward by:

Ting Cheng

Born in: Taipei, Taiwan

Oral examination: 07.12.2023

Neutrino Coherence and Decoherence in Terrestrial and Astrophysical Environments

Referees: Prof. Dr. Dr. h.c. Manfred Lindner
Prof. Dr. Jörg Jäckel

Abstract

This thesis explores how neutrinos may serve as a portal to effects in the quantum regime. Due to the smallness of neutrino masses and its feebly interacting feature, the neutrino system acts as a closed quantum system at a macroscopic scale. Nonetheless, as the precision of neutrino oscillation experiments increases, a closed quantum system description would become insufficient at some point, and a door to effects in the quantum regime through decoherence signatures would be open up. In order to sift the fundamental, quantum signal from the classical noise in the future detection, a more consistent machinery warrants development. For this purpose, we incorporate the concept of open quantum systems into the quantum field theory description of neutrino oscillations. As a result, we present a generic structure (introduced as the layer structure) for decoherence effects in neutrino oscillations, showing how decoherence signatures from quantum effects and classical uncertainties may be interpreted as phase wash-out effects on different layers with different phase structures. On the other hand, additional coherence could come into play when interactions with a low momentum transfer are included. In addition, we explore the expanded coherence due to the interaction with magnetic field, which flips the chirality of the neutrino through the theoretically motivated magnetic moment effect. For high energy neutrinos, such effect can be sizeable as some of them are likely to be produced in a highly magnetized region. By adopting a simple model aiming to investigate the imprints of magnetic moment effect on the neutrino flux generated from the particle collisions nearby a magnetar, possible signatures with the IceCube observatory is speculated and discussed.

Zusammenfassung

In dieser Arbeit wird untersucht, wie Neutrinos als Portal zu Effekten im Quantenbereich dienen können. Aufgrund der geringen Masse der Neutrinos und der Tatsache, dass sie nur über die schwache Wechselwirkung interagieren, entspricht das Neutrinosystem auf makroskopischer Ebene einem geschlossenen Quantensystem. Mit zunehmender Präzision der Neutrinooszillationsexperimente würde eine Beschreibung als geschlossenes Quantensystem jedoch irgendwann nicht mehr ausreichen und es würde sich eine Tür zu Effekten im Quantenbereich durch Dekohärenzsignaturen öffnen. Wir integrieren das Konzept offener Quantensysteme in die quantenfeldtheoretische Beschreibung von Neutrinooszillationen. Als Ergebnis stellen wir eine generische Struktur (die Schichtstruktur) für Dekohärenzeffekte in Neutrinooszillationen vor und zeigen, wie Dekohärenzsignaturen aus Quanteneffekten und klassischen Unsicherheiten als Phasenauswaschungseffekte auf verschiedenen Schichten mit unterschiedlichen Phasenstrukturen interpretiert werden können. Andererseits könnte zusätzliche Kohärenz ins Spiel kommen, wenn Wechselwirkungen mit geringem Impulstransfer einbezogen werden. In dieser Arbeit untersuchen wir auch die erweiterte Kohärenz aufgrund der Wechselwirkung mit einem Magnetfeld, das die Chiralität des Neutrinos durch den theoretisch motivierten magnetischen Momenteneffekt umkehrt. Insbesondere untersuchen wir die Erwartung eines solchen Effekts für hochenergetische Neutrinos astrophysikalischen Ursprungs, da sie eng mit den Magnetfeldanforderungen für die Teilchenbeschleunigung verbunden ist.

Contents

Disclaimer	vii
Acknowledgements	ix
1 Introduction	1
2 Neutrino Coherence and Decoherence Formalisms	7
2.1 Closed Quantum System	7
2.1.1 Flavour Transition	8
2.1.2 Helicity Flip by Neutrino Magnetic Moment	8
2.1.3 Length-scales	10
2.1.4 Anti-symmetric Hamiltonian	11
2.2 Open Quantum System	12
2.2.1 Formalisms for Neutrino Decoherence	14
2.2.2 The Quantum Field Theory Formalism	15
3 The Layer Structure	23
3.1 Microscopic Layer (Layer 1): QFT Transition Amplitude	28
3.2 Microscopic Layer (Layer 1): Quasi-Transition Probability	31
3.3 Physical Layer (Layer 2): Transition Probability	34
3.4 Measurement Layer (Layer 3): Transition Probability	38
4 Neutrino Decoherence Signatures	43
4.1 Classification of Decoherence-like Signatures	44
4.1.1 Formalism	44
4.1.2 State Decoherence	47
4.1.3 Phase Decoherence	54
4.2 Spectral Analysis	58
4.2.1 Reactor Neutrinos	60
4.3 A Phase Measuring Proposal	63
4.3.1 The Set Up	64
4.3.2 Decay at Rest Neutrinos	67

5 High Energy Neutrino Magnetic Moment	73
5.1 Production of High Energy Neutrinos	75
5.1.1 Systems involving a magnetar	78
5.1.2 Magnetic Field Structure and Numerical Results	80
5.2 Neutrino Magnetic Moment Effect	84
5.2.1 Signatures at IceCube	89
6 Conclusions	93
A Fourier Transformation and Convolution Properties	97
B Factorization Condition	101
C Phase Decoherence for Discrete Neutrino Sources	103

Disclaimer

This thesis is based on two papers with the original research performed by the author in collaboration with others. In particular:

- The results of Chapter 3 and 4 are based on Reference [1], in collaboration with Manfred Lindner and Werner Rodejohann.
- The results of Chapter 5 are based on a paper currently in the finalisation process, which is in collaboration with Vedran Brdar, Hao-Jui Kuan and Yingying Li.

Another paper published in peer-reviewed journals developed during my time as a PhD student is Reference [2], in collaboration with Manfred Lindner and Manibrata Sen.

Acknowledgements

I would first like to thank my supervisors at the Max-Planck-Institut für Kernphysik: Werner Rodejohann and Manfred Lindner. Without their invaluable guidance and support of all its forms, I would have not fulfilled my thesis. I was very naive when I started my PhD, and would particularly like to thank Werner for integrating me into the field. I remember on my first day at the institute, Manfred told me that the goal is to find what I am good at and excel in that area, and at the end of the day, be able to look myself in the mirror and know what I want to do. I would like to thank him for the guidance and providing an idea environment for this journey. I would also like to thank Jörg Jäckel, who has been my internal supervisor at the University of Heidelberg, for keeping track of my progress. I am also indebted to Martin Spinrath, my advisor for my pre-doctoral studies, for introducing me into the field and helping me find my passion. I have my gratitude to my collaborators, Vedran Brdar, Hao-Jui Kuan, Yingying Li, Manibrata Sen, Vishnu PK and Jisuke Kubo for the fruitful discussions. I also appreciate Yi Chung, Hao-Jui, Nele Volmer, Manibrata, Salva Centelles Chulia and Tim Herbermann for proof reading this thesis. A special thanks to Nele for providing a German translation of the abstract, and being wonderful and supportive officemate. I would also like to show appreciation to my mother, father and brother for providing the warm support system. Finally, I would like to thank my partner, Hao-Jui, for his pouring many physics insights to me when we pondering the universe together, and for those discussions concerning both works and life with him.

Terminology

Phase space (PS) variables

Three coordinate variables, three momentum variables (composing the six-dimension PS) and a temporal variable.

Layer structure

Composed of three layers (layer 1-3) from the microscopic Hilbert space to the macroscopic measurement space, where all spaces are represented by PS variables. The structure is illustrated in Chapter 3, and its value of providing a simple and generic picture of decoherence effects is shown in Chapter 4.

Layer-Moving-Operator (LMO)

Operators moving some physical quantity up one layer, characterised by some weighting functions on the lower layer. The definition is given in Eq. (3.1).

Microscopic layer (layer 1)

Configurations of fundamental theories are described on this layer, such as the Feynman diagram, and intrinsic quantum mechanical uncertainties. More explanations are given in Section 3.1 and Section 3.2.

Physical layer (layer 2)

As an intermediate layer between the fundamental theories and experimental measurements, this layer describe the statistical ensemble. On top of quantum uncertainties brought up from the first layer, this layer also include uncertainties due to a lack of knowledge. More explanations are given in Section 3.3.

Measurement layer (layer 3)

This layer describes realistic experimental measurements including effects such as energy resolution. Examples are given in Section 3.4.

Fock phase space (Fock-PS)

A representation of layer 1 where the occupation of the PS is written in terms of Fock states. The case for neutrino oscillations calculated by QFT is demonstrated in Section 3.1.

Wigner phase space (Wigner-PS)

A representation of layer 1 where the occupation of the PS is written in terms of Wigner quasi-probability distributions. More explanations are given in Section 3.2.

Relativistic phase space (Relativistic-PS)

A representation of layer 2, by taking the expectation values of the PS variables on the first layer assuming a relativistic system (e.g. massless neutrinos). The case for neutrino oscillation is demonstrated in Section 3.3.

Measurement phase space (Measurement-PS)

A representation of layer 3, given by PS variables from experimental measurement.

Weighting function

Localized distributions that characterise uncertainties included in the LMO. Examples of uncertainties from layer 1 and layer 2 for neutrino oscillation are summarized in Section 4.1.2 and Section 4.1.3, respectively.

Phase wash-out (PWO) effect

An averaging effect which washes out oscillation signatures by introducing a damping term and a phase shift term. Mathematical formalism and properties are given in Appendix A.

Uncertainty parameters (σ_n)

Widths of the weighting functions w.r.t. some PS variable n which parameterize decoherence signatures. Some analysing methods, as well as its sensitivity estimation of three relevant uncertainty parameters are shown in Section 4.2 for neutrino oscillation experiments.

State decoherence (SD)

Decoherence by the separation of superposition states on the physical layer, which is equivalent to a PWO effect on the Wigner-PS under a factorisation condition (see Appendix B) and is dominated by uncertainties on layer 1 (see Section 4.1.2).

Phase decoherence (PD)

Decoherence by the PWO effect on the physical layer dominated by the macroscopic uncertainties on layer 2 (see Section 4.1.3).

Chapter 1

Introduction

Neutrinos are like the late bloomers in physics due to their unique properties. Since it is nearly invisible, it didn't exist in the eyes of physicists until Pauli "invented" them in 1930 to preserve energy-momentum conservation in beta decay. For the same reason, it took another 26 years before they were directly observed. Furthermore, due to the absence of neutrino masses in the standard model (SM) renormalizable terms, neutrinos were long treated as massless particles until the observation of neutrino oscillations around the beginning of the 21st century. These properties are also why neutrinos could play a crucial role in advancing high energy physics. This statement will be elaborated upon in terms of theoretical motivation, followed by probes through quantum information and astrophysics in this section. On the other side of the coin, neutrinos may also contribute to our understanding of quantum mechanics and the development of astrophysics.

Features from existing measurements of neutrino properties, such as their masses and the leptonic mixing matrix (i.e., the Pontecorvo–Maki–Nakagawa–Sakata, or PMNS matrix), have been considered indications of beyond standard model (BSM) physics at a high energy scale (see, e.g., [3] for a review). Dissatisfaction arises from the fact that if neutrinos were Dirac particles with masses generated through the same Higgs vacuum expectation value (vev) as other SM particles, their Yukawa coupling would need to be at least six orders of magnitude smaller than that of the lightest charged fermions. In the context of effective field theory, massive degrees of freedom at the high scale are integrated out, resulting in a suppression effect at low energies imposed by the high energy scale. When expanding over $1/\Lambda$, where Λ represents the scale of some unknown new physics, the lowest order non-renormalizable term with $d = 5$ would be the unique Weinberg operator, responsible for generating Majorana masses. Numerous models, such as the celebrated (three types of) seesaw models that generate neutrino masses at the tree level, as well as radiative models generating neutrino mass at the loop level, fall into this category [4]. Furthermore, in the spirit of reducing the randomness of parameters in a bigger picture, one may expand to the lepton sector (or even further to the entire fermion sector). In addition

to explaining the hierarchy among leptonic masses, the structure of the obviously-non-diagonal PMNS matrix also needs to be addressed. This is known as the flavor puzzle. Solving the flavor puzzle in addition, would indicate a more unified and comprehensive theory. It would also provide intermediate points for a bottom-up/top-down approach to unified theories [5]. In addition, note that there are other measured neutrino properties and their implications not covered here, such as the effective number of neutrino families in cosmology and their abundance in the universe.

The unique features of neutrinos enable them to evolve as a closed quantum system on a macroscopic scale. Consequently, the interference pattern of quantum coherence arising from the misalignment of the mass basis and the flavor (or interaction) basis has been extensively studied in neutrino oscillation experiments across a wide range of energies, involving multiple sources. Based on current data, neutrino sources can be classified as either fully coherent or fully decoherent at the detection site. The former category includes all terrestrial and atmospheric sources, and their coherence properties have been verified by introducing a damping factor $\exp(-\gamma_{jk})$ when fitting current oscillation data, [6–8]. Here, $\gamma_{jk} \propto \Delta m_{jk}^2 L^n / E^m$, and $\exp(-\gamma_{jk})$ suppresses the interference pattern between the j th and k th mass eigenstates. For decoherence resulting from wavepacket (WP) separation, the values are $m = 2$ and $n = 4$. Additionally, according to the Lindblad equation (Eq. (2.27)) and under certain assumptions, such as having a single scaling parameter for all decoherence effects and no energy or neutrino loss, we have $m = 1$, while n can remain a free parameter for a power-law fit. In contrast, neutrinos originating from astrophysical or cosmic sources are considered fully decohered due to WP separation. To elaborate, in order for an interference pattern to occur from the superposition of mass eigenstates, there must be a minimal energy uncertainty, as discussed in Section 3.3. This uncertainty imposes an upper limit on the size of the wavepackets []. Consequently, as different mass eigenstates travel at different group velocities, the WPs become fully separated over cosmic distances.

The study of decoherence was initiated in 1970 by H.D. Zeh here in Heidelberg to address the problem of "how to describe classical phenomena in the framework of quantum theory" [9]. Since then, it has been extensively developed to understand the emergence of classicality within the quantum framework (see, e.g., [10–12] for a review). Decoherence has been observed in various systems, including photon states in a cavity, matter-wave interferometry, superconducting systems, and ion traps [11]. The typical experimental challenges involve: 1) Creating a macroscopic superposition state to start with. 2) Ensuring that decoherence is not too fast, allowing the gradual process to be observed. 3) Minimizing unwanted decoherence, such as that caused by closely monitoring the system. For neutrinos, due to their unique features, the challenges are the other way around. It is impossible to produce a macroscopically coherent state for neutrinos, and artificial decoherence from monitoring is basically unattainable. Hence, the main obstacle is that the decoherence of neutrinos is not fast enough. In a way, this is also why neutrinos may be a late bloomer in terms of decoherence, since these challenges can be overcome by reducing statistical and/or systematic uncertainties. Once the required sensitivity

is achieved, it could open up a vast observational landscape for quantum effects. This statement is demonstrated in Chapter 4, where we address the question of “how much more statistics is needed if quantum decoherence appears at a certain scale” by manually reducing statistical uncertainties in the analysis while assuming a true decoherence scale. On the other hand, the requirement of systematic uncertainties can be answer by whether we will be able to identify decoherence signatures between quantum uncertainties and classical uncertainties.

The theoretical development for neutrino decoherence in this work (Section 2.2 - 4.1) aims to investigate the potential of probing quantum effects through decoherence tomography, which involves observing decoherence signatures over a range of E_0 and L_0 . Here, E_0 represents the observed energy of the neutrinos, and L_0 is the length of the baseline. To describe quantum effects at a fundamental level, we work within the framework of quantum field theory, making it more suitable for testing new physics, e.g., [13,14]. As decoherence effect results from leaking information to the environment in an open quantum system, would be convenient to view it as a quantum version of statistical mechanics. In fact, the Wigner quasi-probability distribution, which maps density matrix states onto a phase space, allows us to visualize quantum decoherence as a statistical effect. This will be referred to as state decoherence in Section 4.1. Furthermore, classical uncertainties also lead to decoherence signatures, and these are classified as phase decoherence in Section 4.1. The summary provided above motivates us to construct a layered structure in Chapter 3, comprising phase spaces ranging from a quantum (microscopic) level to a classical (macroscopic) level. The neutrino system is described within a quantum field theory framework at the quantum level (layer 1), and it can be mapped to a Wigner quasi-probability distribution (also at layer 1). By applying the open quantum system concept of integrating our the environment, we can move up to the classical level (layer 2) where classical uncertainties come into play. Finally, we present decoherence tomography at the observational level (layer 3) after statistical averaging. Experimental realization may involve constraining the range of E_0 and L_0 while implementing the analysis method. Two examples are provided in Section 4.2 and 4.3.

While neutrinos with an astrophysical origin become fully decohered upon their arrival at Earth, they can still carry information about additional coherence effects near their source. Specifically, the presence of an additional coherence effect, such as the coherent forward scattering effect (known as the Mikheyev-Smirnov-Wolfenstein or MSW effect), can cause the energy eigenstates to deviate from alignment with the mass eigenstates. This results in an energy-dependent variation in the flavor ratio detected at Earth. A prominent example of this effect is the observed oscillation pattern of solar neutrinos with respect to their energy. Moreover, astrophysical sources can provide extreme environments that are unattainable on Earth. Therefore, taking advantage in terms of extreme magnetic energy density, we focus on neutrinos above 100 TeV in Chapter 5. This energy threshold is chosen for two reasons: 1) it ensures an astrophysical source because atmospheric neutrinos cannot reach such high energies, and 2) it guarantees the presence of an effectively large magnetic field, which is a requirement for particle acceleration. As these neutrinos propagate in a effectively large magnetic field environment, they may gain

additional coherence, similar to the MSW effect, from the neutrino magnetic moment (ν MM) effect. However, unlike the MSW effect, this effect enhances the degree of freedom because the ν MM induces a chirality flip in the neutrinos. In the standard three-neutrino scenario, the degree of freedom expands from 3 (e.g., three flavors or masses) to $3 \otimes 2$ for Majorana neutrinos, and $3 \otimes 4$ for Dirac neutrinos. Consequently, this effect impacts the flavor and helicity structure detectable at Earth.

In the particle physics point of view, signatures of the flavour + helicity structure of these high energy neutrinos could provide information about 1) the Dirac or Majorana Nature of neutrinos and, 2) the ν MM. The former is because only half the coherent degree of freedom (the left-handed half) is detectable for Dirac neutrinos, while the complete set of degrees of freedom are detectable for Majorana neutrinos. Knowing whether neutrinos are Dirac or Majorana not only determines the first step of constructing a mechanism to generate neutrino mass, it also tells if lepton number is violated. For Majorana neutrinos, the generation of both the neutrino mass and the magnetic moment would violate lepton number by two units, which is a feature favored by grand unification theories as well as models addressing the baryon asymmetry of the Universe through leptogenesis. As for ν MM, since neutrinos are charge-less, it is typically generated at loop level. Furthermore, it has a tight connection with neutrino mass due to having a similar (chiral) structure in the effective field theory Lagrangian. For instance, without non-trivial model building, removing the photon line in a diagram generating ν MM would result in a diagram generating neutrino mass. Benchmark points of ν MM include: Dirac neutrinos for the simplest extension of the SM implies $\mu_\nu \simeq 3 \times 10^{-19} (m_\nu/\text{eV}) \mu_B$ and the current upper bound from terrestrial experiments $\mu_\nu < 10^{-12} \mu_B$. On the other hand, in the astrophysics point of view, these signature could also provide information about the source. For example, acceleration and cooling mechanism through their relation with the magnetic field strength. However, such effect will also increase the uncertainty for determining the collision processes through tracing back the neutrino's initial flavour state through the flavour ratio and/or Glashow resonance signatures.

In the context of particle physics, the flavor and helicity signatures of these high-energy neutrinos offer valuable insights into determining the Dirac or Majorana Nature of neutrinos and the value of ν MM. The former is because only half the coherent degree of freedom (the left-handed half) is detectable for Dirac neutrinos, while the complete set of degrees of freedom are detectable for Majorana neutrinos. Knowing whether neutrinos are Dirac or Majorana not only guides the initial steps in constructing mechanisms for generating neutrino mass but also provides insight into whether lepton number conservation is violated. In the case of Majorana neutrinos, the generation of both neutrino mass and the magnetic moment results in a violation of lepton number by two units. This is a feature favored by grand unification theories as well as models addressing the baryon asymmetry of the Universe through leptogenesis. Knowing whether neutrinos are Dirac or Majorana not only determines the first step of constructing a mechanism to generate neutrino mass, it also tells if lepton number is violated. For Majorana neutrinos, the generation of both the neutrino mass and the magnetic moment would violate

lepton number by two units, which is a feature favored by grand unification theories as well as models addressing the baryon asymmetry of the Universe through leptogenesis. As for ν MM, since neutrinos are charge-less, it is typically generated at loop level. Additionally, it shares a close connection with neutrino mass due to its analogous (chiral) structure in the effective field theory Lagrangian. For instance, without non-trivial model building, removing the photon line in a diagram generating ν MM would result in a diagram generating neutrino mass. Benchmark points of ν MM include: Dirac neutrinos for the simplest extension of the SM implies $\mu_\nu \simeq 3 \times 10^{-19} (m_\nu/\text{eV}) \mu_B$; the present upper bound from terrestrial experiments places μ_ν at less than $10^{-12} \mu_B$. From an astrophysical perspective, these signatures also offer insights into the source of these high-energy neutrinos. They can provide information about the acceleration and cooling mechanisms, particularly in relation to the strength of the magnetic field. However, such effects will also increase the uncertainty when attempting to determine collision processes by tracing back the initial flavor state of the neutrinos using the flavor ratio and/or Glashow resonance signatures.

Chapter 2

Neutrino Coherence and Decoherence Formalisms

Contents

2.1 Closed Quantum System	7
2.2 Open Quantum System	12

2.1 Closed Quantum System

The state of a neutrino can be characterized using the density matrix $\rho = |\nu\rangle\langle\nu|$. The choice of basis for the neutrino state ($|\nu\rangle$) depends on the basis neutrinos interact and propagate on. When neutrinos evolve as a closed quantum system, their dynamics are governed by the Liouville-von Neumann equation:

$$\frac{d}{dt}\rho(t) = i[\mathcal{H}(t), \rho(t)]. \quad (2.1)$$

This equation applies whether we consider the system in the coordinate basis or the momentum basis. In a closed quantum system, there is no loss of information. Consequently, the Hamiltonian operator \mathcal{H} , which may include both kinematic and potential energy terms, suffices to completely describe the neutrino's evolution. In this scenario, quantum coherence is preserved by the unitarity of the time evolution operator. In simpler terms, to maintain coherence, it is essential not to disrupt unitarity, thereby ensuring that Eq. (2.1) remains valid. For example, when a neutrino scatters off other particles, it can still remain coherent as long as the momentum transfer between the incident neutrino and the target particle is sufficiently small. This means that interactions that do not significantly change the momentum of the neutrino are less

likely to disrupt its quantum coherence. In fact, this is particularly the case for the MSW effect from coherent forward elastic scattering of the neutrinos through weak interaction, and the spin flavour precession effect caused by ν MM. The former will be included but not emphasised in this thesis, while the latter will be elaborated in the following.

2.1.1 Flavour Transition

Taking into account that neutrinos are produced and detected only through weak interactions, their initial (production) and final (detection) states are restricted to the flavor basis. However, during free propagation, the kinematic eigenstates are determined by the neutrino's mass, as a result, Eq. (2.1) will be diagonal in the mass basis. For neutrinos with an initial state as flavor α , i.e., $\rho(0) = |\nu_\alpha\rangle\langle\nu_\alpha|$, the probability of observing the final state as flavor β can be expressed as:

$$P_{\alpha\beta} = \text{Tr} [|\nu_\beta\rangle\langle\nu_\beta|\rho(t)] = \sum_{j,k} U_{\alpha j}^* U_{\beta j} U_{\alpha k} U_{\beta k}^* e^{i \frac{\Delta m_{jk}^2 t}{2p}}. \quad (2.2)$$

This expression is obtained by inserting $\mathcal{H}_{\alpha\beta} = \frac{1}{2\bar{p}} \sum_j U_{\alpha j} m_j^2 U_{j\beta}^\dagger$ into $\rho(t) = e^{-iHt} \rho(0) e^{iHt}$ to satisfy the Liouville-von Neumann equation. Here, U represents the leptonic mixing matrix, which relates the flavor and mass eigenstates as: $|\nu_\alpha\rangle = \sum_i U_{\alpha i} |\nu_i\rangle$. Note that this expression is still different from the standard vacuum oscillation formula where t and p are replaced by the propagation distance (L) and the neutrino energy (E), respectively. The difference arises because the trace is taken only to sum over the mass eigenstates, without integration over momentum (or coordinate) space and time t . A comprehensive integration will be presented later in the context of neutrino decoherence. Nevertheless, it's evident that if all eigenstates are sharply peaked at $t = L$ and $|\bar{p}| = E$ due to a delta function, the standard oscillation formula would appear, and quantum coherence remains intact. Furthermore, when neutrinos propagate through matter, coherent scattering processes will dominate over incoherent ones, leading to an effective potential in the Hamiltonian that is diagonal in the flavour basis. In this case, the flavour transition probability may be obtained by tracing over the new eigenstates of the Hamiltonian which includes the matter potential. Consequently, it results in the same form as Eq. (2.2) but with different eigenvalues (Δm_{jk}^2) and eigenvectors (U).

2.1.2 Helicity Flip by Neutrino Magnetic Moment

In general, the mass term of neutrinos can be written as $\mathcal{L}_m = m\nu_L \bar{\nu}_R$. If Dirac spinors (with four degrees of freedom) are necessary to represent the neutrino field, i.e., we have Dirac neutrinos, $\bar{\nu}_R$ represent chirally right-handed neutrino field, which is invisible to weak interaction, and lepton number is conserved. On the other hand, if it is sufficient for a neutrino field to be represent by Weyl spinor having only two degrees of freedom, then the neutrinos have a Majorana nature, and $\bar{\nu}_R = \bar{\nu}_L^c$ is the chirally left-handed neutrino field with a charge conjugation. In this case, lepton neutrino is violated by two units, making it possible for neutrinos to be produced and detected with different helicity (hence, having a helicity flip). However, such effect is m/E suppressed,

therefore, due to the smallness of neutrino mass and the difficulty of observing non-relativistic neutrinos such effect is usually negligible. Similar to the neutrino mass, in the presence of strong magnetic field, a chiral flip can also be induced since the Lagrangian for the ν MM:

$$\mathcal{L} \supset \frac{1}{2} \mu_{\alpha\beta} \nu_{L,\alpha} \sigma_{\mu\nu} \bar{\nu}_{R,\beta} F^{\mu\nu} + h.c. , \quad (2.3)$$

has the same chiral structure as the neutrino mass. Here $\mu_{\alpha\beta}$ is the magnetic moment of neutrinos, $\nu_{L,\alpha}/\nu_{R,\beta}$ is the left/right-handed neutrino field with flavor α/β , and $F^{\mu\nu}$ is the electromagnetic field strength tensor.

However, unlike neutrino mass, ν MM effect scale with the magnetic field strength. Moreover, since the momentum transfer between the incident neutrino and the magnetic field is negligible, coherence will be contained with an additional potential term in the Hamiltonian which mixes the right and left chiral states. In other words, $|\nu(t, \vec{p})\rangle$ include n flavor states $\otimes m$ spinor states and satisfy the Liouville-von Neumann equation. Furthermore, since neutrinos are usually ultra-relativistic, helicity would majorly coincide with chirality. Therefore, written in the standard three flavor basis, $\{\alpha, \beta\} = \{e, \mu, \tau\}$, and the two helicity basis, $\{h, h'\} = \{1 \text{ (for } \nu_L), 2 \text{ (for } \bar{\nu}_L)\}$, the 6×6 entries of the Hamiltonian is

$$\mathcal{H}_{\alpha\beta}^{11/22} = \frac{1}{2\bar{p}} \sum_j U_{\alpha j} m_j^2 U_{j\beta}^\dagger \pm \delta_{\alpha\beta} V_\alpha^{\text{mat}}, \quad (2.4)$$

$$\mathcal{H}_{\alpha\beta}^{12} = (\mathcal{H}_{\beta\alpha}^{21})^* = \mu_{\alpha\beta} B_\perp e^{i\phi}, \quad (2.5)$$

for Majorana neutrinos. Here, the first term in Eq. (2.4) would be responsible for neutrino oscillation in vacuum due to the mass splitting, where m_j is the neutrino mass and $U_{\alpha\beta}$ is the leptonic mixing matrix; the second term is the MSW matter potential, which is diagonal in flavor space; and Eq. (2.5) describes the helicity flip induced by $B_\perp e^{i\phi}$, the strength of the magnetic field perpendicular to the propagation direction of the neutrino. We note that $\mu_{\alpha\beta}$ is asymmetric due to CPT symmetry (i.e., $U_{\alpha\alpha} = 0$), indicating that a neutrino with one flavor α will be converted to another flavor $\beta \neq \alpha$ by ν MM effects. As for Dirac neutrinos, the helicity basis is doubled, viz. $\{h, h'\} = \{1 \text{ (for } \nu_L), 2 \text{ (for } \bar{\nu}_L), 3 \text{ (for } \nu_R), 4 \text{ (for } \bar{\nu}_R)\}$, the Hamiltonian defining the evolution is thus extended to a 12×12 matrix, expressed as

$$\mathcal{H}_{\alpha\beta}^{11/22} = \frac{1}{2\bar{p}} \sum_j U_{\alpha j} m_j^2 U_{j\beta}^\dagger \pm \delta_{\alpha\beta} V_\alpha^{\text{mat}}, \quad (2.6)$$

$$\mathcal{H}_{\alpha\beta}^{33} = \mathcal{H}_{\alpha\beta}^{44} = \frac{1}{2\bar{p}} \sum_j U_{\alpha j} m_j U_{j\beta}^\dagger, \quad (2.7)$$

$$\mathcal{H}_{\alpha\beta}^{14} = \mathcal{H}_{\alpha\beta}^{41} = (\mathcal{H}_{\beta\alpha}^{23})^* = (\mathcal{H}_{\beta\alpha}^{32})^* = \mu_{\alpha\beta} B_\perp e^{i\phi}, \quad (2.8)$$

while the rest of the entries are 0. The ν MM effects for Dirac neutrino are expected to be dominated by flavour diagonal terms of $\mu_{\alpha\beta}$ even though all entries are allowed, since the off-diagonal terms would, in principle, suffer from the GIM mechanism.

2.1.3 Length-scales

Different effects may be decoupled if their length-scales differ by orders of magnitude. The length-scale of a certain effect X (e.g., mass-splitting, MSW effect, and ν MM effect) is determined by the associated Hamiltonian, dubbed as H_X , and is given by

$$L_{jk} = 2\pi/(H_j - H_k), \quad (2.9)$$

for H_k the k th eigenvalue of H_X . Reading from the first term in Eqs. (2.4) and (2.6), the length-scale of mass-splitting is set by the oscillation length for the larger $m_j^2 - m_k^2$, i.e.,

$$L_{\text{mass}} = \frac{4\pi E}{\Delta m_{jk}^2} \simeq 2.0 \times 10^9 \text{ km} \left(\frac{2.44 \times 10^{-3} \text{ eV}^2}{\Delta m_{32}^2} \right) \left(\frac{\text{E}}{100 \text{ TeV}} \right), \quad (2.10)$$

where j, k denote the mass eigenstates. For the MSW effect, we have the refractive length,

$$L_{\alpha\beta}^{\text{mat}} = \frac{2\pi}{V_\alpha - V_\beta}, \quad (2.11)$$

for the flavor eigenstates α, β . Therefore, since contributions from neutral current will cancel among flavours, the length-scale would be left with,

$$L_{\text{mat}} = \frac{\sqrt{2}\pi}{G_F n_e}, \quad (2.12)$$

where G_F is the Fermi constant, and $n_e = n_{\text{bary}} Y_e$ is the electron's number density for the baryon number density n_{bary} and the electron fraction Y_e . In contrast to the above two length-scales, that for ν MM effect is sensitive to the nature of neutrinos. In particular, we have

$$L_{\alpha\beta}^{\text{mag,D}} = 4\pi(\mu_\alpha - \mu_\beta)^{-1} B_\perp^{-1} \quad (2.13)$$

for Dirac neutrinos, where α, β is expected be close to the flavor eigenstates considering that flavour diagonal terms are significantly larger than off-diagonal ones. On the other hand, the length-scale is less straightforward to define for Majorana neutrinos due to the asymmetry of the ν MM matrix. As we will derive later in this section, the length-scale can be found as

$$L_{\text{mag}}^{\text{M}} = 4\pi\mu_\nu^{-1} B_\perp^{-1} \quad (2.14)$$

with $\mu_\nu^2 = \mu_{e\mu}^2 + \mu_{e\tau}^2 + \mu_{\mu\tau}^2$ and the Bohr magneton μ_B .

Comparing two effects, the one with a small length scale would dominate. This can be understood by the smaller length scale having a larger frequency, therefore, the reaction time-scale would be shorter and the energy would be larger. Furthermore, the mass splitting effect is dependent on neutrino energy while the matter potential as well as the magnetic field potential would be localized in space. Hence, only in certain energy and/or coordinate regions will two effects be comparable with each other, or even have a resonant effect, while in the other

regions, one effect will dominate over the others. For instance, L_{mass} would increase with the neutrino energy, so if it is larger than the region where νMM potential is relevant (neglecting matter effect), then the transition probability can be decoupled as

$$P_{\alpha\beta}^{hh'}(0 \rightarrow L) \simeq \sum_{\delta} P_{\alpha\delta}^{hh'}(0 \rightarrow L_{\text{cut}}; \mathcal{H} = \mathcal{H}_{\nu\text{MM}}) \times P_{\delta\beta}^{h'h'}(L_{\text{cut}} \rightarrow L; \mathcal{H} = \mathcal{H}_{\text{mass}}). \quad (2.15)$$

Such decoupling occurs when there exist L_1, L_2 , where $L_1 < L_{\text{cut}} < L_2$, such that $L_{\text{mass}} \gg L_{\nu\text{MM}}$ when $\ell < L_1$ and $L_{\text{mass}} \ll L_{\nu\text{MM}}$ when $\ell > L_2$. Here, ℓ is the traveling distance of the neutrinos. In fact, this would be particularly the case for magnetar produced neutrinos with energy above 100 TeV, which will be investigated in Chapter 5.

2.1.4 Anti-symmetric Hamiltonian

For Majorana neutrinos, in the region where νMM effect dominates (i.e., when $\ell < L_{\text{cut}}$), the time evolution cannot be solved by diagonalizing the Hamiltonian due to its asymmetry. However, we can block diagonalize the time evolution operator $\exp[-iA(t)]$ satisfying Eq. (2.1) as

$$\rho(t, \vec{p}) = |\nu(t, \vec{p})\rangle\langle\nu(t, \vec{p})| = e^{-iA(t)}\rho(0, \vec{p})e^{iA(t)}, \quad (2.16)$$

by recasting it into the form:

$$\exp\left[-i\int_0^t dt' \begin{pmatrix} 0 & \tilde{\mu}B_{\perp}(t')e^{i\phi} \\ \tilde{\mu}^{\dagger}B_{\perp}(t')e^{-i\phi} & 0 \end{pmatrix}\right] = \begin{pmatrix} \tilde{U}\cos\hat{\theta}(t)\tilde{U}^{\dagger} & iU\sin\hat{\theta}(t)\tilde{U}^{\dagger}\hat{\mu}_{\nu} \\ -i\hat{\mu}_{\nu}^{\dagger}\tilde{U}\sin\hat{\theta}(t)\tilde{U}^{\dagger} & \tilde{U}\cos\hat{\theta}(t)\tilde{U}^{\dagger} \end{pmatrix}$$

for

$$\hat{\mu} = \frac{1}{\mu_{\nu}} \begin{pmatrix} 0 & \mu_{e\mu} & \mu_{e\tau} \\ -\mu_{e\mu} & 0 & \mu_{\mu\tau} \\ -\mu_{e\tau} & -\mu_{\mu\tau} & 0 \end{pmatrix} \quad (2.17)$$

with $\mu_{\nu} = \sqrt{\mu_{e\mu}^2 + \mu_{e\tau}^2 + \mu_{\mu\tau}^2}$ (i.e., $\tilde{\mu} = \mu_{\nu}\hat{\mu}$). Moreover, when the geometric of magnetic field evolves slowly such that $|\phi/\nabla\phi| \ll 1$ (as in the case of dipolar structure considered in Chapter 5), the νMM effect is adiabatic and the $e^{\pm i\phi}$ can be factored out, leaving no physical influence. Consequently, we have $U^{\dagger}|\hat{\mu}|^2U = \text{diag}(0, 1, 1)$ and thus $\hat{\theta}(t) = \theta_{\nu}(t)\text{diag}(0, 1, 1)$ for the oscillation phase given by

$$\theta_{\nu}(t) = \mu_{\nu} \int_0^t dt' B_{\perp}(t'). \quad (2.18)$$

We see that the magnitude of the νMM effect is decided by the effective eigenvalue μ_{ν} through the oscillation phase θ_{ν} , and the flavor structure of it is determined by \tilde{U} and $\hat{\mu}_{\nu}$.

In addition, the transition probability from ν_{α}^h to $\nu_{\beta}^{h'}$ can be calculated through $P_{\alpha\beta}^{hh'} =$

$\text{Tr} \left[\langle \nu_{\beta}^{h'} | \rho^{(\alpha, h)}(t) | \nu_{\beta}^{h'} \rangle \right]$, which reads

$$P_{\alpha\beta}^{\text{HC}} = \text{Tr} \left[|\langle \nu_{\beta} | \text{U} \cos(\hat{\theta}) \text{U}^{\dagger} | \nu_{\alpha} \rangle|^2 \right] = \sum_{j,k} \text{U}_{\alpha j}^* \text{U}_{\beta j} \text{U}_{\alpha k} \text{U}_{\beta k}^* \cos \theta_j \cos \theta_k, \quad (2.19)$$

when helicity is conserved ($h = h'$), and

$$P_{\alpha\beta}^{\text{HF}} = \text{Tr} \left[|\langle \nu_{\beta} | \tilde{\text{U}} \cos(\hat{\theta}) \tilde{\text{U}}^{\dagger} \hat{\mu}_{\nu} | \nu_{\alpha} \rangle|^2 \right] = \sum_{j,k,\gamma,\delta} \hat{\mu}_{\alpha\gamma}^* \hat{\mu}_{\alpha\delta} \tilde{\text{U}}_{\gamma j}^* \tilde{\text{U}}_{\beta j} \tilde{\text{U}}_{\delta k} \tilde{\text{U}}_{\beta k}^* \sin \theta_j \sin \theta_k, \quad (2.20)$$

when helicity is flipped ($h \neq h'$). Here, the (effective) eigenvalues are $\theta_1 = 0$ and $\theta_2 = \theta_3 = \theta_{\nu}(t)$. The CP symmetry is assumed in the above expressions; in general, $P_{\alpha\beta}^{\text{HC}}$ ($P_{\alpha\beta}^{\text{HF}}$) would be splitted into $P_{\alpha\beta}^{++}$ and $P_{\alpha\beta}^{--}$ ($P_{\alpha\beta}^{+-}$ and $P_{\alpha\beta}^{-+}$) by an additional CP phase.

As mentioned above, the two phenomenological inputs for decoupled Majorana ν MM effect would be the effective magnetic moment μ_{ν} , and the flavour structure $\hat{\mu}$. The transition probability would be maximized when $\theta_{\nu}(\propto \mu_{\nu}) = \pi/2$ and how the flavour structure of the ν MM matrix reflect on the flavour structure of the transition probability $P_{\alpha\beta} = P_{\alpha\beta}^{\text{HC}} + P_{\alpha\beta}^{\text{HF}}$ is shown in Fig. 2.1, where full coherence is assumed. In particular, plot (a) and (c), as well as plot (b) and (d), compensate each other by $\sum_{\beta} P_{\alpha\beta} = 1$. For instance, when only $\mu_{\beta\gamma} \neq 0$ (top corner), the ν_{α} state would not be affected, hence, $P_{\alpha\alpha} = 1$ while $P_{\alpha\beta} = P_{\alpha\gamma} = 0$ for $\alpha \neq \beta \neq \gamma$. Note that $P_{\alpha\gamma}$ would simply be plot (c)/(d) after exchanging β and γ . The lower left corner is when only $\mu_{\alpha\beta} \neq 0$, in this case, there will be an 100% transition from ν_{α} to ν_{β} in the optimal $\theta_{\nu} = \pi/2$ scenario. However, in the equilibrium scenario, where θ_{ν} is averaged over, ν_{α} and ν_{β} will each have a 50% share. In fact, such equilibrium feature holds in general, for instance, the center point of plot (b) and (d) indicates that all flavours each have a 1/3 share when $\mu_{e\mu} = \mu_{e\tau} = \mu_{\mu\tau}$. Such flavour structure will be crucial once the initial flavour is taken into account, this will be explored for the typical initial states for high energy neutrinos in Chapter 5.

2.2 Open Quantum System

In an open quantum system, the system is coupled to the environment, leading to a gradual leakage of information into the environment. Consequently, the unitary for the evolution of the density matrix of this system, $\rho_S = \text{Tr}_{\text{E}}[\rho]$, would no longer hold when the Liouville-von Neumann equation is only satisfied for the complete density matrix ρ . Here Tr_{E} signifies the process of tracing out or removing the environmental degrees of freedom, leaving only the focus on the system's dynamics. Such leak of information would cause the lost of coherence, namely, the lost of interference between two eigenstates. Such process of losing quantum interference is decoherence, which describes how a (entangled) quantum state evolves into a classical state.

For the flavour transition probability (FTP) describing neutrino oscillation, decoherence

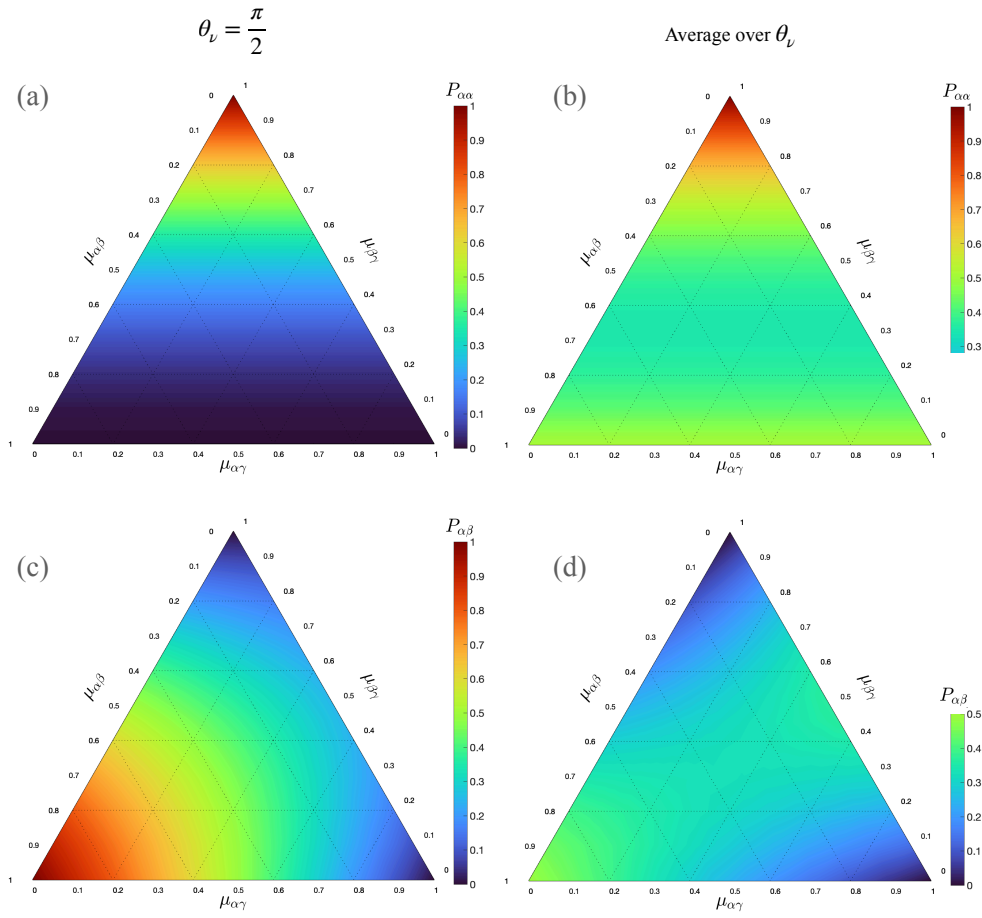


Figure 2.1: Demonstration of how the flavour structure matrix $\hat{\nu}$ would reflect on the flavour structure of the transition probability. (a) and (b) is the probability that the flavour remains unchanged, while (c) and (d) is the transition of state ν_α to ν_β where $\alpha \neq \beta$. (a) and (c) is when HF is maximized (i.e. at $\theta_\nu = \pi/2$) while (b) and (d) when equilibrium is reached between transitions (i.e. when θ_ν is averaged over).

effect can be summarized by a function Ψ_{jk} as

$$P_{\alpha\beta} = \sum_{j,k} U_{\alpha j}^* U_{\beta j} U_{\alpha k} U_{\beta k}^* e^{i\psi_{jk}} \Psi_{jk}, \quad (2.21)$$

where ψ_{jk} is the coherent phase, commonly approximated $\Delta m_{jk}^2 L_0 / (2E_0)$ for some traveling distance L_0 and energy E_0 . The decoherence term Ψ_{jk} would, in general, erase the interference pattern, hence, $|\Psi_{jk}| \leq 1$. However, since it could also be complex, it might also cause a phase shift w.r.t. ψ_{jk} . Furthermore, $\Psi_{jj} = 1, \forall j$, since the correlation, or overlap-ness, between an eigenstate and itself is naturally 100%. These properties will be shown to hold without assumption using the QFT approach in Sec. 4.1. Therefore, when neutrino state is fully decohered, the FTP reads

$$P_{\alpha\beta} = |U_{\alpha 1} U_{\beta 1}^*|^2 + |U_{\alpha 2} U_{\beta 2}^*|^2 + |U_{\alpha 3} U_{\beta 3}^*|^2, \quad (2.22)$$

which is widely used for neutrinos traveling over a cosmic distance. Similarly, the transition probability in Eq. (2.19) and Eq. (2.20) for an anti-symmetric Hamiltonian would be modified as

$$P_{\alpha\beta}^{\text{HC}} = \sum_{j,k} \tilde{U}_{\alpha j}^* \tilde{U}_{\beta j} \tilde{U}_{\alpha k} \tilde{U}_{\beta k}^* \Psi_{j,k} \cos \theta_j \cos \theta_k, \quad (2.23)$$

$$P_{\alpha\beta}^{\text{HF}} = \sum_{j,k,\gamma,\delta} \hat{\mu}_{\alpha\gamma}^* \hat{\mu}_{\alpha\delta} \tilde{U}_{\gamma j}^* \tilde{U}_{\beta j} \tilde{U}_{\delta k} \tilde{U}_{\beta k}^* \Psi_{j,k} \sin \theta_j \sin \theta_k, \quad (2.24)$$

where $\theta_1 = 0, \theta_2 = \theta_3 = \theta_\nu(t)$. Note that, unlike neutrino oscillation in vacuum, where $\psi_{jj} = 0, \forall j$, the transition probability will still have a time dependence from the modes where $j = k$, since the time evolution operator can only be block diagonalized. In this case

$$P_{\alpha\beta}^{\text{HC}} = |\tilde{U}_{\alpha 1} \tilde{U}_{\beta 1}^*|^2 + \left(|\tilde{U}_{\alpha 2} \tilde{U}_{\beta 2}^*|^2 + |\tilde{U}_{\alpha 3} \tilde{U}_{\beta 3}^*|^2 \right) \cos^2 \theta_\nu(t), \quad (2.25)$$

and

$$P_{\alpha\beta}^{\text{HF}} = \sum_{j,\gamma,\delta} \hat{\mu}_{\alpha\gamma}^* \hat{\mu}_{\alpha\delta} \tilde{U}_{\gamma j}^* \tilde{U}_{\beta j} \tilde{U}_{\delta j} \tilde{U}_{\beta j}^* \sin^2 \theta_\nu(t). \quad (2.26)$$

2.2.1 Formalisms for Neutrino Decoherence

The literature extensively explores various theoretical approaches to quantify quantum decoherence in neutrino oscillation, often referred to as neutrino decoherence. In the framework of the open quantum system, decoherence can be analyzed through the framework of Liouville dynamics using density matrices [15–23]. The Lindblad equation

$$\dot{\rho} = -i[H, \rho] + \sum_k \left(L_k \rho L_k^\dagger - \frac{1}{2} \{L_k^\dagger L_k, \rho\} \right) \quad (2.27)$$

is often used in this approach. In this equation, the Lindblad operators L_k serve as parameters that quantify the extent of decoherence. This approach is valid when the Markov approximation

holds, which implies that the environment's response occurs significantly faster than that of the system of interest. In other words, the environment has not quantum memory effect, such that the system's time evolution can be effectively described through time-local quantum master equations.

In addition, decoherence can also be expressed by the Wigner quasi-probability distribution [19, 24, 25] through the Wigner-Weyl transformation:

$$\mathcal{W}(\hat{\rho}) = \int \int dx dy \langle x + \frac{1}{2} | \hat{\rho} | x - \frac{1}{2} \rangle e^{-iy \cdot p}. \quad (2.28)$$

On the other hand, neutrino decoherence is often described by the degree of wavepacket separation using principles from quantum mechanics (QM) [26–30] and quantum field theory (QFT) [28, 31–35]. Furthermore, there is a body of literature that compares these different approaches, including comparisons between QM and QFT methods for wavepacket separation [28], as well as comparisons involving the Lindblad equation in relation to both the wavepacket format [17] and the Wigner quasi-probability distribution [19]. Among these diverse theories, QFT stands out as a comprehensive description, describing neutrino oscillation as the propagator within a full Feynman diagrams including both production and detection process. On the other hand, the open quantum system method is more tailored to address quantum decoherence effects, offering a broader perspective by considering a system of interest within its surrounding environment.

2.2.2 The Quantum Field Theory Formalism

In this thesis, we introduce a novel approach known as the open quantum system method into quantum field theory (QFT) calculations. In this approach, we regard the propagator describing neutrino oscillation as the system of interest, treating everything else in the diagram as the surrounding environment, which we intend to integrate out of the calculations. Furthermore, since neutrino oscillation is a phenomenon arising from the coherence of kinematics between mass eigenstates, the states of the environment that we integrate out exist within the phase space (PS). To be more specific, if a state is characterized by creation and annihilation operators in either the coordinate or momentum space, we refer to it as the "Fock-PS". On the other hand, if a state is defined by occupation numbers within a PS, resulting in a Wigner quasi-probability distribution, we call it the "Wigner-PS." It's worth noting that, since the Fock space representations for mass basis and flavor basis are unitarily inequivalent with each other [36, 37], at least one of them must be unphysical. Given that both representations approximately coincide with each other in the relativistic limit, our choice is to construct the Fock-PS for mass states, with flavor states being represented as a superposition of mass states. However, it's essential to recognize that one can also establish a flavor-based Fock-PS for the layered structure, as this choice does not dictate the specific representation we opt for in our analysis.

Specifically, we compute the transition amplitude using the Fock-PS representation by applying the S -matrix method as outlined in [31]. In this context, we treat the traveling neutrino

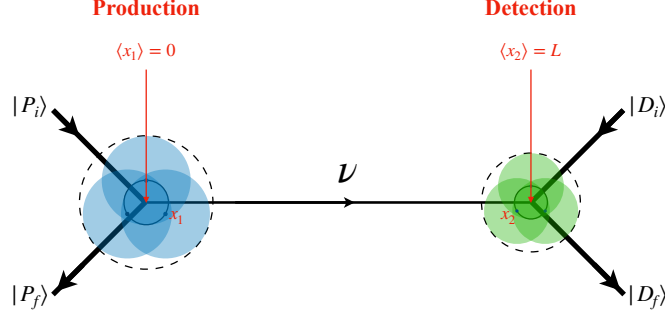


Figure 2.2: A simplified Feynman diagram where the neutrino propagating a macroscopic distance is treated as a propagator of a full diagram, and the kinematics of the external particles are described with wavepackets. At the production/detection vertex site, the diameter of the shaded blue/green areas represent the uncertainties of external wavepackets projected onto the coordinate space, and their mean value is labeled as x_1/x_2 . The inner circles with solid lines at both sites are the additional coordinate uncertainties from the blob vertices for the internal states regardless of the external particles. In other words, it represents the uncertainties of x_1/x_2 by $g_P(x_1)/g_D(x_2)$ in Eq. (2.30). Hence the total uncertainty on the coordinate space at this layer would be the diameter of the dashed-lined circles.

as an internal propagator within a diagram of the full process, including both production and detection interactions, as illustrated in Figure 2.2. The kinematic properties of the neutrino's initial and final states are expressed as WPs in momentum space, which will later be combined into a weighting function with a width denoted as σ_p . Consequently, without loss of generality we can write

$$\begin{aligned} |P_i\rangle &= \int [dq] f_{P_i}(q, t) |q\rangle, & |P_f\rangle &= \int [dk] f_{P_f}(k, t) |k\rangle, \\ |D_i\rangle &= \int [dq'] f_{D_i}(q', t) |q'\rangle, & |D_f\rangle &= \int [dk'] f_{D_f}(k', t) |k'\rangle, \end{aligned} \quad (2.29)$$

Here, $[dh] = d^3h/(2\pi)^3$ for each $h = \{q, k, q', k'\}$. Additionally, the internal states (excluding the neutrino propagator) of the process are described by the distributions $g_P(x_1)$ and $g_D(x_2)$. These distributions account for space-time uncertainties around the vertex at the production and detection sites, respectively. It is important to note that since these states are not constrained to the mass-shell, such uncertainties encompass four degrees of freedom: a temporal uncertainty and three spatial ones. In contrast, the on-shell WPs only possess three degrees of freedom. However, these uncertainties are typically not explicitly emphasized in the literature. Concerning WP separation, we will demonstrate that they can effectively be combined with σ_p . Regarding a localization term, as seen in [32], these uncertainties are microscopic compared to the scale of the experiment. Nevertheless, given that the external particles are better characterized and are, in principle, observable, there remains the possibility of extracting the contribution of such uncertainties through measurements.

We can readily compute the transition amplitude for a neutrino that is initially produced

as flavor α , detected as flavor β , and propagating in mass eigenstates with mass m_j . To make our structure complete, we integrate over both x_1 and x_2 . In this regard, the total amplitude is expressed as:

$$\begin{aligned}
iA_{2,\alpha\beta}(T, \mathbf{L}, \mathbf{P}) &\equiv i \sum_j U_{\alpha j}^* U_{\beta j} A_{2,j}(T, \mathbf{L}, \mathbf{P}) \\
&= i \sum_j U_{\alpha j}^* U_{\beta j} \int [dq] f_{P_i}(\mathbf{q}) \int [dk] f_{P_f}^*(\mathbf{k}) \int [dq'] f_{D_i}(\mathbf{q}') \int [dk'] f_{D_f}^*(\mathbf{k}') \\
&\times \int d^4 x_1 g_P(x_1) \int d^4 x_2 g_D(x_2) \int d^4 y_2 M_{Dj}(q', k') e^{-i(q'-k')(y_2-x_2)} \\
&\times \int \frac{d^4 p_\nu}{(2\pi)^4} \frac{\not{p}_\nu + m_j}{p_\nu^2 - m_j^2 + i\epsilon} e^{-ip_\nu(y_1-y_2)} \int d^4 y_1 M_{Pj}(q, k) e^{-i(q-k)(y_1-x_1)}. \quad (2.30)
\end{aligned}$$

In this expression, $M_P(q, k)$ and $M_D(q', k')$ represent the plane-wave amplitudes associated with the particles involved in the production and detection processes, respectively. In the following sections, we will explicitly compute the transition amplitude by singling out the neutrino system (equivalently, tracing out the environment) from two distinct perspectives in terms of how the “neutrino system” is defined.

Neutrinos Represented Indirectly

In the viewpoint that neutrinos are represented by states entangled to it, the Fock-PS is composed by $x = x_2 - x_1$ and $\bar{p} = \mathbf{q} - \mathbf{k} = \mathbf{k}' - \mathbf{q}'$. Here x_1/x_2 are the space-time coordinates of the production/detection vertices and $\mathbf{q}, \mathbf{k}, \mathbf{q}', \mathbf{k}'$ are the momenta of the initial and final states of the production and detection sites. Therefore, x and \bar{p} represent the traveling distance and the momentum of the neutrino determined by the external particles and the position of the vertices — essentially, the states entangled with the neutrino. The process to reach the expression where the neutrino system is singled out (i.e. Eq. (3.7) in the next chapter) includes a series of Fourier transformations and convolutions. We summarize these processes in Fig. 2.3. These relations are particularly important in the sense that we can clearly see how each of the uncertainties are combined to an effective one. Note that Fourier properties in Appendix ??, which is summarized in Table A.1 and Table A.2, are particularly useful. Below, we will outline the step-by-step derivation process from Eq. (2.30) to Eq. (3.7), which leads to the relations in Fig. 2.3. We first include all the uncertainties following Eq. (2.30):

$$\begin{aligned}
A_{2,j}(T, \mathbf{L}, \mathbf{P}) &= \int [dq] f_{P_i}(\mathbf{q}) \int [dk] f_{P_f}^*(\mathbf{k}) \int [dq'] f_{D_i}(\mathbf{q}') \int [dk'] f_{D_f}^*(\mathbf{k}') \\
&\times \int d^4 x_1 g_P(x_1) \int d^4 x_2 g_D(x_2) \int d^4 y_2 M_{Dj}(q', k') e^{-i(q'-k')(y_2-x_2)} \\
&\times \int \frac{d^4 p_\nu}{(2\pi)^4} \frac{\not{p}_\nu + m_j}{p_\nu^2 - m_j^2 + i\epsilon} e^{-ip_\nu(y_1-y_2)} \int d^4 y_1 M_{Pj}(q, k) e^{-i(q-k)(y_1-x_1)}. \quad (2.31)
\end{aligned}$$

In addition, since the external states are on the mass-shell, $h^0 = E_h(\mathbf{h}) = \sqrt{\mathbf{h}^2 - m_h^2} \forall h = \{q, k, q', k'\}$. Furthermore, if the WPs are sharply peaked at the expectation value $\langle h \rangle$, we can write $E_h(\mathbf{h}) \simeq E_h + \mathbf{v}_h(\mathbf{h} - \mathbf{h}_0)$, where $E_h = E_h(\langle h \rangle)$, using the saddle point approximation. As for the production site, the integration over k performs a convolution between the initial state and the final state while the plane wave, amplitudes $M_{P_j}(q, k)$, are included. Namely,

$$\begin{aligned} & \int \frac{d^3k}{(2\pi)^3} f_{P_f}^*(\mathbf{k}) f_{P_i}(\mathbf{k} - \mathbf{p}) M'_{P_j}(\mathbf{p}, \mathbf{k}) e^{-i(y_1^0 - x_1^0)(E_q(\mathbf{k} - \bar{\mathbf{p}}) - E_k(\mathbf{k}))} \\ & = F_{P_j}(\bar{p}) F'_P(y_1^0 - x_1^0) e^{i\xi(\bar{p})(y_1^0 - x_1^0)}, \end{aligned} \quad (2.32)$$

Here, a change of variables: $\{q, k\} \rightarrow \{p, k\}$, where $p = k - q$, is applied. Also, we have written $M'_{P_j}(\bar{p}, \mathbf{k}) = M_{P_j}(k - p, k)|_{p^0 = E_q(\mathbf{k} - \bar{\mathbf{p}}) - E_k(\mathbf{k}), k^0 = E_k(\mathbf{k})}$ for convenience. In particular, if f_{P_i} and f_{P_j} are Gaussian distributed with width σ_q and σ_k respectively, the momentum uncertainties from the external states at the production site would be

$$F_{P_j} = M'_{P_j}(\langle \mathbf{p} \rangle, \langle \mathbf{k} \rangle) \exp \left[\frac{-(\bar{p} - \mathbf{P})^2}{4(\sigma_q^2 + \sigma_k^2)} \right], \quad (2.33)$$

where $\mathbf{P} = \langle \mathbf{q} \rangle - \langle \mathbf{k} \rangle$. The other terms are

$$F'_P(y_1^0 - x_1^0) = \exp \left[-(y_1^0 - x_1^0)^2 \sigma_{qk}^2 \mathbf{v}_{qk}^2 \right], \quad (2.34)$$

$$\xi_P(\bar{p}) = E_q - E_k - \mathbf{v}_q \mathbf{q}_0 + \mathbf{v}_k \mathbf{k}_0 + \frac{\mathbf{v}_{qk}^2}{\Delta_{qk}} \mathbf{P} + \bar{p} \left(\mathbf{v}_q + \frac{\mathbf{v}_{qk}^2}{\Delta_{qk}} \right). \quad (2.35)$$

Particularly, $\mathbf{v}_{qk} = \mathbf{v}_q - \mathbf{v}_k$, $\Delta_{qk} = (\sigma_q^2 + \sigma_k^2)/\sigma_k^2$, and σ_{kq} refers to the notation in Table A.1. The detection site can be derived analogously, by having $\bar{p}' = \mathbf{k}' - \mathbf{q}'$ and $\mathbf{P}' = \langle \mathbf{k}' \rangle - \langle \mathbf{q}' \rangle$ instead. Therefore, Eq. (2.31) can be reformulated as:

$$\begin{aligned} A_{2,j} & = \int d^3p F_{P_j}(\bar{p}) \int d^3p' F_{D_j}(\bar{p}') \int d^4x_1 g_P(x_1) \int d^4x_2 g_D(x_2) \\ & \times \int d^4y_1 e^{-i(y_1^0 - x_1^0)\xi_P(\bar{p}) + i(\mathbf{y}_1 - \bar{\mathbf{x}}_1)\bar{p}} F'_P(y_1^0 - x_1^0) \int d^4y_2 e^{-i(y_2^0 - x_2^0)\xi_D(\bar{p}') + i(\mathbf{y}_2 - \bar{\mathbf{x}}_2)\bar{p}'} F'_D(y_2^0 - x_2^0) \\ & \times \int \frac{d^4p_\nu}{(2\pi)^4} \frac{\not{p}_\nu + m_j}{p_\nu^2 - m_j^2 + i\epsilon} e^{-ip_\nu(y_1 - y_2)}. \end{aligned} \quad (2.36)$$

The integration over $\int d^3y_1$ and $\int d^3y_2$ gives rise to $\delta^3(\bar{p} - \bar{p}_\nu)$ and $\delta^3(\bar{p}' - \bar{p}_\nu)$, respectively. On the other hand, the integration over $\int dy_1^0$ returns

$$\int dy_1^0 e^{-iy_1^0(\xi(\bar{p}) - p_\nu^0)} F'_P(y_1^0 - x_1^0) = e^{-ix_1^0(\xi(\bar{p}) - p_\nu^0)} \tilde{F}'_P(\xi(\bar{p}) - p_\nu^0), \quad (2.37)$$

where \tilde{F}'_P is the Fourier transformation of F'_P . Finally after including the detection site, Eq. (2.36) takes the form:

$$A_{2,j} = \int d^3p \int d^4x F_j(\bar{p}; \mathbf{P}) G(x; X) A_{1,j}(x, \bar{p}), \quad (2.38)$$

where $x = x_2 - x_1$, $F_j(\bar{p}, \mathbf{P}) = F_{P_j}(\bar{p}) F_{D_j}(\bar{p})$,

$$G(x) = \int d^4x_2 g_P(x_2 - x) g_D(x_2). \quad (2.39)$$

As we will see in the next chapter, this expression takes the form of a layer moving operator. Furthermore, the transition amplitude of the neutrino system becomes:

$$A_{1,j}(x, \bar{p}) = e^{i\bar{p}x} \int dp_\nu^0 e^{-ip_\nu^0 x^0} \tilde{F}'_P(\xi_P(\bar{p}) - p_\nu^0) \tilde{F}'_D(\xi_D(\bar{p}) - p_\nu^0) \frac{\not{p}_\nu + m_j}{p_\nu^2 - m_j^2 + i\epsilon} \Big|_{\bar{p}_\nu = \bar{p}}. \quad (2.40)$$

Intuitively, this expression may be interpreted as the collection of all configuration that are energetically allowed for some \bar{p} given by the external particles. Moreover, since the neutrino propagates a macroscopic distance, we may consider them to travel on the mass-shell. In other words, the dispersion relation $p_\nu^0 = E_j(\bar{p}) \equiv \sqrt{\bar{p}^2 + m_j^2}$ would hold. Therefore, we can replace $A_{1,j}(x, \bar{p}) \rightarrow e^{-itE_j(\bar{p}) + i\bar{x}\bar{p}}$ and

$$F_j(\bar{p}) \rightarrow F_j(\bar{p}) \tilde{F}'_P(\xi(\bar{p}) - E_j(\bar{p})) \tilde{F}'_D(\xi'(\bar{p}) - E_j(\bar{p})), \quad (2.41)$$

in Eq. (2.38). In this case, the width of F_j , σ_p becomes

$$\frac{1}{\sigma_p^2} = \frac{1}{\sigma_q^2 + \sigma_k^2} + \frac{1}{\sigma_{q'}^2 + \sigma_{k'}^2} + \frac{|\mathbf{v}_q - \mathbf{v}_j + \mathbf{v}_{qk}^2 / \Delta_{qk}|}{\sigma_{qk}^2 \mathbf{v}_{qk}^2} + \frac{|\mathbf{v}_{q'} - \mathbf{v}_j + \mathbf{v}_{q'k'}^2 / \Delta_{q'k'}|}{\sigma_{q'k'}^2 \mathbf{v}_{q'k'}^2}. \quad (2.42)$$

This result can be more efficiently observed from Fig. 2.3.

The calculation can be further carrier out by integrating out the coordinate space $\int d^4x$, for $X = (T, \mathbf{L})$:

$$A_{2,j} = \int d^3p e^{-iT E_j(\bar{p}) + i\mathbf{L}\bar{p}} F_j(\bar{p}; \mathbf{P}) \tilde{G}(\bar{p}). \quad (2.43)$$

Under the condition that one of the functions F_P , F_D , \tilde{F}'_P , \tilde{F}'_D or \tilde{G} is sharply peaked, we can apply the saddle point approximation at \mathbf{P}_j , such that

$$\frac{d}{d\bar{p}} F_j(\bar{p}; \mathbf{P}) \tilde{G}(\bar{p}) \Big|_{\bar{p}=\mathbf{P}_j} = 0. \quad (2.44)$$

This leads to $E_j(\bar{p}) \simeq E_j + \mathbf{v}_j(\bar{p} - \mathbf{P}_j)$, resulting in the final form of the transition amplitude as

$$A_{2,j} = e^{-iE_j T + i\mathbf{P}_j \mathbf{L}} \hat{\Phi}_j(\mathbf{L}_j, \mathbf{P}_j), \quad (2.45)$$

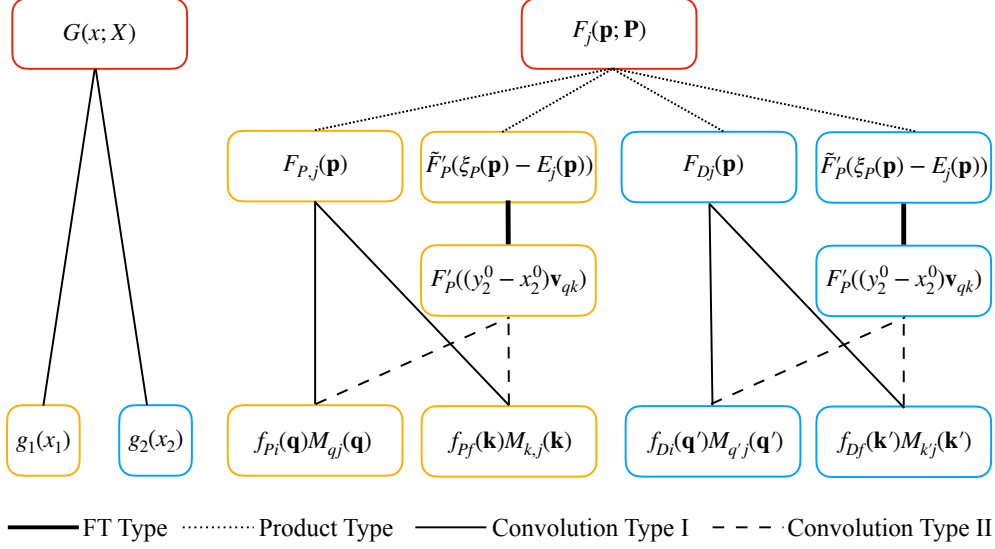


Figure 2.3: The final (width of the) weighting functions ($G(x; X)$ and $F_j(\bar{p}, \mathbf{P})$) in terms of the wavepacket (size) of each of the external particles, and the spatial uncertainty (size) at the vertices. Referring to Table A.1 and Table A.2, this diagram is useful for finding how the widths are related, and how they contribute to the width of the weighting functions, which are σ_x and σ_p in the main text.

where $\mathbf{L}_j = \mathbf{L} - \mathbf{v}_j T$. Similarly, for

$$G_x(x, X) = \exp \left[-\frac{(t-T)^2}{4\sigma_t^2} - \frac{(\bar{x} - \mathbf{L})^2}{4\sigma_{\bar{x}}^2} \right], \quad (2.46)$$

after integrating over x , which preforms a Fourier transformation to the momentum space, we will arrive at:

$$\int dt \int d^3 x e^{-it(E_j + \mathbf{v}_j \bar{p} - \mathbf{v}_j \mathbf{P}_j) + i\bar{x}\bar{p}} G_x(x, X) \quad (2.47)$$

$$= e^{-i(E_j - \mathbf{v}_j \mathbf{P}_j)T + i\bar{p}(\mathbf{L} - \mathbf{v}_j T)} \exp \left[-(\sigma_t^2 \mathbf{v}_j^2 + \sigma_{\bar{x}}^2)(\bar{p} - \tilde{m}_j)^2 \right], \quad (2.48)$$

where $\tilde{m}_j = m_j \mathbf{v}_j \sigma_t^2 / (\sigma_t^2 \mathbf{v}_j^2 + \sigma_{\bar{x}}^2)$. Hence, Eq. (2.38) can be eventually written as

$$e^{-iE_j T + \mathbf{v}_j \mathbf{P}_j T} \int dp^3 \int dx^3 e^{i\bar{x}\bar{p}} G(\bar{x}; \mathbf{L}_j) F_j(\bar{p}; \mathbf{P}_j). \quad (2.49)$$

Here G , centred at $\mathbf{L}_j = \mathbf{L} - \mathbf{v}_j T$, has width $\sigma_x^2 = \sigma_t^2 \mathbf{v}_j^2 + \sigma_{\bar{x}}^2$; and that for F_j , centred at $\mathbf{P}'_j = \Delta \mathbf{P}_j$, is σ_p . Additionally, $\Delta = 1 + 4\sigma_x^2 \sigma_p^2$, such that the saddle point from Eq. (2.44) is at \mathbf{P}_j . In fact, if all the input distributions are Gaussian distributed and both \bar{x} and \bar{p} are linear dependent, F_j and G will also be Gaussian distributed with some width σ_p and σ_x , respectively.

Neutrinos Represented Directly

Alternative from representing the Fock-PS by states entangled to the neutrino system, we represent it by the neutrinos directly in this section. In this case, we need to leave $y = y_2 - y_1$ and p_ν non-integrated. However, as demonstrated in this section, this particular representation does not allow us to explicitly account for uncertainties related to the external particles and the internal vertex as the previous representation. Instead, we can only treat them as effectively as either spatial-temporal or energy-momentum uncertainties, but not both. Hence, for the purpose of investigating neutrino decoherence concerning these two types of uncertainties, the previous representation will be applied in the following chapters. Nevertheless, it's worth noting that the representation presented in this subsection remains compatible with our overall framework, yielding equivalent effects. In fact the difference between this representation and the previous one is similar to the difference between the density matrix formalism and the Wigner quasi-probability distribution. The underlying argument is: while it can be more intuitive to write the direct representation (density matrix) in either the momentum or coordinate space, the interference pattern between eigenstates can be straightforwardly seen using the indirect representation (Wigner distribution) on the phase space.

The above statement may be demonstrated by following Eq. (2.36):

$$A_{2,j}(T, \mathbf{L}, \mathbf{P}) = \int d^4 y_1 \int d^4 y_2 \int \frac{d^4 p_\nu}{(2\pi)^4} \Delta(p_\nu) e^{-i p_\nu (y_1 - y_2)} \\ \times \int d^4 x_1 g_P(x_1) \tilde{F}_P(y_1 - x_1) e^{i P_P (y_1 - x_1)} \int d^4 x_2 g_D(x_2) \tilde{F}_D(y_2 - x_2) e^{-i P_D (y_2 - x_2)}, \quad (2.50)$$

where $\Delta(p_\nu)$ is the neutrino propagator in the momentum space. In this formalism, the WPs at the production and detection site in coordinate space are

$$\tilde{F}_{P_j}(y_1 - x_1) e^{i P_P (y_1 - x_1)} \simeq \int d^3 p F_{P_j}(\vec{p}) e^{-i (y_1^0 - x_1^0) \xi_P(\vec{p}) + i (\mathbf{y}_1 - \mathbf{x}_1) \vec{p}}, \quad (2.51)$$

$$\tilde{F}_{D_j}(y_2 - x_2) e^{-i P_D (y_2 - x_2)} \simeq \int d^3 p' F_{D_j}(\vec{p}') e^{-i (y_2^0 - x_2^0) \xi_D(\vec{p}') + i (\mathbf{y}_2 - \mathbf{x}_2) \vec{p}'}. \quad (2.52)$$

Here, P_P and P_D are the saddle points of $F_{P_j}(\vec{p})$ and $F_{D_j}(\vec{p}')$, respectively. Furthermore, under the assumption that the energy loss during the neutrino propagation is negligible, we have $P_P = P_D \simeq P$. Therefore, after integrating over x_1 and x_2 , Eq. (2.50) becomes

$$\int d^4 y \left\{ \int d^4 y_1 I_P(y_1; P_P) I_D(y_1 - y; P_D) e^{-[x_P(y_1) - x_D(y_1 - y)]} \right\} e^{i P y} \tilde{\Delta}(y), \quad (2.53)$$

where $y = y_1 - y_2$. Moreover, $\tilde{\Delta}(y)$ is the Fourier transformation of the propagator, or the two point function with distance y of the neutrino. Here, with the help of Property 5 in Appendix A, I_P and I_D results from the convolutions between the coordinate uncertainties of the external

states and the vertices:

$$I_P(y_1; P)e^{iP[y_1 - x_P(y_1)]} = \int d^4x_1 g_P(x_1) \tilde{F}_{Pj}(y_1 - x_1) F'_P(y_1^0 - x_1^0) e^{iP(y_1 - x_1)} \quad (2.54)$$

$$I_D(y_2; P)e^{-iP[y_2 - x_D(y_2)]} = \int d^4x_2 g_D(x_2) \tilde{F}_{Dj}(y_2 - x_2) F'_D(y_2^0 - x_2^0) e^{-iP(y_2 - x_2)}. \quad (2.55)$$

In fact, they represent the total coordinate uncertainties for the production and detection site. Finally, the total coordinate uncertainty within the large bracket in Eq. (2.53), comes from the width of the convolution function $(I_P * I_D)(y)$, or equivalently, $((g_P * \tilde{F}_{Pj} F'_P) * (g_D * \tilde{F}_{Dj} F'_D))(y)$. Moreover, with the association and commutation property for convolution, the total coordinate width may be rewritten as $(G * \tilde{F}_{Pj}^{\text{tot}} * \tilde{F}_{Dj}^{\text{tot}})(y)$, where G is in Eq. (2.39), $\tilde{F}_{Pj}^{\text{tot}} = \tilde{F}_{Pj} F'_P$ and $\tilde{F}_{Dj}^{\text{tot}} = \tilde{F}_{Dj} F'_D$.

Chapter 3

The Layer Structure

Contents

3.1 Microscopic Layer (Layer 1): QFT Transition Amplitude	28
3.2 Microscopic Layer (Layer 1): Quasi-Transition Probability	31
3.3 Physical Layer (Layer 2): Transition Probability	34
3.4 Measurement Layer (Layer 3): Transition Probability	38

Following the QFT description for calculating neutrino oscillation in the previous Sec. 2.2.2, we have singled out the neutrino system while shuffling the environmental effect into weighting functions w.r.t. the PS integration. Note that even though the PS does not inherently include a temporal dimension, the kinematics of the states involved are time-dependent. Thus, when we refer to “PS variables” we implicitly include a temporal component. In this chapter, our focus lies on the structural aspects of the PS during the calculation of the FTP. We refer to this structure as the “layer structure”, which consists of three distinct layers. Vertically, these layers include the microscopic layer, the physical layer, and the measurement layer. Horizontally, each layer represents a PS composed of space-time and momentum variables, collectively determining the kinematics of the neutrinos comprehensively.

The microscopic layer is closely related to the theories found in the existing literature, such as [15–19, 24–28, 31–34]. These theories can be represented using either the Fock-PS or the Wigner-PS, where Fock states and the Wigner quasi-probability distribution are employed, respectively. With the layer structure, we can comprehensively account for the decoherence effect resulting from information loss to the environment, from a microscopic to a macroscopic level. Differing from existing literature that also calculates neutrino decoherence at a macroscopic level [34, 38], our primary focus is on classifying and understanding decoherence within a generic framework. Eventually, neutrino decoherence for continuously emitted neutrinos is primarily parameterized by four uncertainties within the layer structure. These uncertainties encompass

coordinate/momentum uncertainties on the microscopic layer (quantum effects quantified by σ_x/σ_p), as well as those on the physical layer (macroscopic effects such as energy resolution or neutrino production profile σ_L/σ_E), providing an interface between microscopic mechanisms and the macroscopic experiments. In the case of non-continuously emitted neutrinos, an additional temporal uncertainty on the physical layer, denoted as σ_T , comes into play.

In Fig. 3.1, we present the layered structure designed for computing the expectation value of a given observable. This structure is composed of three layers of S, ranging from the microscopic level to the macroscopic level. These layers are denoted as the “microscopic layer” (Layer 1), the “physical layer” (Layer 2), and the “measurement layer” (Layer 3). As introduced earlier, this structural framework integrates the concept of an open quantum system into the QFT framework while accounting for statistical effects relevant to practical measurements.

Layer 1, the “microscopic layer,” is where quantum effects come into play. This layer accommodates phenomena like the superposition of states within the Hilbert space. It’s important to note that, owing to the uncertainty principle, both coordinate and momentum uncertainties cannot simultaneously be zero. These uncertainties are parameterized as σ_p and σ_x , and are generally independent of each other. The former accounts for uncertainties arising from external states on the mass-shell, described by the WPs in momentum space. The latter characterizes uncertainties from the vertices in coordinate space, representing how non-point-like the effective vertices are in a simplified diagram that includes only the external states and the neutrino propagator, as exemplified in Fig. 2.2.

Layer 2, the “physical layer”, reflects our limited knowledge of the system within the classical regime. Here, probability is summed (integrated) over, instead of the amplitudes. The uncertainties on this layer include those inherited from the first layer, along with additional macroscopic uncertainties. These additional uncertainties may be parameterized as the energy uncertainty (σ_E), for aspects like the energy resolution and how correct the energy reconstruction models is; and the coordinate uncertainty (σ_E), which can encompass elements like the neutrino production profile. As we progress in the following sections, each layer will be introduced in context, and we will delve into specific examples contributing to σ_p , σ_x , σ_E and σ_L .

Let’s consider the double-slit experiment, where we observe the interference pattern by capturing a photograph as an analogy to illustrate our point: the two slits in the experiment correspond to uncertainties on the first layer, creating interference between wavefunctions. In contrast, the probability density function (PDF) that describes the resolution of the camera taking the photo belongs to the second layer. The former allows the superposition of states, while the latter is a classical effect. In the context of neutrino oscillation, even though the uncertainties on the second layer are macroscopic, we still observe quantum coherence. This can be attributed to the smallness of the neutrino mass splitting.

In the upcoming discussion, we will delve into the layered structure in a more formal manner, encompassing various aspects depicted in Fig. 3.1. This includes the representation of the PS and the layer-moving-operators (LMOs) denoted as \mathcal{LMO} , which connect each layer. Notably, a crucial point to emphasize is that, as we will demonstrate later, the uncertainty parameters on

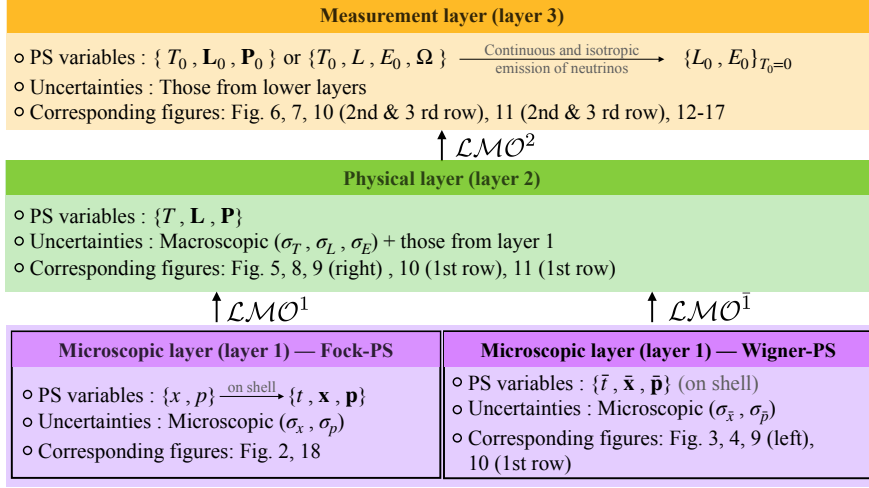


Figure 3.1: Illustration of the layer structure, and the notation of each phase space variable deciding the kinematics of states: t, \bar{t}, T, T_0 are the temporal variables; $\bar{x}, \bar{x}, \mathbf{L}, \mathbf{L}_0$ are the spatial variables; and $\bar{p}, \bar{p}, \mathbf{P}, \mathbf{P}_0$ are the momentum variables; E_0 is the energy and Ω represents the solid angle. The layers are linked by the layer-moving operator in Eq. (3.1), and the uncertainties are discussed in the text.

each layer correspond to the width of a weighting function within the \mathcal{LMO} . These weighting functions carry information about the environment entangled with the system. Consequently, these uncertainty parameters play a significant role in characterizing neutrino decoherence in experiments.

In our structural framework, different representation of the PS may be chosen for each layer. For example, the first layer may be represented using either the Fock-PS or the Wigner-PS. Concerning the representation of the second layer, we take the PS variables to be the expectation values of that from the first layer when neutrinos are massless (detailed explanations are found in Sec. ??). This representation is referred to as the "relativistic-PS". As for the third layer, we simply express the PS variables in terms of the expectation values obtained from the relativistic-PS. These values should align with the actual measurements. This statement must hold because, otherwise, should there be a dependence on the mass of the neutrino, the states would collapse to a specific neutrino mass state, resulting in no oscillation. Consequently, we label such representation as the "measurement-PS." Each PS encompasses its own temporal, coordinate, and momentum spaces, with energy implicitly derived from the momentum variables through the dispersion relation. The specific notations for these components can be found in Fig. 3.1. It's worth noting that while the layer structure has a broad applicability for calculating the expectation value of any measurement, our focus in this work is specifically on computing the FTP for neutrino oscillation. As shown in Fig. 3.1, the layers are linked by Layer-Moving Operators, denoted as \mathcal{LMO}^i , which transport a quantity, denoted as $B_i(x_i, p_i)$, such as the FTP or the transition amplitude, from Layer i to Layer $i + 1$. This transfer is achieved by integrating out the PS variables, specifically x_i and p_i , from Layer i while taking into account

additional uncertainties through the inclusion of a weighting function, denoted as W^i . This operation can be expressed as follows:

$$\mathcal{LMO}^i B_i(x_i, p_i) = \int d^4 x_i \int d^3 p_i [W^i(x_i, p_i; x_{i+1}, p_{i+1}) B_i(x_i, p_i)] = B_{i+1}(x_{i+1}, p_{i+1}). \quad (3.1)$$

In the context of the open quantum system, B_1 typically represents the system of interest, with W_1 encompassing the environment entangled with it.

Additionally, with respect to the notation of PS variables in Fig. 3.1, we have $x_1 = (t, \bar{x})$ and $p_1 = \bar{p}$ for the Fock-PS, $x_1 = (\bar{t}, \bar{x})$ and $p_1 = \bar{p}$ for the Wigner-PS (representing the PS for the occupation number of quasi-probability distributions), $x_2 = (T, \mathbf{L})$ and $p_2 = \mathbf{P}$ for the relativistic-PS, and $x_3 = (T_0, \mathbf{L}_0)$ and $p_3 = \mathbf{P}_0$ for the measurement-PS. Each of these PS representations will be explored in detail in the following subsections, specifically in the context of neutrinos.

Moreover, B_i on the first, second, and third layers represent the system of interest, the observable, and the measured value, respectively. Additionally, W_i serves as a PDF with the property:

$$\int d^4 x_i \int d^3 p_i W^i(x_i, p_i; x_{i+1}, p_{i+1}) = 1. \quad (3.2)$$

Additionally, if $B_i = e^{ix_i p_i} C_i(x_i, p_i)$, we have $\mathcal{LMO}^i e^{ix_i p_i} C_i = e^{ix_{i+1} p_{i+1}} C_{i+1}(x_{i+1}, p_{i+1})$ (see Appendix A for details), indicating that the uncertainty principle between x_i, p_i remains fulfilled on each layer. This is because \mathcal{LMO}^i along with $e^{ix_i p_i}$ means to first project everything onto the x_i or the p_i space, and then integrate over that space, while the projection process secures the uncertainty principle. In fact, this is exactly the case for the position-space representation of the wavefunction for some considered particle. In this case, $B_1(x, p) = e^{ixp} \tilde{\Delta}(p)$, where $\tilde{\Delta}(p)$ is the propagator in momentum space. We will demonstrate this explicitly for the case of neutrinos in Sec. 3.1. As a matter of fact, if $B_i = \exp(i\eta(x_i, p_i))$, for some phase structure $\eta(x_i, p_i)$, the LMO meets the condition of giving rise to a phase wash-out (PWO) effect described in Appendix A. The PWO effect is an averaging effect over the phase structure caused by the non-trivial width of the (normalized) weighting function, resulting in an additional suppression term Φ as

$$B_i(x_{i+1}, p_{i+1}) \Phi(x_{i+1}, p_{i+1}) = \mathcal{LOM}^i B_i(x_i, p_i), \quad (3.3)$$

where $|\Phi(x_{i+1}, p_{i+1})| \leq 1, \forall (x_{i+1}, p_{i+1})$. Only when the weighting function is symmetric with respect to the phase structure would Φ be a real function (see again Appendix A).

Furthermore, when there is a substructure of B , i.e. $B_i = \sum_{\nu} B_{\nu i}$, then the summation rule is simply

In fact, the normalization of W_i is not relevant at this point, as we will demonstrate in Sec. 4.1.1 that the FTP will inherently be normalized. Nonetheless, we define the weighting function as a PDF for the sake of examining its width, which relates to the concept of "width" described in Appendix A. Furthermore, x_{i+1} and p_{i+1} represent the variables on the next layer and are typically defined as the expectation values of x_i and p_i . Consequently, the width

of $W_1(x, p; T, \mathbf{L}, \mathbf{P})$, characterizing the microscopic quantum uncertainties, w.r.t. t , \bar{x} , and \bar{p} are denoted as σ_t , σ_x , and σ_p , respectively. Similarly, the width of $W_2(T, \mathbf{L}, \mathbf{P}; T_0, \mathbf{L}_0, \mathbf{P}_0)$, representing macroscopic statistical uncertainties, w.r.t. T , \mathbf{L} , and \mathbf{P} are denoted as σ_T , σ_L , and σ_P , respectively.

Additionally, if the weighting function can be expressed as $W^i(x_i - x_{i+1}, p_i - p_{i+1})$, the layer-moving operator becomes a convolution between W_i and B_i , as discussed in Appendix A. Moreover, \mathcal{LMO}^i is related to the calculation of the expectation value of the quantity B_i and the layer structure can be mathematically described as fiber bundles, as detailed in [39]. In simpler terms, when looking from upper layers to lower layers, each PS point (x_{i+1}, p_{i+1}) can be expanded into a complete PS composed of (x_i, p_i) on the lower layer. Additionally, on each layer, operations can map one state to another, depending on what is to be observed. Viewing the LMOs as vertical operators, these operators can be thought of as horizontal operators that keep the state within the same layer. Furthermore, if $B_i = e^{ix_i p_i} C_i(x_i, p_i)$, then we have $\mathcal{LMO}^i e^{ix_i p_i} C_i = e^{ix_{i+1} p_{i+1}} C_{i+1}(x_{i+1}, p_{i+1})$ (see Appendix A for details). This indicates that the uncertainty principle between x_i and p_i remains satisfied on each layer. This is because \mathcal{LMO}^i along with $e^{ix_i p_i}$ first projects everything onto the x_i or p_i space and then integrates over that space, ensuring the uncertainty principle is maintained. In fact, this would correspond to the position-space representation of the wavefunction for a given particle. In such cases, $B_1(x, p) = e^{ixp} \tilde{\Delta}(p)$, where $\tilde{\Delta}(p)$ represents the propagator in momentum space.

It is worth emphasising that, if $B_i = \exp(i\eta(x_i, p_i))$ for some phase structure $\eta(x_i, p_i)$, the LMO satisfies the condition for inducing a Phase Wash-Out (PWO) effect, as described in Appendix A. The PWO effect involves averaging over the phase structure due to the non-trivial width of the (normalized) weighting function, resulting in an additional suppression term Φ :

$$B_i(x_{i+1}, p_{i+1}) \Phi(x_{i+1}, p_{i+1}) = \mathcal{LMO}^i B_i(x_i, p_i), \quad (3.4)$$

where $|\Phi(x_{i+1}, p_{i+1})| \leq 1, \forall (x_{i+1}, p_{i+1})$. When the weighting function is symmetric with respect to the phase structure, Φ is a real function, otherwise, there will be an addition phase on top of η (see again Appendix A). In addition, when there is a substructure of B , i.e. $B_i = \sum_\nu B_{\nu i}$, the summation rule can be expressed as:

$$\mathcal{LMO}^i B_i = \sum_\nu \int d^4 x_i \int d^3 p_i W_i^\nu(x_i, p_i; x_{i+1}, p_{i+1}) B_{\nu i}(x_i, p_i). \quad (3.5)$$

Finally, to determine the measurement expectation value of the FTP, denoted as P_3 , we perform statistical averaging (\mathcal{LMO}^2) over the FTP on the physical layer (P_2). However, P_2 can be calculated in two ways: either by squaring the transition amplitude (A_2) on Layer 2 or by moving up (\mathcal{LMO}^1) the quasi-probability distribution (P_1) from the Wigner-PS. Here, A_2 is computed by integrating over all quantum-mechanical configurations of the environment (\mathcal{LMO}^1), moving the system of interest from the Fock-PS (A_1) up to the physical layer. On the other hand, \mathcal{LMO}^1 performs an effective statistical averaging over an effective FTP, which is the quasi-probability distribution representing the quantum-mechanical superposition effect

in the Wigner-PS [24, 40]. In summary:

$$\begin{aligned}
P_3(T_0, \mathbf{L}_0, \mathbf{P}_0) &= \mathcal{LMO}^2 P_2(T, \mathbf{L}, \mathbf{P}) = \mathcal{LMO}^2 \{A_2^*(T, \mathbf{L}, \mathbf{P}) A_2(T, \mathbf{L}, \mathbf{P})\} \\
&= \mathcal{LMO}^2 \{ \mathcal{LMO}^1 A_1^*(x, \bar{p}) \mathcal{LMO}^1 A_1(x, \bar{p}) \} \\
&= \mathcal{LMO}^2 \{ \mathcal{LMO}^{\bar{1}} P_1(\bar{t}, \bar{x}, \bar{p}) \}.
\end{aligned} \tag{3.6}$$

In the following sections, we will introduce each layer and its role in calculating the expectation value for the measurement of the FTP in the context of neutrino oscillation in vacuum.

3.1 Microscopic Layer (Layer 1): QFT Transition Amplitude

In this subsection, we apply the calculate of the transition amplitude on the Fock-PS with the QFT approach in Sec. 2.2.2 onto the layer structure. While QM can describe neutrino coherence and decoherence on the Fock-PS, it falls short in addressing several important questions, which the QFT approach can tackle effectively, as demonstrated in previous works [28, 31]. Furthermore, for the purpose of investigating quantum decoherence effects and their implications for fundamental physics, employing the QFT framework is essential, even for the scenario of vacuum propagation. This is because the weighting functions on the first layer may originate from uncertainties in the interactions occurring around the vertices. Moreover, to explicitly capture the influence of states entangled with neutrinos on these weighting functions, we apply the viewpoint of Sec. 2.2.2, where the PS on this layer is dictated by the states entangled to the neutrino.

Regarding the weighting functions, we treat the external particles as WPs, often referred to as the Jacob-Sachs model [41] in [31], following the approach outlined in Eq. (2.29). The WPs introduce a microscopic uncertainty parameter, denoted as σ_p , which is defined in the momentum space. σ_p encapsulates information such as the lifetime of the external particles [42] for neutrinos produced by decaying particles or the mean free path of processes preceding the production of neutrinos [43]. Additionally, regardless of the uncertainties associated with external particles, we account for the microscopic uncertainties in the interaction processes around the vertices through another parameter, σ_x . The value of σ_x depends on the internal states and the details of the scattering or collision process. In principle, it is possible to directly express the Fock-PS in the first layer in terms of neutrinos, as shown in Appendix 2.2.2. However, this approach would only yield an effective weighting function in either the energy-momentum space or the space-time coordinate space.

Applying results from Sec. 2.2.2, where only the neutrino momentum ($\bar{p} = \mathbf{q} - \mathbf{k} = \mathbf{k}' - \mathbf{q}'$) and traveling distance and time ($x = x_2 - x_1$) determined by the entangled states are left unintegrated, into the layer structure shows:

$$A_{2,\alpha\beta}(T, \mathbf{L}, \mathbf{P}) = \int d^3 p \int d^4 x F_j(\bar{p}; \mathbf{P}) G_x(x; X) A_{1,\alpha\beta}(x, \bar{p}), \tag{3.7}$$

In this expression, $F(\bar{p}; \mathbf{P})$ characterizes the PDF arising from the WPs of the external particles, while $G_x(x; X)$ represents a PDF associated with the vertices. Consequently, the layer-moving operator is given by:

$$\mathcal{LMO}^1 = \int d^3p \int d^4x F_j(\bar{p}; \mathbf{P}) G_x(x; X), \quad (3.8)$$

In this context, the product $F(p; P)G_x(x; X)$ serves as the weighting function, and the width of these uncertainties, σ_p and σ_x , are considered as the parameters of observation. The relationship between these parameters and the original uncertainties are outlined Fig. 2.3. Here, the notation $G_x(x; X)$ denotes that X is the expected value of x for the PDF $G_x(x)$, as well as for other functions in this paper.

In general, the transition amplitude on the first layer takes the form shown in Eq. (2.40), where all configurations of the internal energy of the neutrino propagator should, in principle, be included. However, since the measurement is performed on a macroscopic scale, we can treat the propagating neutrino as being on the mass shell. Consequently, the first-layer transition amplitude for neutrino oscillation becomes:

$$A_{1,\alpha\beta}(x, \bar{p}) = \sum_j U_{\alpha j}^* U_{\beta j} e^{-itE_j(\bar{p}) + i\bar{x}\bar{p}}. \quad (3.9)$$

It is worth noting that although we have ‘‘imposed’’ the on-shell approximation in this expression, it will be on-shell on the second layer, even if we choose not to do so. This is due to the fact that the variables on the second layer are macroscopic, while those on the first layer are microscopic. Consequently, the dynamics evolve into a classical regime, and we obtain the energy-momentum dispersion relation. Furthermore, we stress that e^{ipx} in $A_{1,\alpha\beta}$ ensures the preservation of the uncertainty principle all the way up to the measurement layer, as discussed previously.

Finally, we proceed to expand the neutrino energy around $\bar{p} = \mathbf{P}_j$, which serves as the saddle point of the overall weighting function in momentum space. We retain terms up to the first order, denoted as $E_j(\bar{p}) \simeq E_j + \mathbf{v}_j(\bar{p} - \mathbf{P}_j)$, where $E_j \equiv E_j(\mathbf{P}_j)$ and $\mathbf{v}_j \equiv \partial E_j(\bar{p}) / \partial \bar{p}|_{\bar{p}=\mathbf{P}_j} = \mathbf{P}_j / E_j$. Therefore, in accordance with Eq. (2.45), we obtain:

$$A_{2,j}(T, \mathbf{L}, \mathbf{P}) = e^{-iE_j T + i\mathbf{P}_j \mathbf{L}} \hat{\Phi}_j(\mathbf{L}, \mathbf{P}), \quad (3.10)$$

Here, \mathbf{L} and \mathbf{P} represent the second-layer phase space variables, such that $\mathbf{P}_j = \mathbf{P}_j(\mathbf{P})$ (the explicit relationship for the latter will be discussed in Section 3.3). In principle, a comprehensive analysis of weighting functions resulting in the neutrino decoherence phenomena is possible, providing insight into the underlying mechanisms. However, this would require exceptionally precise measurements encompassing a wide spectrum in both coordinate and momentum space, and an analysis that exceeds the scope of this paper. In this context, we investigate the weighting function through the width of the PDF, denoted as σ_x / σ_p for $G(\bar{x}, \mathbf{L}_j) / F_j(\bar{p}, \mathbf{P}_j)$ in Eq. (3.11) below. If the weighting functions are symmetric, then $\hat{\Phi}_j(\mathbf{L}, \mathbf{P})$ is real, as explained in Appendix A. Otherwise, an additional parameter for the phase of $\hat{\Phi}_j(\mathbf{L}, \mathbf{P})$ would be required.

Additionally, it’s important to note that σ_x and σ_p do not represent the total momentum

and coordinate uncertainty of the system. In fact, the total coordinate uncertainty is calculated in Appendix 2.2.2, revealing that it arises from the convolution between the coordinate distributions at the production and detection sites. Specifically, the total coordinate distribution for each production/detection site is the result of convolving $g_P(x_1)/g_D(x_2)$ with the momentum distributions of the external states projected onto the coordinate space ($\tilde{F}_{P/D}^{\text{tot}}$). In other words, the total coordinate uncertainty can be expressed as $(g_P * \tilde{F}_P^{\text{tot}})(g_D \tilde{F}_D^{\text{tot}})$, where $*$ denotes convolution between two functions, as noted in Table A.1. This concept is illustrated at the vertices in Fig. 2.2: while the external particles contribute to some coordinate uncertainties by mapping the momentum uncertainties onto the coordinate space (represented by the individual blue and green circles), the internal process introduces additional spatial uncertainties (represented by the inner solid circle lines), resulting in a total coordinate uncertainty (represented by the outer dashed lines) that surpasses the individual uncertainties.

Specifically, for the case of Gaussian WPs, the formalism for $F_j(\bar{p}, \mathbf{P})$ is widely established in the literature, as found in references such as [28, 31, 32]. For the sake of demonstration, we also adopt a generic Gaussian form for the weighting function on the Fock-PS. Although, in general, the WPs can take any shape. Additionally, we integrate out x^0 in Eq. (3.7) for later convenience. Consequently, following the discussion in Sec. 2.2.2, we arrive at the following expression:

$$A_{2,j}(T, \mathbf{L}, \mathbf{P}) = e^{-iE_j T + i\mathbf{v}_j \mathbf{P}_j T} \int dp^3 \int dx^3 e^{i\bar{x}\bar{p}} G(\bar{x}; \mathbf{L}_j) F_j(\bar{p}; \mathbf{P}_j). \quad (3.11)$$

Here, the functions $G(\bar{x}; \mathbf{L}_j)$ and $F_j(\bar{p}; \mathbf{P}_j)$ are given by:

$$G(\bar{x}; \mathbf{L}_j) \propto \exp\left[-\frac{(\bar{x} - \mathbf{L}_j)^2}{4\sigma_x^2}\right], \quad F_j(\bar{p}; \mathbf{P}_j) \propto \exp\left[-\frac{(\bar{p} - \Delta \mathbf{P}_j)^2}{4\sigma_p^2}\right], \quad (3.12)$$

where $\mathbf{L}_j = \mathbf{L} - \mathbf{v}_j T$ and $\Delta = 1 + 4\sigma_x^2 \sigma_p^2$.

Ultimately, σ_x encompasses all individual uncertainties, both temporal and coordinate, associated with production and detection, in a convolutional manner. Consequently, the dominant factor will be the larger one among them. On the other hand, σ_p combines the momentum uncertainties of production and detection through a product relationship, as indicated in Table A.1. However, at each site, the total momentum uncertainty arises from the convolution of momentum uncertainties of individual external states, implying that the largest one among them will dominate. This relationship aligns with the findings of Ref. [32], assuming Gaussian distributions. Again, the normalization of the weighting functions is irrelevant at this point, as we will later demonstrate that the FTP will automatically normalize on the measurement layer with the definition in Eq. (4.4). With the Gaussian distributions incorporated, we can easily determine that:

$$\hat{\Phi}_j(\mathbf{L}, \mathbf{P}) \propto e^{i\mathbf{P}_j \mathbf{L}_j} \exp\left[-\mathbf{P}_j^2 \Delta \sigma_x^2 - \frac{\mathbf{L}_j^2 \sigma_p^2}{\Delta}\right]. \quad (3.13)$$

Thus, when $\sigma_x \ll 1/(2\sigma_p)$, that is, when the width of the inner solid line in Fig. 2.2 is significantly smaller than that of the blue/green circle's width, σ_x can be safely neglected, and vice versa.

3.2 Microscopic Layer (Layer 1): Quasi-Transition Probability

In this section, we perform calculations to determine the quasi-probability distribution (or Wigner function, as referred to in some literature, e.g., [40]) of the FTP on the Wigner-PS representation. These distributions serve as a connection between quantum mechanics (or quantum field theory, as in this context) and statistical probability distributions, enabling the calculation of expectation values through direct PS integration. Furthermore, in Section 4.1.2, we will demonstrate the insightfulness and utility of viewing state decoherence as a phase wash-out (PWO) effect from the perspective of the Wigner-PS representation. Although we do not directly obtain the quasi-probability distribution $P_{\bar{1}}$ through the Wigner transformation, we arrive at the same formalism by performing a change of variables that satisfies Eq. (3.6). This means that we find $P_{\bar{1}}$ in a way that fulfills the following relation:

$$\begin{aligned} P_{2,\alpha\beta} &= \int d^3\bar{x} \int d^3\bar{p} P_{\bar{1}}(\bar{x}, \bar{p}) = A_{2,\alpha\beta} A_{2,\alpha\beta}^\dagger \\ &= \sum_{j,k} U_{\alpha j}^* U_{\beta j} U_{\alpha k} U_{\beta k}^* e^{-i(E_j - E_k)T + i(\mathbf{v}_j \mathbf{P}_j - \mathbf{v}_k \mathbf{P}_k)T} A_{2,j} A_{2,k}^\dagger, \end{aligned} \quad (3.14)$$

Here, $A_{2,j/k}$ is given by Eq. (3.11). Thus, for a $P_{\bar{1}}$ of the form:

$$P_{\bar{1}} = \sum_{j,k} U_{\alpha j}^* U_{\beta j} U_{\alpha k} U_{\beta k}^* e^{-i(E_j - E_k)T + i(\mathbf{v}_j \mathbf{P}_j - \mathbf{v}_k \mathbf{P}_k)T} P_{\bar{1},jk}, \quad (3.15)$$

Eq. (3.14) implies that

$$\int d^3\bar{x} \int d^3\bar{p} P_{\bar{1},jk}(\bar{x}, \bar{p}) = \int d^3x \int d^3p e^{i\bar{p}\bar{x}} G(x) F_j(\bar{p}) \int d^3x' \int d^3p' e^{-i\bar{p}'\bar{x}'} G^*(x') F_k^*(\bar{p}'). \quad (3.16)$$

The right-hand side of this equation involves the mixing of two phase-spaces, (\bar{x}, \bar{p}) and (\bar{x}', \bar{p}') , while the left-hand side does not.

Therefore, $P_{\bar{1},jk}$ represents the quasi-probability distribution, indicating the occupation number of having both the j th and the k th mass eigenstates simultaneously on the Wigner-PS. This equation is achieved by replacing $(\bar{x}, \bar{x}') \rightarrow (\bar{x} = \frac{1}{2}(\bar{x} + \bar{x}'), \Delta\bar{x} = \bar{x} - \bar{x}')$ and $(\bar{p}, \bar{p}') \rightarrow (\bar{p} = \frac{1}{2}(\bar{p} + \bar{p}'), \Delta\bar{p} = \bar{p} - \bar{p}')$. Consequently, Eq. (3.16) can be expressed as:

$$P_{\bar{1},jk}(\bar{x}, \bar{p}) = \tilde{W}_{jk}^G(\bar{x}, \bar{p}) \tilde{W}_{jk}^F(\bar{x}, \bar{p}). \quad (3.17)$$

Here $\tilde{W}_{jk}^G(\bar{x}, \bar{p})$ and $\tilde{W}_{jk}^F(\bar{x}, \bar{p})$ take the form of the Wigner quasi-probability distribution as

follows:

$$\begin{aligned}\tilde{W}_{jk}^G(\bar{x}, \bar{p}) &= \int d^3(\Delta\bar{x}) e^{i\Delta\bar{x}\bar{p}} G(\bar{x} + \frac{1}{2}\Delta\bar{x}; \mathbf{L}_j) G^*(\bar{x} - \frac{1}{2}\Delta\bar{x}; \mathbf{L}_k), \\ \tilde{W}_{jk}^F(\bar{x}, \bar{p}) &= \int d^3(\Delta\bar{p}) e^{i\Delta\bar{p}\bar{x}} F_j(\bar{p} + \frac{1}{2}\Delta\bar{p}; \mathbf{P}_j) F_k^*(\bar{p} - \frac{1}{2}\Delta\bar{p}; \mathbf{P}_k).\end{aligned}\quad (3.18)$$

In this context, $\mathcal{LMO}^{\bar{1}} = \int d^3\bar{x} \int d^3\bar{p}$ simply involves integrating over the Wigner-PS, and the FTP on this layer is represented by the quasi-probability distribution $\tilde{W}_{jk}^G \tilde{W}_{jk}^F$, encompassing both W_1 and B_1 as described in Eq. (3.1). In particular, if we assume that all weighting functions take Gaussian forms on the Fock-PS as given in Eq. (3.12), the quasi-probability distributions become:

$$\begin{aligned}\tilde{W}_{jk}^G(\bar{x}, \bar{p}) &\propto \exp[i\bar{p}(\mathbf{L}_j - \mathbf{L}_k)] \exp\left[-\frac{(\bar{x} - \bar{\mathbf{L}}_{jk})^2}{2\sigma_x^2} - 2\bar{p}^2\sigma_x^2\right], \\ \tilde{W}_{jk}^F(\bar{x}, \bar{p}) &\propto \exp[i\bar{x}\Delta(\mathbf{P}_j - \mathbf{P}_k)] \exp\left[-\frac{(\bar{p} - \Delta\bar{\mathbf{P}}_{jk})^2}{2\sigma_p^2} - 2\bar{x}^2\sigma_p^2\right],\end{aligned}\quad (3.19)$$

where $\bar{\mathbf{L}}_{jk} = \frac{\mathbf{L}_j + \mathbf{L}_k}{2}$ and $\Delta\bar{\mathbf{P}}_{jk} = \frac{\mathbf{P}_j - \mathbf{P}_k}{2}$. After moving the FTP up to the physical layer by integrating over the Wigner-PS, there will be a PWO effect that suppresses the plane wave term on the physical layer. Moreover, the strength of the PWO effect is determined by the width of the weighting function relative to the wavelength of the phase structure, which is $\mathbf{P}_j - \mathbf{P}_k$ for \bar{x} and $\mathbf{L}_j - \mathbf{L}_k$ for \bar{p} in this case. Essentially, the wider the weighting function relative to the wavelength of the phase structure, the greater the suppression caused by the PWO effect will be. This can also be viewed as counting the number of periods determined by the phase structure (e.g., $2\pi/(\mathbf{P}_j - \mathbf{P}_k)$ is one period in \bar{x}) within a certain width of the weighting function. This quantity is referred to as the phase density. Hence, a higher phase density results in more damping from the PWO effect.

Fig.3.2 and Fig.3.3 serve as examples to illustrate the quasi-probability distribution on the Wigner-PS before integrating out the phase-space variables, which would ultimately lead to a PWO effect on the physical layer after the integration. In particular, Fig.3.3 provides a 2D contour plot, illustrating the projection of 3D plots like Fig.3.2. The shaded and non-shaded circles within the plot represent contour lines corresponding to one standard deviation of a Gaussian distribution as described in Eq. (3.19). In both plots, the alternation between positive and negative values (red and blue circles) within the circles indicates the phase density within one standard deviation of the weighting function. A higher phase density within this range results in a larger PWO effect. The left plot corresponds to a specific time T_{left} and a certain width $\sigma_p = \sigma_x = \sigma_{\text{left}}$ for the weighting functions. The middle plot maintains the same width but features a longer propagation time, i.e., $T_{\text{middle}} > T_{\text{left}}$. On the other hand, the right plot presents two scenarios for the width resulting in the same effect: $\sigma_p = \sigma_x = \sigma_{\text{right}} = 0.325\sigma_{\text{left}}$ and $\sigma_p = \sigma_x = \sigma_{\text{right}} = 1.376\sigma_{\text{left}}$, both with $T_{\text{middle}} = T_{\text{right}}$.

Comparing the left and middle plots of Fig.3.3, we observe that as time progresses, although the FTP of the two mass eigenstates separate, the width of the overlapping profiles remains

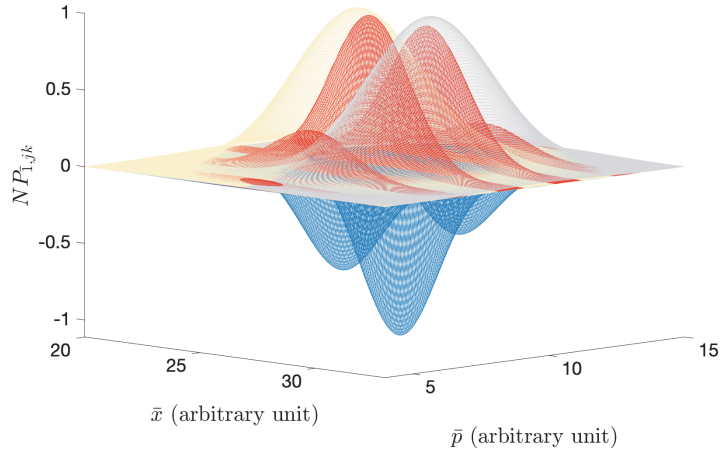


Figure 3.2: An illustration of the quasi-probability distribution in Eq. (3.19) on layer 1 in the Wigner-PS assuming Gaussian distributed weighting functions scaled by N (as explained in the text, the normalization of the distributions is irrelevant, just the width and shape are). The yellow/grey areas represent $P_{1,jj}/P_{1,kk}$, and the red/blue area are for the positive/negative values of $P_{1,jk}$.

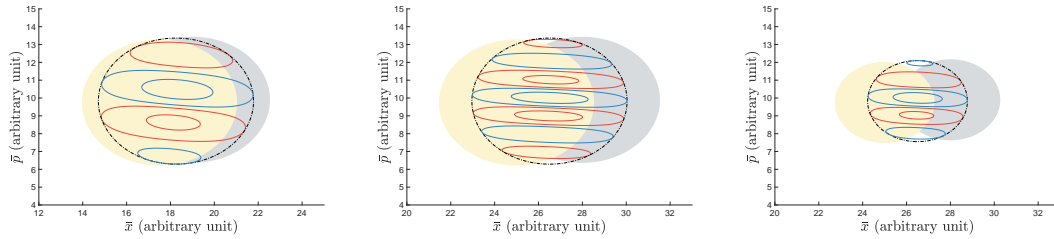


Figure 3.3: An illustration of the quasi-probability distribution in Eq. (3.19) on layer 1 in the Wigner-PS assuming Gaussian distributed weighting functions. These plots show the projection of 3D plots like Fig. 3.2 onto 2D plots. The edge of the shaded areas, the (outer) thick solid lines and the dashed lines are contour lines for the distributions within two standard deviations, while the (inner) thin lines are for one standard deviation. The shaded areas represent $P_{1,jj}$ and $P_{1,kk}$, the red/blue lines are for the positive/negative values of $P_{1,jk}$, and the black dashed line shows the weighting function for $P_{1,jk}$. The three plots differ by the traveling time (T_{plot}) and width ($\sigma_{\text{plot}} = \sigma_p = \sigma_x$) as: $T_{\text{left}} < T_{\text{middle}} = T_{\text{right}}$ and $\sigma_{\text{left}} = \sigma_{\text{middle}}$, also $\sigma_{\text{right}} = 0.325 \sigma_{\text{left}}$ or $1.376 \sigma_{\text{left}}$.

constant. However, the phase density increases, consequently intensifying the PWO effect. On the other hand, since the width of the weighting function is determined by $\sigma_{\bar{x}}^2 = \sigma_x^2/(1 + 4\sigma_x^2\sigma_p^2)$ for \bar{x} and $\sigma_{\bar{p}}^2 = \sigma_p^2/(1 + 4\sigma_x^2\sigma_p^2)$ for \bar{p} , the maximum value of $\sigma_{\bar{x}}^2\sigma_{\bar{p}}^2$ is $1/4$. This signifies that the quasi-probability distribution is localized, and the uncertainty principle is inherently maintained. Consequently, there exist two solutions for σ_{right} , each corresponding to a value of $\sigma_{\bar{x}} = \sigma_{\bar{p}} < 1/2$. Moreover, a reduction in $\sigma_{\bar{x}}$ and $\sigma_{\bar{p}}$ would also decrease the phase density, ultimately mitigating the PWO effect. Note that on the Wigner-PS, when the quasi-probability distribution becomes localized at a single point, it effectively describes a classical monochromatic field [40].

3.3 Physical Layer (Layer 2): Transition Probability

In this section, we transition to the physical layer, where we must account for experimental uncertainties in addition to the existing ones from layer 1. To simplify matters, we assume isotropic neutrino emission. The supplementary uncertainties introduced through the weighting function on this layer encompass the macroscopic energy uncertainty, denoted as σ_E , and the macroscopic coordinate uncertainty, denoted as σ_L . The former summarizes energy-related uncertainties, such as the energy resolution of the experiment ($\sigma_E \propto 1/\sqrt{E_0}$) and sophistication of the energy reconstruction models (e.g., see [44, 45]). The latter concludes uncertainties related to the propagation distance, which can arise from various sources, such as: the core size and distribution of multiple reactors for reactor neutrinos; the length of the decay pipe and the velocity of parent particles before they decay into neutrinos for accelerator neutrinos; or even exotic effects that introduce uncertainties in the time and distance a neutrino travels before detection, such as spacetime fluctuations.

Before accounting for the additional uncertainties on layer 2, we must first transfer the FTP from layer 1 to this layer. This can be accomplished by moving from the Fock-PS with the following expression:

$$P_{2,jk}(T, \mathbf{L}, \mathbf{P}) = e^{-i(E_j - E_k)T + i(\mathbf{P}_j - \mathbf{P}_k)L} \hat{\Phi}^*(\mathbf{L}_k; P_k) \hat{\Phi}(\mathbf{L}_j; P_j), \quad (3.20)$$

where the FTP is

$$P_{2,\alpha\beta}(T, \mathbf{L}, \mathbf{P}) = \sum_{j,k} U_{\alpha j}^* U_{\beta j} U_{\alpha k} U_{\beta k}^* P_{2,jk}(T, \mathbf{L}, \mathbf{P}). \quad (3.21)$$

Alternatively, we can also move from the Wigner-PS as follows:

$$P_{2,jk}(T, \mathbf{L}, \mathbf{P}) = \int d^3\bar{x} \int d^3\bar{p} \tilde{W}_{jk}^G(\bar{x}, \bar{p}) \tilde{W}_{jk}^F(\bar{x}, \bar{p}). \quad (3.22)$$

Both approaches yield the same result, serving as a valuable consistency check. When we utilize Gaussian distributions for the first layer as described in Eq. (3.12), we arrive at the following expression:

$$P_{2,jk}(T, \mathbf{L}, \mathbf{P}) \propto e^{-i(E_j - E_k)T + i(\mathbf{P}_j - \mathbf{P}_k)L} \exp[-(\mathbf{P}_j^2 + \mathbf{P}_k^2)\sigma_{\bar{x}}^2 - (\mathbf{L}_j^2 + \mathbf{L}_k^2)\sigma_{\bar{p}}^2]. \quad (3.23)$$

This result can be obtained from either Eq.(3.13) or Eq.(3.19), and it's worth noting that it's helpful to express the widths in terms of $\sigma_{\bar{x}} = \Delta$, σ_x and $\sigma_{\bar{p}} = \sigma_p/\Delta$, where $\Delta = 1 + 4\sigma_x^2\sigma_p^2$.

So far, we have not specified the relationship between the second-layer momentum variable \mathbf{P} in the relativistic-PS and the expectation value of momentum \mathbf{P}_j for each mass eigenstate. We will now derive this relationship by comparing the massless case with the small mass case. In the massless case, for a certain energy E , we have $E = |\mathbf{P}|$. However, for nonzero neutrino mass, some of the energy, denoted as δE_j , will be used to account for the mass, and this energy distribution is constrained by the uncertainty of the energy on the first layer. In other words, we can think of this as having $\mathbf{P}_j(E')$ instead of $E_j(\bar{p})$ while deriving Eq. (3.10), with E being the mean of energies E' of the neutrinos given by the external particles in the first layer.

Therefore, we can express this relationship as:

$$|\mathbf{P}_j| \equiv E - \delta E_j. \quad (3.24)$$

Expanding \mathbf{P}_j with respect to m_j and keeping only the leading order, we obtain:

$$\mathbf{P}_j \simeq \mathbf{P} - \vec{\xi}_j \frac{m_j^2}{2E} = \vec{\xi}_p E - \vec{\xi}_j \frac{m_j^2}{2E}, \quad (3.25)$$

where $\vec{\xi}_p = \mathbf{P}/E = \mathbf{P}/|\mathbf{P}|$, ensuring that $|\vec{\xi}_p|^2 = |\vec{\xi}_j|^2 = 1$. This allows us to identify δE_j , by substituting Eq. (3.25) to Eq. (3.24) with $|P_j| = \sqrt{P_j^2}$, as:

$$\delta E_j = E - |\mathbf{P}_j| \simeq \vec{\xi}_p \vec{\xi}_j \frac{m_j^2}{2E} \quad (3.26)$$

to the lowest order in m_j . The actual energy carried by the mass eigenstate is determined by the dispersion relation:

$$E_j = \sqrt{|\mathbf{P}_j|^2 + m_j^2} \simeq E - \delta E + \frac{m_j^2}{2E} \simeq E + \frac{m_j^2}{2E} \left(1 - \vec{\xi}_p \vec{\xi}_j\right). \quad (3.27)$$

Hence, when $\vec{\xi}_p \vec{\xi}_j = 1$, which is the case where all mass eigenstates and the massless case are co-linear, we have equal energy of mass states. Conversely, when $\vec{\xi}_p \vec{\xi}_j = 0$, we have equal momentum modulus. To have exact equal momentum, we would need $\vec{\xi}_j = \vec{0}$. However, both of these extreme case would contradicts Lorentz invariance [46, 47]. Additionally, we can derive the group velocity as:

$$\mathbf{v}_j = \frac{\mathbf{P}_j}{E_j} \simeq \left(\vec{\xi}_p E - \vec{\xi}_j \frac{m_j^2}{2E} \right) \frac{1}{E} \left(1 + \frac{m_j^2}{2E^2} (1 - \vec{\xi}_p \vec{\xi}_j) \right)^{-1} \simeq \vec{\xi}_p \left(1 - \frac{m_j^2}{2E^2} \right). \quad (3.28)$$

With this approximation, Eq. (3.23) becomes:

$$P_{2,jk}(T, L, E) = e^{i\psi'_{jk}(T,L,E)} D'_x(T, L, E) D'_p(E), \quad (3.29)$$

where the phase structure, the momentum weighting function, and the coordinate weighting function are given by equations (3.30), (3.31), and (3.32) below, respectively.

$$\psi'_{jk}(T, L, E) = -\frac{\Delta m_{jk}^2}{2E}(T(1-\eta) + L\eta), \quad (3.30)$$

$$D'_p(E) \propto \exp \left[-2\sigma_{\vec{x}}^2 \left(E\vec{\xi}_p - \frac{m_j^2\vec{\xi}_j + m_k^2\vec{\xi}_k}{2E} \right)^2 - \frac{\sigma_{\vec{x}}^2}{2} \left(\frac{m_j^2\vec{\xi}_j - m_k^2\vec{\xi}_k}{2E} \right)^2 \right], \quad (3.31)$$

$$D'_x(T, L, E) \propto \exp \left[-\sigma_{\vec{p}}^2 \left(\frac{L\Delta m_{jk}^2}{2\sqrt{2}E^2} \right)^2 - 2\sigma_{\vec{p}}^2 \left(1 - \frac{m_j^2 + m_k^2}{2E^2} \right) (T-L)^2 \right], \quad (3.32)$$

Here, we have taken $\vec{\xi}_j = \vec{\xi}_k \equiv \vec{\xi}$ and $\eta = \vec{\xi}\vec{\xi}_p = \vec{\xi}\vec{\xi}_L$ as the alignment factor. In particular, terms such as the second term in the brackets of Eq. (3.31) will be cancel out by normalization. This will be shown in Sec. ??.

For experiments with continuously emitted neutrinos over a sufficiently long period of time, we integrate out the time variable T . In this scenario, ψ'_{jk} is replaced by ψ_{jk} , and D'_x is replaced by D_x in the equation above, where:

$$\psi_{jk}(L, E) = -\frac{\Delta m_{jk}^2 L}{2E}, \quad (3.33)$$

$$D_x(L, E) \propto \exp \left\{ -\sigma_{\vec{p}}^2 \left(\frac{L\Delta m_{jk}^2}{2\sqrt{2}E^2} \right)^2 - \frac{1}{2\sigma_{\vec{p}}^2} \left[\frac{\Delta m_{jk}^2}{2E}(1-\eta) \right]^2 \right\}. \quad (3.34)$$

Note that ψ_{jk} being independent of $\vec{\xi}_j$ and $\vec{\xi}_k$ implies that regardless of whether we have "equal energy," "equal momentum," or anything in between, the same phase structure results when we have no temporal information. Furthermore, in the limit where $\sigma_{\vec{x}} \sim 0$, we obtain the standard decoherence formula (3.35), which is in line with existing literature. [32], namely

$$P_{2,jk}(L, E) \simeq \exp \left[i \frac{\Delta m_{jk}^2 L}{2E} \right] \exp \left[- \left(\frac{L}{L_{kj}^{\text{coh}}} \right)^2 - (1-\eta) \left(\frac{\Delta m_{jk}^2}{2\sqrt{2}E\sigma_{\vec{p}}} \right)^2 \right], \quad (3.35)$$

where

$$L_{kj}^{\text{coh}} = \frac{2\sqrt{2}E^2}{|\Delta m_{kj}^2|\sigma_{\vec{p}}} \quad (3.36)$$

for freely propagating neutrinos.

So far, we have focused on the transmission of weighting functions from the first layer to the second layer. However, before delving further into this, we will simplify our discussion by introducing a change of variables. We will move from $T, \mathbf{L}, \mathbf{P}$ to $T, L = |\mathbf{L}|, E = |\mathbf{P}|, \Omega_L, \Omega_P$, where Ω_L and Ω_P represent the solid angles associated with \mathbf{L} and \mathbf{P} , respectively. With these new variables, the layer-moving operator from the physical layer to the measurement layer can

be expressed as:

$$\mathcal{LMO}^2 = \int dL \int dE \int d\Omega \int dT H_L(L; L_0) H_E(E; E_0) H_T(T; T_0) H_\Omega(\Omega; \Omega_0). \quad (3.37)$$

Assuming isotropic neutrino emission and a lack of temporal information, meaning we only consider uncertainties in E and L , we can express $P_{2,jk}$ as it moves to the third layer via

$$P_{3,jk}(L_0, E_0) \propto \int dL \int dE H_L(L; L_0) H_E(E; E_0) P_{2,jk}(L, E). \quad (3.38)$$

For a counting experiment, the transformation from the second layer to the third layer can be understood as a convolution between the FTP on the second layer (which includes uncertainties from the first layer) and the weighting function $H_X(X; X_0)$, which represents the PDF of the true value X for a measured value X_0 . Namely,

$$P_{3,jk}(X_0) = \int dX P_{2,jk}(X) H_X(X - X_0). \quad (3.39)$$

For instance, when considering the measured rate at L_0 , it doesn't solely account for neutrinos actually propagating the distance L_0 . Instead, it encompasses contributions from all possible distances within a time window, considering the uncertainty in time. In the case of continuous neutrino emission over a sufficiently long period of time, this time window is taken as infinite. Particularly, the coordinate uncertainty, represented by $H_L(L; L_0)$, arises from the convolution of the spatial PDF of the neutrino production process and the detection process. Therefore, the dominant source of uncertainty is typically the production PDF, which refers to the source profile or the PDF characterizing neutrino production, because the largest among these uncertainties will dominate.

Since Eq. (3.38) also results in a PWO effect, Fig. 3.4 is plotted in the same way as Fig. 3.3 such that the phase density of the weighting function can be visualized. However, unlike the case of the Wigner-PS in Fig. 3.3, the separation of $P_{2,jj}(\mathbf{L}, \mathbf{P})$ and $P_{2,kk}(\mathbf{L}, \mathbf{P})$ affects the width of $P_{2,jk}(\mathbf{L}, \mathbf{P})$ (black dotted circle) on the relativistic-PS. In Fig. 3.4 the time-dependent case for $P_{2,jk}$ on the physical layer is illustrated as an example. The phase structure is the same as Eq. (3.30), and the spatial uncertainty is the same as Eq. (3.32). Nonetheless, since the effect from D'_p is suppressed by the neutrino mass, in Eq. (3.31) we consider the second layer weighting function $H_E(E; E_0)$ solely for the energy uncertainty. Hence, with

$$P_{2jk}(T, L, E; E_0) = \exp \left[\frac{-(E - E_0)^2}{2\sigma_E^2} \right] D'_x(T, L, E) e^{i\psi'_{jk}(T, L, E)}. \quad (3.40)$$

we can show the contour lines in Fig. 3.4 for one standard deviation. To demonstrate how the time-dependent phase structure would be affected by the alignment η , Fig. 3.4 is plotted under two cases of η between ξ_p and $\xi = \xi_j = \xi_k$ in Eq. (3.25). In addition, due to the energy dependence of the group velocity in Eq. (3.28), we can also see that the heavier mass eigenstate $P_{2,jj}$ (the yellow shaded area) is a bit tilted at large T . In reality, however, this tilting is

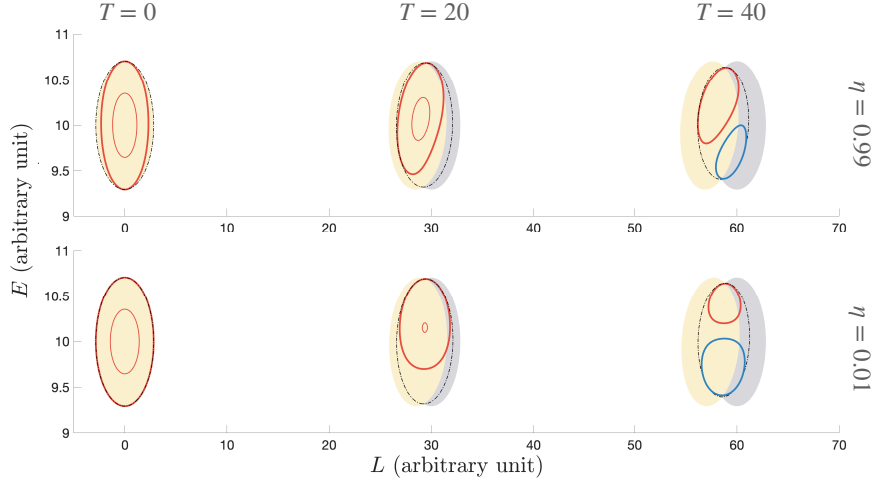


Figure 3.4: Same as Fig. 3.3, but demonstrating the FTP in Eq. (3.40) on the physical layer, also assuming Gaussian distributed weighting functions. The differences between each FTP are labeled on the figure, showing the time evolution of the FTP and the effect of the alignment factor.

negligible, because the mass splitting is a lot smaller compared to the uncertainty of the energy, σ_E . In Sec. ??, from time-independent version of these plots, we will show that Fig. 3.3 and Fig. 3.4 correspond to state decoherence and phase decoherence, respectively.

3.4 Measurement Layer (Layer 3): Transition Probability

In this section, we arrive at the measurement layer, where we consider the collection of experimental data. In addition to the uncertainties that have originated from the previous layers, namely the phase space uncertainties (PSUs), the final data must also account for count uncertainties (CUs). While the PSUs pertain to uncertainties in the phase space variables (such as σ_x , σ_p , σ_L , and σ_E discussed earlier), the CUs relate to uncertainties in the neutrino flux. These include statistical uncertainties and background uncertainties. In our likelihood/ χ^2 analysis in Sec. 4.2, we will treat the PSUs and the CUs differently. Specifically, we will treat the CUs as conventional “uncertainties” in the analysis, while the PSUs will be incorporated into the theoretical prediction. The total count rate for energy-distance binned data is given by:

$$N_{\text{tot}} = \int_{L_0 \text{ bin}} dL_0 \frac{1}{4\pi L_0} \int_{E_0 \text{ bin}} dE_0 \Phi_0(E_0) D(E_0) P_{3,\alpha\beta}(L_0, E_0). \quad (3.41)$$

Here, the CUs are encompassed within $\Phi_0(E_0)$, which represents the neutrino flux at $L_0 = 0$, accounting for production rate. The term $D(E_0)$ encapsulates the detection rate, including the cross section pertinent to the detection process. Conversely, the PSUs are integrated into $P_{3,\alpha\beta}(L_0, E_0)$, which signifies the FTP on the measurement layer. These PSU-related aspects will be discussed in the following paragraph.

Below, we demonstrate impact of PSUs on the FTP after integrating over the time-ignorant FTP on the second layer. In the following, we take Gaussian PDFs for both $H_L(L; L_0)$ and $H_E(E; E_0)$ for demonstration, the integration over L would result as

$$\begin{aligned}
P_{3,jk}^{\text{semi}}(L_0, E) &= \int dL \exp\left[\frac{-(L-L_0)^2}{4\sigma_L}\right] P_{2,jk}(L, E) \\
&= \exp\left[i\frac{\Delta m_{jk}^2 L_{0,jk}^{\text{eff}}}{2E}\right] \exp\left[-\frac{\left(L_{0,jk}^{\text{eff}}\right)^2}{\left(L_{kj}^{\text{coh}}\right)^2} - \left(\frac{\Delta m_{jk}^2 \Delta L}{2E}\right)^2 - \left(\frac{\Delta m_{jk}^2}{2\sqrt{2}E}\right)^2 \left[\left(\frac{1-\eta}{\sigma_{\bar{p}}}\right)^2 + \sigma_{\bar{x}}^2\right]\right] \\
&\simeq \exp\left[i\frac{\Delta m_{jk}^2 L_0}{2E}\right] \exp\left[-\left(\frac{\Delta m_{jk}^2 \sigma_L}{2E}\right)^2 - \left(\frac{L_0}{L_{kj}^{\text{coh}}}\right)^2\right], \quad (\sigma_{\bar{x}}, 1/\sigma_{\bar{p}} \ll \sigma_L \ll L_{jk}^{\text{coh}}, L_0),
\end{aligned} \tag{3.42}$$

and the integration over E will be done numerically. The resulting FTP on the measurement layer, $P_3(L_0, E_0)$ is plotted in Fig. 3.5 and Fig. 3.6. In Eq. (3.42), the total spatial uncertainty, being the width of H_L , would usually be dominated by σ_S , the width of the production profile. This is because $\sigma_L^2 = \sigma_S^2 + \sigma_D^2$ for neutrinos propagating in vacuum, and the the spatial resolution of the detector σ_D would be subdominant. Consequently,

$$\Delta_L^2 = \frac{\sigma_L^2 \left(L_{kj}^{\text{coh}}\right)^2}{4\sigma_L^2 + \left(L_{kj}^{\text{coh}}\right)^2}, \quad L_{0,jk}^{\text{eff}} = \frac{L_0 \left(L_{kj}^{\text{coh}}\right)^2}{4\sigma_L^2 + \left(L_{kj}^{\text{coh}}\right)^2}. \tag{3.43}$$

In the second line of Equation (3.42), the last two terms in the exponent represent locality terms, indicating that a higher degree of local uncertainty (including $\sigma_{\bar{x}}$, $1/\sigma_{\bar{p}}$, and σ_L), whether microscopic or macroscopic, results in more smearing of the FTP. Since $\sigma_{\bar{x}}$ and $1/\sigma_{\bar{p}} \ll \sigma_L$, the macroscopic uncertainty dominates, as seen in the third line. As for the first term in the second exponent, it modifies the coherence length by $L_{kj}^{\text{coh}} \rightarrow \sqrt{\left(L_{kj}^{\text{coh}}\right)^2 + 4\sigma_L^2}$. However, since L_{kj}^{coh} is inversely proportional to the mass splitting of neutrinos, it is usually much larger than σ_L for ground-based experiments. In this case, the microscopic uncertainty would dominate this term. Nevertheless, for neutrinos produced in continuously emitting celestial objects for extended periods, the situation might be different [48]. For instance, the size of the Sun's core could be much larger than the coherence length in the three-neutrino paradigm. However, the coherence length might be stretched out for neutrinos produced in extreme environments, such as supernovae [49, 50], or at ultra-high energies [51], leading to long oscillation lengths. Furthermore, since the integration $\int dE H_E(E; E_0) P_{3,jk}^{\text{semi}}(L_0, E)$ satisfies the factorization condition in Appendix B, we can express it as follows:

$$P_{3,jk}(L_0, E_0) \simeq \exp\left[-\left(\frac{\Delta m_{jk}^2 \sigma_L}{2E_0}\right)^2 - \left(\frac{\Delta m_{jk}^2 \sigma_{\bar{p}} L_0}{2\sqrt{2}E_0^2}\right)^2\right] \int dE \exp\left[i\frac{\Delta m_{jk}^2 L_0}{2E}\right] H_E(E; E_0). \tag{3.44}$$

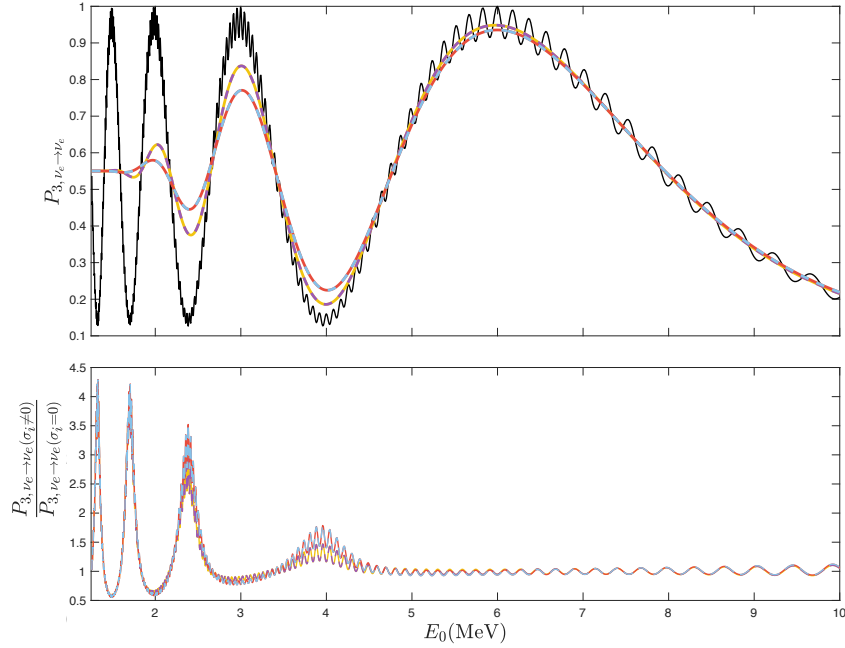


Figure 3.5: Three flavor FTP spectrum from electron neutrino to electron neutrino on the measurement layer at $L_0 = 200$ km (this distance is chosen such that decoherence effects are visible in this energy range for some reasonable uncertainties). The black line represents completely coherent FTP, and the coloured lines all have $\sigma_{\bar{p}} = 0.4$ MeV and $\sigma_{\bar{x}}$ is negligible compared to σ_L . We have $\sigma_L = 0$ m, $\sigma_E = 0$ MeV for the yellow line, $\sigma_L = 5$ m, $\sigma_E = 0$ MeV for the purple line, $\sigma_L = 0$ m, $\sigma_E = 0.1\sqrt{E_0}$ MeV for the red line, and $\sigma_L = 5$ m, $\sigma_E = 0.1\sqrt{E_0}$ MeV for the blue line. Here σ_L is chosen according to a typical reactor core size, σ_E is a typical detector resolution and $\sigma_{\bar{p}}$ is taken at a value such that it is comparable with σ_E .

Hence, the effects of H_L on P_3 hardly depend on L_0 , unless σ_L accumulates as L_0 increases.

Utilizing oscillation parameters extracted from the NuFit 5.1 global fit results [52], we have generated FTP plots for long-distance neutrinos, as presented in both Fig.3.5 and Fig.3.6. These figures reveal key insights: the impact of decoherence, either in terms of damping or phase shifts, is notably more pronounced at lower energies. This phenomenon is attributed to the higher phase-density associated with lower energies, resulting from the reduced oscillation length. Consequently, the Phase Width Overlap (PWO) effect is enhanced. Moreover, in the context of long-distance scenarios, σ_L exhibits minimal impact, as it does not increase with L_0 . Additionally, for Gaussian-distributed weighting functions, only σ_E introduces a phase shift, as it is the only one asymmetric with respect to the phase structure. In contrast, in extremely short baseline situations, as illustrated in the right panel of Fig. 3.6, sensitivity to σ_L surpasses that of $\sigma_{\bar{p}}$ and σ_E , due to the same underlying principle. However, it's crucial to note that this effect is exceptionally small in comparison to long-distance scenarios. Nevertheless, it benefits from larger statistics, scaling by a factor of L_0^2 .

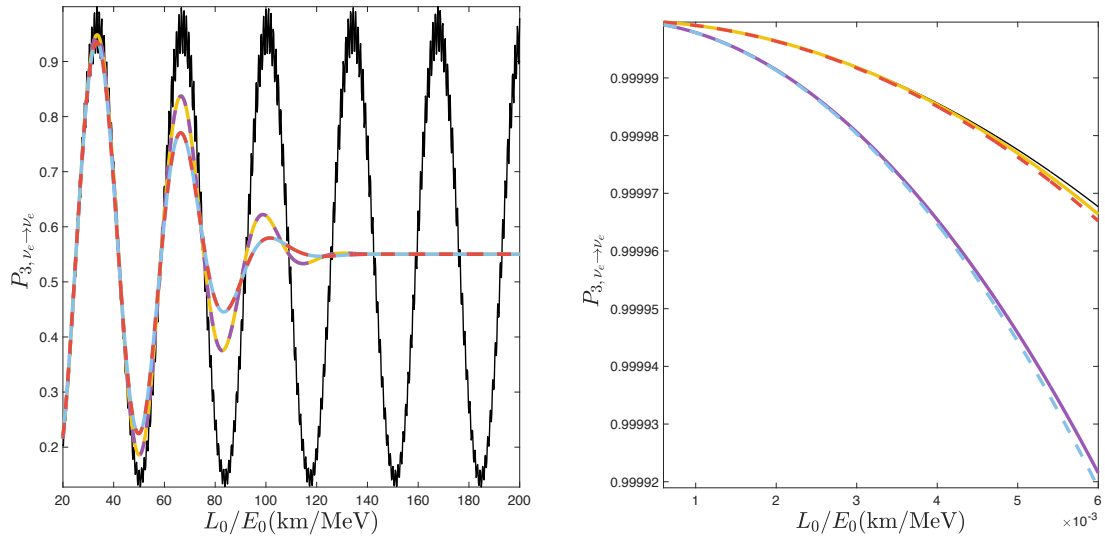


Figure 3.6: FTP from electron neutrino to electron neutrino as a function of L_0/E_0 on the measurement layer for near (right) and far (left) detector. The lines are labels in the same way as Fig. 3.5. We can identify more sensitivity to σ_L at near detectors while effects of $\sigma_{\bar{p}}$ and σ_E are more pronounced at far detectors.

Chapter 4

Neutrino Decoherence Signatures

Contents

4.1	Classification of Decoherence-like Signatures	44
4.2	Spectral Analysis	58
4.3	A Phase Measuring Proposal	63

Overview

With information loss occurring at different levels, quantum mechanical uncertainties provide a parameterization for decoherence via an inherent effect of mass eigenstate separation. On the other hand, decoherence stemming from classical uncertainties is typically dominated by a statistical averaging process. In this chapter, we will illustrate that by leveraging the layer structure, we can categorize the former as state decoherence (SD) and the latter as phase decoherence (PD). Furthermore, we will establish that both SD and PD originate from PWO effects associated with distinct phase structures on different layers. These effects lend themselves to straightforward numerical calculations of decoherence, contingent upon the specific width and shape of uncertainties. Furthermore, the distinction between difference decoherence parameters comes from different dependence on the phase structure(s). Put differently, whereas quantum coherence is reflected in the oscillation signature, decoherence can be characterized as a form of washing-out of such signature. Therefore, the PWO effect arising from neutrino decoherence results in a damping and/or phase shift signature to the oscillation by Ψ_{jk} in Eq. (2.2) for each eigenstate interference.

In terms of the phenomenological aspects of neutrino decoherence, broadly speaking, observations of neutrinos for both long and short baseline experiments, as well as those from the atmosphere, are best described by treating neutrinos as fully coherent. One can refer to [52] for an updated global fit supporting this notion. On the other hand, for neutrinos produced outside

the Earth, a fully incoherent description appears to be more appropriate. There have been extensive discussions regarding various aspects of neutrino decoherence phenomena, including general neutrino decoherence in reactor experiments [7, 53, 54]; gravitational fluctuations or cosmological effects leading to atmospheric neutrino decoherence [6, 16, 55, 56]; and matter effects responsible for accelerator or atmospheric neutrino decoherence [20, 57–60].

Our framework has the capacity to encompass all of these mechanisms and more, given that it incorporates both the QFT approach and the concept of open quantum systems. Consequently, instead of going into the specifics of these theories, we provide a general overview of the measurable parameters they could potentially affect. Furthermore, we also consider decoherence effects arising from classical uncertainties due to the observer’s lack of knowledge, such as uncertainties in the neutrino production profile (e.g., the exact shape of the neutrino source) and the energy reconstruction model. We delve deeper into the analysis of damping and phase shift signatures with respect to both classical and quantum mechanical uncertainty parameters, focusing on reactor/decay-at-rest (DAR) neutrinos. Damping signatures, which are anticipated in the literature mentioned earlier, are evaluated for their sensitivity by directly analyzing the neutrino count rate using conventional methods. However, phase shift signals are found to be less amenable to this approach. Instead, we explore the feasibility of measuring the distance-dependent oscillation phase for phase shift signals.

4.1 Classification of Decoherence-like Signatures

4.1.1 Formalism

In this section, we will illustrate how neutrino decoherence can be further categorized into two distinct types, one resulting from the separation of mass eigenstates leading to coherence loss, and the other arising from statistical averaging effects. Within the framework of the layer structure, we will demonstrate that both types of decoherence effects stem from PWO effects. As a result, we formulate neutrino decoherence effects in terms of a damping term (ϕ_{jk}) and a phase shift term (β_{jk}), expressed as follows:

$$P_{3,jk}(X_3) = e^{i[\psi_{jk}(X_3) - \beta_{jk}(X_3; \vec{\sigma})]} \phi_{jk}(X_3; \vec{\sigma}), \quad (4.1)$$

for

$$P_{3,\alpha\beta}(X_3) = \sum_{j,k} U_{\alpha j}^* U_{\beta j} U_{\alpha k} U_{\beta k}^* P_{3,jk}(X_3), \quad (4.2)$$

where $P_{3,\alpha\beta}(X_3) = \sum_j \sum_k P_{3,jk}(X_3)$. Here, ψ_{jk} represents the phase structure on the second layer, as discussed in Eq. (3.30). The vector $\vec{\sigma} = \vec{\sigma}_x, \vec{\sigma}_p, \vec{\sigma}_L, \vec{\sigma}_E, \vec{\sigma}_T$ encompasses parameters describing the weighting functions, such as the width and asymmetry parameters associated with each variable.

In general, X_3 includes temporal, spatial, energy, spatial solid angle, and momentum solid angle variables for the third layer. For isotropic neutrinos, $X_3 = T_0, L_0, E_0$, and in the case of

neutrinos continuously emitted over a sufficiently long period, $X_3 = L_0, E_0$. For simplicity, this thesis considers only these latter two cases. Specifically, if all the weighting PDFs are Gaussian distributions, then the damping term can be parameterized as:

$$\phi_{jk}(X_3) = e^{-[\Delta m_{jk}^2 \gamma(X_3; \vec{\sigma})]^2}. \quad (4.3)$$

Additionally, it is essential to define the operational FTP, since $P_{3,jk}$ is on the measurement layer. We define the FTP for each $P_{3,jk}(X_3)$ as the ratio between the total count with and without oscillation, as follows:

$$P_{3,jk}(X_3) = \frac{\int dX_2 H(X_2; X_3) \Gamma_{2,jk}(X_2; X_3)}{\sqrt{\int dX_2 H(X_2; X_3) \Gamma_{2,jj}(X_2; X_3)} \sqrt{\int dX_2 H(X_2; X_3) \Gamma_{2,kk}(X_2; X_3)}}, \quad (4.4)$$

where $\Gamma_{2,jk}(X_2; X_3) \propto P_{2,jk}(X_2; X_3)$ represents the un-normalized FTP on the second layer, and X_2 corresponds to the second layer variables analogous to X_3 . It is important to note that, with this definition, $P_{3,jk}(X_3)$ is independent of the scaling of the weighting functions on each layer and is solely determined by their widths and shapes.

One might raise concerns regarding the validity of the definition provided in Eq. (4.4), as it measures the FTP by considering the total $P_{3,\alpha\beta}$ rather than each $P_{3,jk}$ individually. However, from a theoretical perspective, it is indeed possible to measure $P_{3,jk}$ by employing an approach where the denominator is measured with precision to determine the exact neutrino mass. This would be accomplished through a well-controlled oscillation experiment. It's worth noting that in a mass-measuring experiment, oscillation doesn't occur since the neutrino's mass eigenstate is precisely known. Therefore, such an experiment serves the purpose of normalizing an oscillation experiment. In the context of neutrino mixing, where only two mass eigenstates (with eigenvalues m_j and m_k) are involved and sensitive, the numerator in Eq. (4.4) can be obtained through oscillation experiments. Furthermore, due to the smallness of the mass splitting, the shape of the weighting functions on each layer can be approximated as being independent of the indices j and k . Consequently, we can express $\Gamma_{2,jj}(X_2; X_3) = \Gamma_{2,kk}(X_2; X_3) = \Gamma_{\alpha}^{\text{pro}}(X_2; X_3) \sigma_{\beta}^{\text{det}}(X_2; X_3)$. Here, $\Gamma_{\alpha}^{\text{pro}}(X_2; X_3)$ represents the production rate for flavor α , and $\sigma_{\beta}^{\text{det}}(X_2; X_3)$ is the detection cross section for flavor β . In this scenario, the difference between the weighting functions only arises from the distinct group velocities \mathbf{v}_j , which becomes relevant when $j \neq k$. Consequently, the FTP can be expressed as:

$$P_{3,\alpha \rightarrow \beta}(X_3) = \frac{\sum_{j,k} U_{\alpha j}^* U_{\beta j} U_{\alpha k} U_{\beta k}^* \int dX_2 H(X_2; X_3) \Gamma_{2,jk}(X_2; X_3)}{\int dX_2 \Gamma_{\alpha}^{\text{pro}}(X_2) \sigma_{\beta}^{\text{det}}(X_2) H(X_2; X_3)}. \quad (4.5)$$

This expression, along with its conditions for the uncertainties to be independent of j and k , align with the formulation in [28].

Additionally, the definition presented in Eq. (4.4) inherently normalizes as follows:

$$\sum_{\alpha} P_{3,\alpha\beta} = \sum_{\beta} P_{3,\alpha\rightarrow\beta} = 1. \quad (4.6)$$

This normalization is achieved without imposing any further conditions since it implies that $P_{3,jj} = 1$ for any value of j . This condition ensures that:

$$\sum_{\alpha} P_{3,\alpha\rightarrow\beta} = \sum_{j,k} \sum_{\alpha} U_{\alpha j}^* U_{\alpha k} U_{\beta j} U_{\beta k}^* P_{3jk} = \sum_{j,k} \delta_{jk} U_{\beta j} U_{\beta k}^* P_{3,jk} = \sum_j U_{\beta j} U_{\beta j}^* P_{3,jj} = 1, \quad (4.7)$$

and similarly for $\sum_{\beta} P_{3,\alpha\beta} = 1$. This result remains consistent as long as $0 \leq U_{\beta j} U_{\beta j}^* \leq 1$ and $0 \leq P_{3,jj} \leq 1$ for all values of j . In essence, the normalization condition is satisfied if and only if $P_{3,jj} = 1$.

Moreover, Eq. (4.4) can also be employed to analyze the decoherence effect by expressing it as follows:

$$P_{3,jk}(X_3) \equiv S_{3,jk}(X_3) \Phi_{3,jk}(X_3) e^{i\psi_{jk}(X_3)}. \quad (4.8)$$

In this equation, we have introduced two functions:

$$S_{3,jk}(X_3) = \frac{\int dX_2 H |\Gamma_{2,jk}|}{\sqrt{\int dX_2 H \Gamma_{2,jj}} \sqrt{\int dX_2 H \Gamma_{2,kk}}}, \quad (4.9)$$

and

$$\Phi_{3,jk}(X_3) = \frac{\int dX_2 H \Gamma_{2,jk}}{\int dX_2 H |\Gamma_{2,jk}|} e^{-i\psi_{jk}}. \quad (4.10)$$

Here, for simplicity, we have denoted $H \equiv H(X_2; X_3)$, $\Gamma_{2jk} \equiv \Gamma_{2jk}(X_2; X_3)$, and $\theta_{jk} \equiv \theta_{jk}(X_3)$.

Both functions in Eq.(4.9) and Eq.(4.10) serve as the decoherence terms. They are both unitary in the fully coherent case, with their modulus being less than or equal to 1 in general. Specifically, $S_{3,jk}$ represents the probability of overlap between the two mass states. In this context, we refer to it as ‘‘the state decoherence (SD) term’’. When $S_{3,jk}(X_3) = 1$, it signifies that the two mass eigenstates are entirely overlapping, implying that j th and k th eigenstate are fully in coherent. On the other hand, $\Phi_{3,jk}$ gives us insight into the PWO effect introduced in previous sections. Hence, we label this part as ‘‘the phase decoherence (PD) term’’. When $\Phi_{3,jk}(X_3) = 1$, it indicates that there is no PWO effect occurring on the physical layer, where no decoherence signature will be observed from this term.

We can illustrate the separation of the decoherence term into SD and PD in Eq.(4.8) using a visual representation, as demonstrated in Fig.4.1. To achieve this, we insert the identity $1 = \int dX_2 H |\Gamma_{2,jk}| e^{-i\psi_{jk}} / \int dX_2 H |\Gamma_{2,jk}| e^{-i\psi_{jk}}$ into Eq. (4.4). In the figure, the blue and red shaded circles represent two distinct mass eigenstates on the physical layer. The total FTP corresponds to the purple area in the numerator of the phase decoherence term normalized by the purple area in the denominator of the state decoherence term. Consequently, SD denotes the probability of the two mass eigenstates being in a superposition on the relativistic-PS. On

$$P_{3,jk} = \left[\frac{\text{State decoherence term}}{\text{Phase decoherence term}} \right] \times e^{i\psi_{jk}}$$

Figure 4.1: Demonstration of how we separate the FTP defined in Eq. (4.4) into two terms: the state decoherence term and the phase decoherence term in Eq. (4.9) and Eq. (4.10) in terms of probability. The blue and red shaded circles represent two different mass eigenstates on the physical layer, and while the state decoherence term represents the separation of the two mass eigenstates, the phase decoherence term demonstrates a phase wash-out effect.

the other hand, PD reflects our uncertainty about the system on the relativistic-PS, achieved by averaging over all possible scenarios. More specifically, in alignment with Eq. (3.42), the term involving the coherence length describing the WP separation represents SD, while the localization term signifies PD. Therefore, we can anticipate that the SD term will be primarily influenced by the (microscopic) uncertainties on the first layer, while the PD term will be largely affected by the (macroscopic) uncertainties on the second layer.

4.1.2 State Decoherence

In this section, we will demonstrate how the SD term can be subjected to a further analysis and approximation. Ultimately, we will establish that despite SD representing state separation on the physical layer (2nd layer), it can be considered equivalent to a PWO effect on the Wigner-PS (1st layer) in most scenarios. Consequently, the primary sources of uncertainty that dominate SD are those involved in the first layer, namely σ_x and σ_p .

- σ_x (coordinate uncertainty on the Fock-PS \ni layer 1): This uncertainty arises from intrinsic off-shell effects associated with the finite space-time extent of the vertices, which, in turn, depend on the neutrino interaction occurring at the production and detection sites. In fact, when a Fourier transformation of the weighting function g_P/g_D is preformed, it results in an effective form factor that depends on the neutrino momentum. This can be observed by integrating out x_1/x_2 in Eq. (2.30). Consequently, depending on the nature of the interaction, σ_x may represent the charge radius of the proton or neutron, which is typically on the order of 0.1–1 fm, as noted in [61], or even the inter-atomic distance, which can be at a scale of 0.1–1 nm, as discussed in [62]. In Sec. 3.1, we accounted for sources of uncertainty as unrelated spatial and temporal uncertainties (as they are not constrained to the mass-shell) for both the production and detection locations in the computation of the transition amplitude. In Sec. 2.2.2, we have demonstrated that σ_x combines these sources of uncertainty in a convolution-like manner, and thus, it is primarily influenced by the largest source of uncertainty.

- σ_p (momentum uncertainty on the Fock-PS \ni layer 1): This uncertainty originates from the WP description of the external states at a quantum mechanical level, which also becomes apparent when we compute the transition amplitude. To illustrate, σ_p is closely related to the mean free path of interactions that occur before the external particles engage with the neutrinos or the lifetime of the parent particles, as discussed in [32, 42]. Furthermore, as the external particles are on the mass-shell, the energy uncertainties are intrinsically linked to the momentum uncertainties. Unlike σ_x , σ_p combines various sources of uncertainty, encompassing the momentum and energy uncertainties in both production and detection processes, in a product manner. Consequently, the smallest among these uncertainties tends to dominate. However, the total momentum uncertainty at each site results from the convolution of the initial and final state WPs, thus, it is the smaller of the two that typically prevails, as explained in Sec. 2.2.2.

We stress that σ_p and σ_x are independent of each other, and both can be characterized in either coordinate space or momentum space. The distinction between these two types of uncertainties lies in whether they originate from uncertainties associated with the external states or the effective vertices (internal states). Furthermore, as demonstrated in Sec.3.3 and Sec.3.4, it is more convenient to express the width of the quasi-probability distribution in terms of $\sigma_{\bar{x}} = \sigma_x/\Delta$ and $\sigma_{\bar{p}} = \sigma_p/\Delta$, where $\Delta = 1 + 4\sigma_x^2\sigma_p^2$.

- $\sigma_{\bar{x}}$ (coordinate uncertainty on the Wigner-PS \ni layer 1): By Eq. (4.20), the damping term in Eq. (4.3) for a time-independent Gaussian distributed PDF is

$$\gamma_x = \frac{\sigma_{\bar{x}}}{2\sqrt{2}E_0}. \quad (4.11)$$

Nevertheless, as we will demonstrate in the following section, this structure is identical to that of σ_L , which is typically macroscopic, and consequently, it can be disregarded comparably.

- $\sigma_{\bar{p}}$ (momentum uncertainty on the Wigner-PS \ni layer 1): The damping term in Eq. (4.3) would be

$$\gamma_p = \frac{\sigma_{\bar{p}}L_0}{2\sqrt{2}E_0^2}, \quad (4.12)$$

for a time-independent Gaussian distributed PDF, according to Eq. (3.34). Here, the time-dependent component can be accounted for by substituting L_0 with T_0 . Consequently, the decoherence effect arising from $\sigma_{\bar{p}}$ should be sought for at longer distances. Such effects have been extensively researched and examined, particularly for reactor neutrinos, as seen in [53, 54]. These studies exclude values of $(2\sigma_{\bar{p}})^{-1}$ below 2.08×10^{-4} nm at a 90% confidence level. In fact, $(2\sigma_{\bar{p}})^{-1}$ characterizes the total spatial uncertainty, encompassing both the production and detection regions. Hence, in the ensuing discussion, we occasionally consider $\sigma_{\bar{p}}$ to be approximately 0.1 MeV as a "reasonable" value. This value corresponds to $(2\sigma_{\bar{p}})^{-1} \sim 10^{-3}$ nm, which falls within the range of the proton/neutron charge radius

and the inter-atomic distance (typically around 0.1–1 nm), as estimated in [62] for reactor neutrinos.

To derive the State Decoherence (SD), we can begin by expressing the SD term using Eq. (4.9) as

$$S_{3,jk}(X_3) = \frac{\int dX_2 H |\Gamma_{2,jk}|}{\sqrt{\int dX_2 H \Gamma_{2,jj}} \sqrt{\int dX_2 H \Gamma_{2,jj}}} = \frac{\int dX_2 H S_{2,jk} \Phi_{2,jk}}{\sqrt{\int dX_2 H \Phi_{2,jj}} \sqrt{\int dX_2 H \Phi_{2,jj}}}, \quad (4.13)$$

where we replace $\Gamma_{2,jk}$ with

$$\Gamma_{2,jk} = |\Gamma_{2,jk}| e^{i\psi_{jk}} = S_{2,jk} \Phi_{2,jk} e^{i\psi_{jk}} \text{ and } \Phi_{2,jk}(X_2) = \int d^3\bar{x} \int d^3\bar{p} |\Gamma_{1,jk}(\bar{x}, \bar{p}; X_2)|. \quad (4.14)$$

Here, $S_{2,jk} = S_{2,jk}(X_2)$, $\Phi_{2,jk} = \Phi_{2,jk}(X_2)$, and $\psi_{jk} = \psi_{jk}(X_2)$. Additionally, according to Eq. (3.29), $\psi_{jj}(X_2) = 0$ for any j , and $\Gamma_{1,jk}(\bar{x}, \bar{p}; X_2) \propto P_{1,jk}(\bar{x}, \bar{p}; X_2)$ represents the un-normalized transition probability distribution on the Wigner-PS, such that $\Gamma_{2,jk}(X_2) = \int d^3\bar{x} \int d^3\bar{p} \Gamma_{1,jk}(\bar{x}, \bar{p}; X_2)$. Thus, the remaining term becomes:

$$S_{2,jk}(X_2) = e^{-i\psi_{jk}} \frac{\int d^3\bar{x} \int d^3\bar{p} \Gamma_{1,jk}(\bar{x}, \bar{p}; X_2)}{\int d^3\bar{x} \int d^3\bar{p} |\Gamma_{1,jk}(\bar{x}, \bar{p}; X_2)|} \equiv e^{-i\psi_{jk}} \frac{\int d^3\bar{x} \int d^3\bar{p} \bar{D}_{jk}(\bar{x}, \bar{p}; X_2) e^{i\bar{\eta}_{jk}(X_2)}}{\int d^3\bar{x} \int d^3\bar{p} \bar{D}_{jk}(\bar{x}, \bar{p}; X_2)}, \quad (4.15)$$

This shows that $S_{2,jj}(X_2) = 1$, since $\psi_{jj} = \eta_{jj} = 0$ for all j . Therefore, we only need to consider the terms dependent on \bar{x} and \bar{p} for \bar{D}_{jk} . In fact, Eq.(4.15) has the same form of a PWO effect (Eq.(A.3)) with the phase structure $\bar{\eta}_{jk}$ averaged within the normalized \bar{D}_{jk} region.

For example, if we consider Gaussian distributed weighting functions as in Eq. (3.19), then

$$\bar{D}_{jk}(\bar{x}, \bar{p}; T, \mathbf{L}, E) = \exp \left[-\frac{(\bar{x} - \bar{\mathbf{L}}_{jk}/\Delta)^2}{2\sigma_{\bar{x}}^2} \right] \exp \left[-\frac{(\bar{p} - \bar{\mathbf{P}}_{jk})^2}{2\sigma_{\bar{p}}^2} \right]. \quad (4.16)$$

The phase structure is generally given by:

$$\bar{\eta}_{jk}(\bar{x}, \bar{p}; T, E) = -iT\bar{p}(\mathbf{v}_j - \mathbf{v}_k) + i\Delta\bar{x}(\mathbf{P}_j - \mathbf{P}_k), \quad (4.17)$$

where the relation between T, \mathbf{L}, E and $\bar{\mathbf{L}}_{jk}, \bar{\mathbf{P}}_{jk}, \mathbf{P}_j, \mathbf{P}_k$ is provided in Sec. ??.

In the following discussion, we will assume isotropic distributions and simplify the scenario to one dimension. From Appendix B, we observe that the first approximation in Eq. (4.18) can be made in the limit of $X_3 \gg \Delta_{X_2}$ and $\sigma_S \gg \Delta_{X_2}$. Here, we have taken σ_S and Δ_{X_2} as the width of $S_{2,jk}(X_2)$ and $Y_{2,jk}(X_2; X_3) \equiv H(X_2; X_3)\Phi_{2,jk}(X_2)$, respectively, when applying Appendix B. This factorization condition implies neglecting the uncertainty of X_3 on the second layer for the term that can be taken out of the integral, i.e., $X_2 \simeq X_3$, in $S_{2,jk}$ for some Δ_{X_2} . At the same time, σ_S cannot be neglected to maintain SD. Furthermore, if the total uncertainty Δ_{X_2} is predominantly due to the physical layer uncertainty H , as is the case for macroscopic measurements, then $Y_{2,jk}(X_2) \simeq Y_{2,jj}(X_2) \simeq Y_{2,kk}(X_2)$, leading us to the second approximation

in the following equation:

$$S_{3,jk}(X_3) \simeq S_{2,jk}(X_2) \Big|_{X_2=X_3} \frac{\int dX_2 Y_{2,jk}}{\sqrt{\int dX_2 Y_{2,jj}} \sqrt{\int dX_2 Y_{2,kk}}} \simeq S_{2,jk}(X_2) \Big|_{X_2=X_3}. \quad (4.18)$$

The comparison between the width sizes of $S_{2,jk}$, $\Phi_{2,jk}$, and H can be assessed by assuming Gaussian distributions for the weighting functions on each layer. Specifically, for both $S_{2,jk}$ (with width σ_{S,X_2}) and $\Phi_{2,jk}$ (with width σ_{Φ,X_2}), we can use Eq. (3.12). As for $H(X_2)$ (with width σ_{H,X_2}), we can simply represent it as a Gaussian distribution around X_3 . In this scenario, we have the following expressions for Φ_{jk} and S_{jk} :

$$\Phi_{2,jk}(L, E, T) = \exp \left[-\frac{(L_j + L_k)^2 \sigma_{\bar{p}}^2}{2} - \frac{(P_j + P_k)^2 \sigma_{\bar{x}}^2}{2} \right], \quad (4.19)$$

and

$$S_{2,jk}(L, E, T) = \exp \left[-\frac{(L_j - L_k)^2 \sigma_{\bar{p}}^2}{2} - \frac{(P_j - P_k)^2 \sigma_{\bar{x}}^2}{2} \right]. \quad (4.20)$$

Therefore, the width of Φ_{jk} with respect to L and T is given by $\sigma_{\Phi,L} = (2\sigma_{\bar{p}})^{-1}$ and $\sigma_{Phi,T} = [\sigma_{\bar{p}}(v_j + v_k)]^{-1} \simeq E^2[\sigma_p(m_j^2 + m_k^2)]^{-1}$, respectively. For S_{jk} , the width with respect to L and T is $\sigma_{S,T} = [\sigma_{\bar{p}}(v_j - v_k)]^{-1} \simeq E^2[\sigma_p(m_j^2 - m_k^2)]^{-1}$, while $\sigma_{S,L} \rightarrow \infty$ for the time-dependent case, as $S_{2,jk}$ does not depend on L .

In terms of energy uncertainties, we have:

$$\sigma_{\Phi,E} = \int dE \exp \left[-\frac{1}{2} \left(2L - T \frac{m_j^2 + m_k^2}{2E^2} \right)^2 \sigma_{\bar{p}}^2 - \frac{1}{2} \left(2E + \frac{m_j^2 + m_k^2}{2E} \right)^2 \sigma_{\bar{x}}^2 \right] \quad (4.21)$$

and

$$\sigma_{S,E} = \int dE \exp \left[-\frac{1}{2} \left(T \frac{m_j^2 - m_k^2}{2E^2} \right)^2 \sigma_{\bar{p}}^2 - \frac{1}{2} \left(\frac{m_j^2 - m_k^2}{2E} \right)^2 \sigma_{\bar{x}}^2 \right]. \quad (4.22)$$

Due to the $1/E$ dependence, the exponent in Eq. (4.22) approaches 1 as E approaches infinity, resulting in a divergence of $\sigma_{S,E}$. Consequently, the width $\sigma_{\Phi,E}$ also becomes very large in such cases. Therefore, $\sigma_{H,L} \ll \sigma_{Phi,L}, \sigma_{S,L}$ and $\sigma_{H,E} \ll \sigma_{Phi,E}, \sigma_{S,E}$. This indicates that the macroscopic uncertainty $\sigma_{H,L}, \sigma_{H,E}$ will dominate over the transferred microscopic ones of $\Phi_{2,jk}$ for $Y_{2,jk}(X_2; X_3)$ in Eq. (4.18). As a result, we can approximate $\Delta_L \simeq \sigma_{H,L}$ and $\Delta_E \simeq \sigma_{H,E}$. In summary, the factorization condition for Eq. (4.18) is satisfied for the L and E components if the measured values L_0 and E_0 are much larger than $\sigma_{H,L}$ and $\sigma_{H,E}$. This condition is typically met in neutrino experiments with the resolution required to measure neutrino oscillations.

Regarding the temporal aspect, we will explore two scenarios: one where $\sigma_{H,T}$ is much smaller than $\sigma_{\Phi,T}$ and $\sigma_{S,T}$, and another where $\sigma_{H,T}$ approaches infinity. If neither of these situations applies, it's necessary to perform an integration over the variable T while considering the influence of H_T . In the former case, where $\sigma_{H,T}$ is significantly smaller than $\sigma_{\Phi,T}$ and $\sigma_{S,T}$,

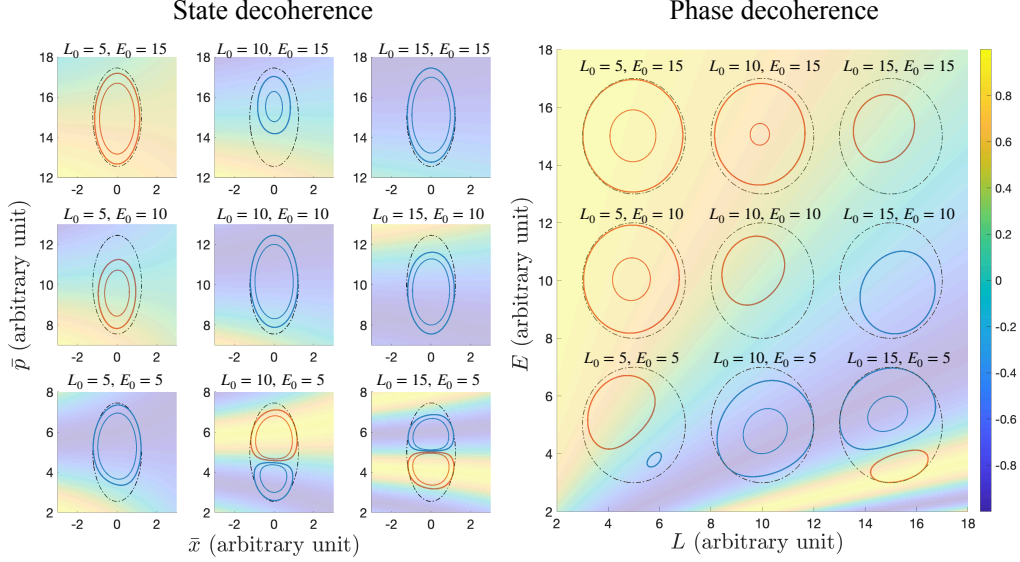


Figure 4.2: Demonstration of time-independent state decoherence (left plot) and phase decoherence (right plot) plotted in a similar fashion as Fig. 3.3 and Fig. 3.4, both representing phase wash-out effects. The former is in the Wigner phase space on layer 1, while the latter is in the relativistic phase space on layer 2. The coloured contour plot in the background is the oscillating phase structure plotted as $\cos(\eta_{jk})$ (left plot) and $\cos(\psi_{jk})$ (right plot), on the corresponding layer. The outer red (blue) circles are the level for two standard deviations of positive (negative) values of the time-independent $P_{1,jk}(X_1; X_3)$ (left plot) and $P_{2,jk}(X_2; X_3)$ (right plot) for weighting functions Eq. (4.24) and Gaussian distributed H_L/H_E , respectively. The inner circle (if there is one), is the contour for one standard deviation. Also, the black dashed line is the contour for two standard deviations of the weighting functions.

the condition for factorization with respect to the variable T is met. Here, $H(X_2)$ dominates over $\Phi_{2,jk}(X_2)$ for all $X_2 = L, E, T$, resulting in $S_{3,jk}(X_3) \approx S_{2,jk}(X_3)$. Consequently, we can directly obtain the time-dependent SD weighting function $D'jk(\bar{x}, \bar{p}; T_0, L_0, E_0)$ and phase structure $\eta'jk$ by substituting X_2 with X_3 . In particular, if all quantum uncertainties follow Gaussian distributions, then $D'jk$ corresponds to $\bar{D}jk(\bar{x}, \bar{p}; T_0, L_0, E_0)$, and $\eta'jk$ aligns with $\bar{\eta}jk(\bar{p}, \bar{x}; T_0, E_0)$. To illustrate this time-dependent PWO effect, we have provided a visual representation in Fig.3.3. This effect intensifies as the wave packets of two states separate over time. Importantly, this phenomenon can be translated into WP separation on the physical layer, as described in Eq.(4.13) and visualized in Fig. 4.1.

On the other hand, if we have no temporal information during the detection process, meaning $\sigma_{H,T} \rightarrow \infty$, then $X_2 = T$ should be integrated out in Eq. (4.13) before looking at the SD term. In this case, after the approximation given in Eqs. (3.24)-(3.27) and including terms up to $\mathcal{O}(m^2)$, the Gaussian example in Eq. (3.12), leads to

$$\eta_{jk}(\bar{x}, \bar{p}; L, E)|_{L=L_0, E=E_0} = i \frac{\Delta m_{jk}^2}{2E_0} \left[(\Delta \bar{x} - L_0) \frac{\bar{p}}{E_0} - \Delta \eta \bar{x} \right]. \quad (4.23)$$

As illustrated in the left plot of Fig. 4.2. Furthermore, the time-independent SD weighting function is

$$D_{jk}(\bar{x}, \bar{p}; E_0) \simeq \exp \left[-2\bar{x}^2 \sigma_{\bar{p}}^2 - \frac{(\bar{p} - E_0 + (m_j^2 + m_k^2)/2E_0)^2}{2\sigma_{\bar{p}}^2} - \left(\frac{\Delta m_{jk}^2 \sqrt{\Delta} \sigma_{\bar{x}}}{2\sqrt{2}E^2} \right)^2 \bar{p}^2 \right]. \quad (4.24)$$

In the left panel of Fig. 4.2, we illustrate the PWO effect based on the aforementioned phase structure and weighting functions. In this visualization, we set $\eta = 1$, $\sigma_{\bar{x}} = 0$, and amplify Δm_{jk}^2 to be one order smaller than E_0 for clarity. However, when $\Delta m_{jk}^2 \ll E_0$, the integration over \bar{x} has a negligible contribution to $S_{3,jk}$. Consequently, the SD term can be approximated as follows:

$$S_{3,jk}(L_0, E_0) \simeq \exp \left(i \frac{\Delta m_{jk}^2 L_0}{2E_0} \right) \frac{\int d\bar{p} D_{jk, \sigma_{\bar{p}}}(\bar{p}; E_0) \exp \left(-i \frac{\Delta m_{jk}^2 L_0}{2E_0^2} \bar{p} \right)}{\int d\bar{p} D_{jk, \sigma_{\bar{p}}}(\bar{p}; E_0)}. \quad (4.25)$$

Here, $D_{jk, \sigma_{\bar{p}}}$ represents a product of three Gaussian distributions. Furthermore, for $E_0 \gg \frac{m_j^2}{E_0}$, the dominant contribution comes from the distribution with a width of $\frac{\sigma_{\bar{p}}}{2}$ centered at E_0 . The phase structure becomes approximately $\eta_{jk} \simeq -\frac{\Delta m_{jk}^2 \bar{p}, L_0}{2E_0^2}$. This behavior is evident from the upper row in the left panel of Fig. 4.2, where phase averaging primarily results from the integration over \bar{p} . Consequently, SD is mainly determined by the Wigner distribution with respect to \bar{p} , and we can refer to this as $D_{\bar{p}}$ -induced decoherence. It's worth noting that the resulting SD term, $S_{3,jk}$, arising from this type of PWO effect not only aligns with the standard decoherence formula in Eq. (3.35) but also underscores that the dependence on L_0 and E_0 is a consequence of the phase structure.

Furthermore, although we have illustrated the case where all weighting functions follow Gaussian distributions, it's important to note that the phase structure remains applicable to arbitrary distributions, provided the saddle point approximation is employed in Eq. 3.18. Hence, since the phase structure essentially implies a Fourier transformation from \bar{p} to $\alpha_{jk} = \frac{\Delta m_{jk}^2 L_0}{2E_0^2}$, we have depicted the damping term and phase shift term resulting from SD for various typical distributions in Fig. 4.3. In particular, the single Gaussian case represents a standard statistical distribution for a single process. The two-Gaussian case takes into account neutrinos that are simultaneously produced by two distinct processes, each with slightly different expectation values for momentum. The other two distributions are better suited for describing an H_L -induced PD effect, which we will delve into in the subsequent subsection. A more comprehensive discussion of this plot will be provided alongside the H_E -induced PD effect. Nevertheless, since both decoherence effects can be characterized by Fourier transformations, albeit with different spatial mappings, we present both effects within the same plot. This demonstrates that distinct sources of decoherence can be discerned based on their dependencies on (L_0, E_0) , which stem from differences in their underlying phase structures.

In summary, while SD characterizes the separation of two mass eigenstates on the physical layer, quantified by the overlapping area between them (as illustrated in Fig. 4.1), the situation

changes when we shift our focus to the Wigner-PS. As depicted in Fig.3.3, we observe that the width of $P_{\bar{1},jk}$ does not decrease as the two mass eigenstates, $P_{\bar{1},jj}$ and $P_{\bar{1},kk}$, move apart. However, the phase density increases as these two mass eigenstates separate, resulting in a stronger PWO effect. This ultimately yields the same outcome as calculating the extent of overlap between two mass eigenstates on the physical layer. Furthermore, from the colored background in Fig.4.2, it's evident that the phase structure varies with the PS variables on the third layer, namely T_0 , L_0 , and E_0 . However, the width of the overlapping weighting function remains constant. In the case of the left plot, which represents the time-independent scenario with $\sigma_{H,T} \rightarrow \infty$, it is clear that there is no dependence on T_0 . Conversely, in the time-dependent scenario shown in Fig.3.3, it emerges that there is no dependence on L_0 . This happens because in $L_j - L_k$, the common factor L cancels out, as shown in Eq. (3.19) or directly from Eq. (4.20).

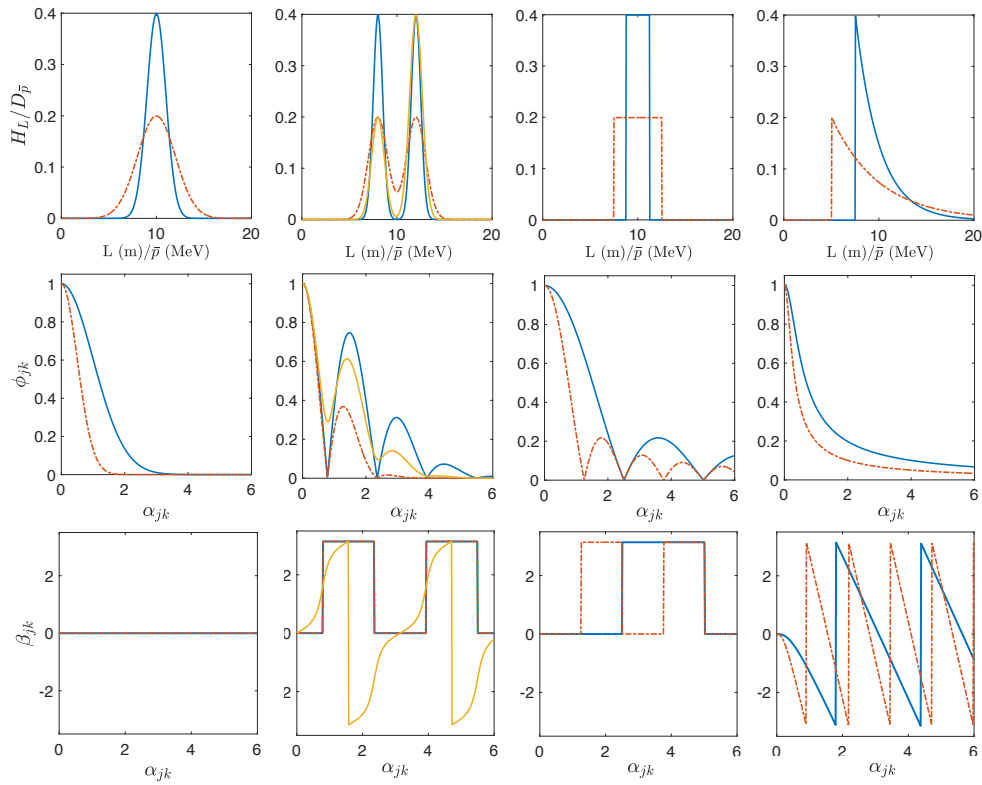


Figure 4.3: Decoherence damping terms (second row) and phase shift terms (third row) for different shaped weighting functions (first row) of H_L -induced or $D_{\bar{p}}$ -induced decoherence. While both types of decoherence are described by Fourier transformation, the former transfers from L space to the $\alpha_{jk} = \Delta m_{jk}^2/(2E_0)$ corresponding to Eq. (4.30); and the later from \bar{p} to $\alpha_{jk} = \Delta m_{jk}^2 L_0/(2E_0^2)$ relates to Eq. (4.25). In particular, the same coloured lines represent weighting functions with the same widths.

4.1.3 Phase Decoherence

In this section, we will demonstrate that the primary factors governing the influence of PD are the macroscopic uncertainties, which are outlined as follows:

- σ_L (coordinate uncertainty on the relativistic-PS \ni layer 2): This uncertainty primarily arises from the macroscopic spatial uncertainties of the entire process, with its dominant contribution coming from the production profile of the neutrino source, especially in cases of vacuum propagation. Unlike σ_x , σ_L does not factor into the Feynman diagram (Fig. 2.2) for calculating the transition amplitude. Instead, it reflects the uncertainty associated with the transition probability on the second layer. For example, σ_L could be determined by factors such as the size of the reactor core (around 3-5 meters) for reactor neutrinos or the distance traveled by mesons/muons before they decay into neutrinos in accelerator experiments. In the case of Gaussian-distributed PDFs, the damping term in Eq. (4.3) can be well-approximated as

$$\gamma_L \propto \sigma_L E_0^{-1}, \quad (4.26)$$

especially when the mass splitting is small, as observed when integrating out the energy variable E in Eq. (3.42). In other words, this damping term is nearly independent of the traveling distance. Therefore, it is advantageous to search for such effects close to the neutrino source to achieve higher statistics. In Fig. 4.3, we illustrate the effects of PD for various production profiles:

- The one Gaussian PDF is suitable for neutrinos produced at rest, such as reactor neutrinos and DAR neutrinos.
- The two Gaussian PDFs are shown for scenarios with multiple sources and/or detectors.
- The box PDF is appropriate when experimental constraints, like the geometry of accelerator or reactor components, dictate a simplified box-shaped production profile.
- The exponential decaying PDF is suitable for neutrinos produced by decaying particles in flight, such as accelerator neutrinos and atmospheric neutrinos.

However, if the propagation process itself contributes to σ_L , then σ_L will accumulate over distance. This can occur due to matter effects [60] or some exotic effects [16, 21, 22, 51], as mentioned in the literature. In such cases, σ_L^2 can be proportional to L_0 , in agreement with the dependence on the traveling distance in the damping term calculated by the Lindblad equation, which is often used in the studies mentioned above.

- σ_E (energy uncertainty on the relativistic-PS \ni layer 2): This uncertainty is primarily determined by the energy resolution of the experimental apparatus and the reconstruction model employed in the experiment. Typically, in the case of neutrinos detected using photomultiplier tubes, the energy resolution is characterized by $\sigma_E = \sigma_E^0 \sqrt{E_0}$, where σ_E^0 typically falls within the range of approximately $\mathcal{O}(0.1)\sqrt{\text{MeV}}$. Furthermore, different

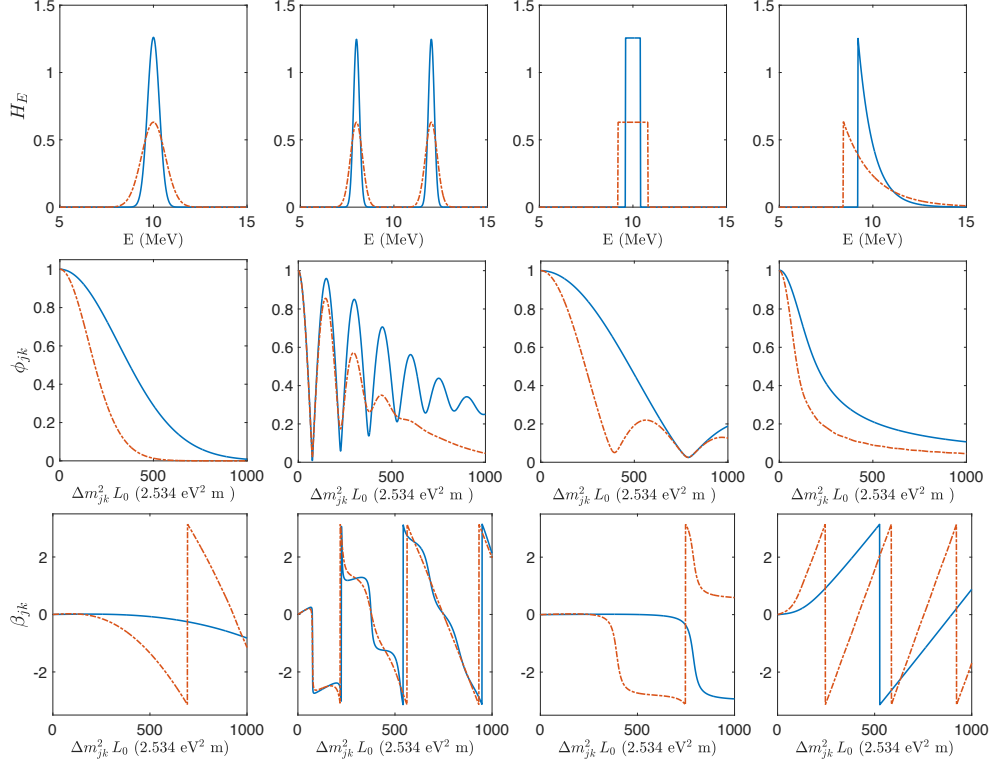


Figure 4.4: Phase decoherence by the macroscopic energy uncertainty σ_E on the physical layer as a phase wash-out effect. Including a damping term and a phase shift term in Eq. (4.1) for different shapes of H_E with the same widths ($\sigma_E/\sqrt{E_0} = 0.1\sqrt{\text{MeV}}$ for the blue line, $\sigma_E/\sqrt{E_0} = 0.2\sqrt{\text{MeV}}$ for the red line), at energy $E_0 = 10$ MeV.

sources contribute to the uncertainty related to the energy reconstruction model. For instance, factors like the degree of quasi-elastic scattering, as discussed in [44] and [45], can lead to a tail in the energy distribution H_E . Additionally, the $1/E$ dependence in ψ_{jk} causes the energy resolution σ_E to be asymmetric with respect to the phase structure, resulting in a phase shift even for a Gaussian-distributed PDF. Numerical simulations, as depicted in Fig. 4.4, illustrate this effect. These numerical results allow us to see how σ_E behaves concerning E_0 and L_0 . For example, Fig. 3.5 demonstrates that the impact of σ_E increases with L_0 in a manner comparable to the behavior of $\sigma_{\bar{p}}$.

Similarly to SD, PD also characterizes a PWO effect, which becomes evident from its definition:

$$\Phi_{3,jk}(X_3) = e^{-i\psi_{jk}(X_3)} \int dX_2 Y'_{2,jk}(X_2; X_3) e^{\psi_{jk}(X_2)}. \quad (4.27)$$

In this equation,

$$Y'_{2,jk}(X_2; X_3) = \frac{S_{2,jk}(X_2)\Phi_{2,jk}(X_2)H(X_2; X_3)}{\int dX_2 S_{2,jk}(X_2)\Phi_{2,jk}(X_2)H(X_2; X_3)} \quad (4.28)$$

represents a real and normalized PDF, with the primary influence coming from the macroscopic weighting function H_{X_2} for $X_2 = L, E$ on the second layer. In cases where $\sigma_{H,T} \ll \sigma_{S,T}, \sigma_{\Phi,T}$, $Y'_{2,jk}$ is predominantly shaped by the macroscopic weighting functions. In this scenario, the phase structure is described by:

$$\psi'_{jk}(T, \mathbf{L}, E) = -i(E_j - E_k)T + i(\mathbf{P}_j - \mathbf{P}_k)\mathbf{L}. \quad (4.29)$$

Conversely, if temporal information is unavailable, one should integrate over the time variable T before examining the decoherence effect. For the time-dependent scenario, the phase structure up to $\mathcal{O}(m^2)$ is given by Eq.(3.30), while for the time-independent case, it is represented by Eq.(3.33).

When the factorization condition is satisfied for integrating out L , Eq. (4.27) becomes:

$$\Phi_{3,jk}(L_0, E_0) \simeq e^{-i2\Delta m_{jk}^2 \frac{L_0}{E_0}} \int dL H_L(L; L_0) e^{i\Delta m_{jk}^2 \frac{L}{E_0}} \int dE H_E(E; E_0) e^{i\Delta m_{jk}^2 \frac{L_0}{E}}. \quad (4.30)$$

This factorization is valid for the time-independent case, where both $H_L(L; L_0)$ and $H_E(E; E_0)$ are normalized PDFs. Consequently, we can consider the (macroscopic) coordinate and energy uncertainties on the second layer as distinct PWO effects. We refer to the former as H_L -induced PD and the latter as H_E -induced PD. In Fig. 4.3 and Fig. 4.4, we illustrate these two PWO effects, respectively, using weighting functions H_L and H_E modeled as PDFs with the same width for the same-colored lines. In other words, $\int dX_2 H_{X_2} = 1$ and $\max H_{X_2}(X_2) = 1/(\sigma_{X_2} \sqrt{2\pi})$, following our definition of “width” in Appendix A. The sole parameter for the two figures depicting the PWO effect on the second layer is the width σ_{X_2} , for a given L_0 or E_0 . For instance, we use $\sigma_L = 1$ m for the blue and yellow lines, and $\sigma_L = 2$ m for the red line in Fig. 4.3, at a distance $L_0 = 10$ m. For Fig. 4.4, we employ $\sigma_E/\sqrt{E_0} = 0.1\sqrt{\text{MeV}}$ for the blue line, and $\sigma_E/\sqrt{E_0} = 0.2\sqrt{\text{MeV}}$ for the red line, at an energy $E_0 = 10$ MeV.

In particular, much like the $D_{\bar{p}}$ -induced SD, H_L -induced PD takes the form of a Fourier transformation from L to $\alpha_{jk} = \Delta m_{jk}^2/(2E_0)$, as shown in Fig. 4.3. For example, a Gaussian PDF transforms into a Gaussian distribution in the $\Delta m_{jk}^2/E_0$ space; the box PDF transforms into a sinc function; and the PDF representing exponential decay (for neutrinos produced by decaying charged leptons) is transformed into a Lorentzian function. Regarding the phase shift term, Appendix B reveals that only the asymmetric functions (the yellow-lined two Gaussian PDF and the exponential decaying PDF) have a non-zero and non- π phase shift. For symmetric ones, although there is no phase shift for a single Gaussian PDF, the phase ranges shift from 0 to π (still with no imaginary part) for the box PDF and the symmetric two-Gaussian PDF due to negative values of the function resulting from the Fourier transformation. However, due to the smallness of the neutrino mass splitting, α_{jk} is typically small for both $D_{\bar{p}}$ -induced and H_L -induced decoherence effects. Consequently, the range of interest lies within a small range around $\alpha_{jk} \rightarrow 0$, where the phase is zero for asymmetric cases. On the other hand, irrespective of how “symmetric” the weighting PDF spectrum may appear, it is not symmetric with respect to $1/E$. As a result, there will always be a non-trivial H_E -induced phase shift, even for a

Gaussian-distributed PDF. Furthermore, it is evident that the larger the width of the PDF, the more significant the decoherence effect becomes, both in terms of the damping term and the phase shift term. Ultimately, if we observe any phase structure dependence in the damping term and/or the phase shift term, such as those in Fig.4.3 and Fig.4.4, we should be able to reconstruct the production profile and cross-verify the energy reconstruction model.

Comparing PD with SD, both phenomena originate from the PWO effect, but they exhibit distinct phase structures denoted as:

case	phase structure	PDF
time-dependent SD	η'_{jk}	D'_{jk}
time-dependent PD	ψ'_{jk}	H_T, H_L, H_E
time-independent SD	η_{jk}	$D_{jk} \simeq D_{\bar{p}}$
time-independent PD	ψ_{jk}	H_L, H_E

In particular, for SD, both the phase structure and the PDF vary with L_0 and E_0 , while in the case of PD, only the mean of the PDF does. This structural difference is shown in the right panel of Fig. 4.2, where the phase structure in the background solely depends on the second layer PS variables, L and E , without any dependence on the third-layer PS variables, L_0 and E_0 . This implies that the second and third layers share the same coherent phase structure, but not with the first layer. The third-layer phase space only determines the centering of the weighting functions, and when it occurs in a region of higher phase density (at lower energy or greater distance), the PWO effect becomes stronger. To illustrate the PWO effect for the time-independent case, Fig. 4.2 is presented in a manner similar to Fig. 3.3 and Fig. 3.4. Additionally, it showcases the phase structures on the Wigner-PS and the relativistic-PS, respectively, in the colored background. The final observable effects on the measurement layer due to SD, H_L -induced PD, and H_E -induced PD are further depicted in Fig. 4.3 and Fig. 4.4.

The advantage of framing the SD and PD effects in terms of the PWO effect lies in the ability to numerically estimate decoherence using only the weighting functions as input. The steps for numerically estimating SD/PD effects are straightforward:

1. Determine the weighting functions on the Wigner-PS and the relativistic-PS.
2. Multiply these functions by the corresponding phase structures.
3. Integrate out the respective phase space variables.

These integration steps are guaranteed to converge because the weighting functions are localized and concentrated around the next level of phase space variables. Even for the simplest phase structure, such as the time-independent case on layer 2, the PD terms can be evaluated numerically, as demonstrated in Fig. 4.4. In principle, by analyzing the waveform and spectrum of neutrino oscillations, it should be possible to reconstruct the weighting functions once their corresponding phase structure is identified.

4.2 Spectral Analysis

From the previous section, we have established that neutrino decoherence effects fall into two categories: SD and PD, both arising as a consequence of a PWO effect. Consequently, both of these effects yield damping terms and phase shift terms, with the latter being significant only when the weighting function lacks symmetry with respect to the phase structure. To be specific, SD is primarily determined by the (microscopic) uncertainties of the first layer, characterized by σ_x and σ_p , whereas PD is controlled by the (macroscopic) uncertainties of the second layer, encompassing σ_T , σ_L , and σ_E . However, only $\sigma_{\bar{p}}$ from the first layer uncertainties is observable, given that $\sigma_{\bar{x}}$ is much smaller than σ_L . Furthermore, in this section, we exclusively consider the time-independent scenario since contemporary experiments, as shown in Fig. 4.5, continuously emit neutrinos over a sufficiently extended duration, thereby making σ_T tend towards infinity. In addition, as we parameterize the uncertainties of the first layer as $\sigma_{\bar{x}}$ and $\sigma_{\bar{p}}$, only $\sigma_{\bar{p}}$ remains as a valid observational parameter, because $\sigma_{\bar{x}}$ is absorbed by σ_L . In this section, we aim to estimate our experimental proximity to achieving a 90% confidence level sensitivity for the detecting damping signatures, as outlined in Eq. (4.1), stemming from the $D_{\bar{p}}$ -induced SD, H_L -induced PD, and H_E -induced PD. Such analysis would not be sensitive to the phase-shift signature, as we will show in the next section.

Concerning the damping signatures, we assume that all weighting functions follow single Gaussian distributions. Consequently, the damping term can be parameterized by $\sigma_{\bar{p}}$, σ_L , and σ_E as expressed in the equation below:

$$\phi_{jk} = \exp \left[- \left(\frac{\Delta m_{jk}^2 \sigma_{\bar{p}} L_0}{2\sqrt{2}E_0^2} \right)^2 - \left(\frac{\Delta m_{jk}^2 \sigma_L}{2E_0} \right)^2 - (\Delta m_{jk}^2 \gamma_E(L_0, E_0; \sigma_E))^2 \right], \quad (4.31)$$

The first two terms are derived from Eq.(4.12) and Eq.(4.26), while the last term can only be determined numerically, as demonstrated in Fig. 4.4. Furthermore, we assess the sensitivity to the three uncertainty parameters through a χ^2 -analysis employing the traditional rate measuring method (RMM). This analysis aims to detect unexpected disappearance or appearance signals resulting from SD and/or PD. Moreover, since neutrino decoherence is more pronounced at low energy, as indicated in Fig. 4.5, we observe that current experiments involving reactor neutrinos possess a higher sensitivity. Therefore, in the following, as a benchmark experiment to evaluate our progress in detecting neutrino decoherence via the damping term, we select the RENO experiment. This choice is based on the experiment's lower level of uncertainty compared to the Double Chooz experiment and its simpler configuration of reactors and detectors in comparison to the Daya Bay experiment. The latter complexity would introduce non-trivial effects on the damping signature through σ_L , as discussed in more detail in Appendix ???. Additionally, we discuss the different dependencies on L_0 and E_0 in the damping signatures within neutrino oscillation, as explored in prior studies like [7, 63].

To detect the damping term ϕ_{jk} , which typically arises from various sources of decoherence, we conduct an analysis of the total neutrino count rate in ground-based neutrino experiments.

This analysis involves fitting our theoretical models for SD using $\sigma_{\bar{p}}$ and PD using σ_L and σ_E to oscillation data. We define the χ^2 function as follows:

$$\chi^2(\sigma_n) = \min_{\vec{\alpha}} \sum_{i \text{ bins}} \frac{(R_i(\sigma_n, \vec{\alpha}) - R_i^{\text{data}})^2}{U_i} + \sum_j \left(\frac{b_j - b_j^0}{\sigma_j} \right)^2. \quad (4.32)$$

In this equation, R_i can represent either the observed rate or the ratio of the detected rates of near and far detectors. The term b_j corresponds to the pull parameters, which encompass both the oscillation parameters and the experimental uncertainties related to the rate. Additionally, U_i accounts for the statistical uncertainty associated with each bin.

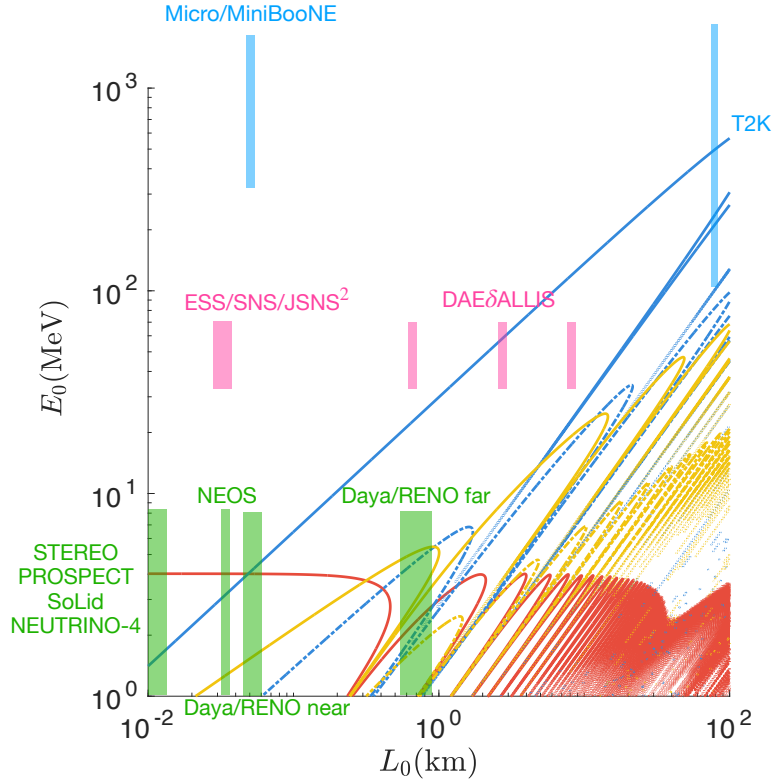


Figure 4.5: This figure is plotted to give us an idea on where to find neutrino decoherence effect among current ground-based experiments. The red, blue and yellow lines represent contours of $|P(\sigma_n \neq 0) - P(\sigma_n = 0)| = 10^{-6}$ for the solid lines and 10^{-4} for the dashed lines, for $n = L, E$ and \bar{p} , respectively, where the sensitivity would be higher below the lines. We set $\sigma_L = 3$ m $\sigma_E = 0.1\sqrt{E_0}$ MeV and $\sigma_{\bar{p}} = 0.1$ MeV as an example. Additionally, experiments (see [64] for a review) with their corresponding baseline and typical neutrino energies are labeled on the plot, for accelerator neutrinos (blue), decay-at-rest neutrinos (pink) and reactor neutrinos (green).

With the purpose of determining what experiments are more sensitive for each decoherence parameter, we plot Fig. 4.5, in which the red, blue and yellow lines represent contours of $|P(\sigma_n \neq 0) - P(\sigma_n = 0)| = 10^{-6}$ for the solid lines and 10^{-4} for the dashed lines, for $n = L, E$ and \bar{p}

respectively, giving us a hint of what experiments to look at for a certain σ_n . For simplicity, P represents the FTP on the third layer for $\bar{\nu}_e \rightarrow \bar{\nu}_e$ in this section. We can see from the figure that for all decoherence effects, the influence would be larger at lower energies, because the oscillation structure is denser along the \bar{p} and E axes, so the PWO effect is enhanced. Therefore, reactor neutrinos having the lowest energies for ground-based experiments would be the best candidate. Additionally, for vacuum oscillation, the decoherence effect by σ_L is small and does not depend on L_0 , hence, it is suitable for experiments near the source where the statistics are high, whereas $\sigma_{\bar{p}}$ and σ_E are more pronounced at larger distance. Moreover, a more realistic version of Fig. 4.5 for reactor neutrinos is plotted in Fig. 4.6 for the each σ_n , where the contour lines represent the rate difference between decoherent and coherent fluxes, $|\Phi(\sigma_n \neq 0) - \Phi(\sigma_n = 0)|$, considering the energy spectrum of neutrinos for RENO and also the diffusion over distance by

$$\Phi(\sigma_n; E_0, L_0) = \sqrt{N(E_0)} |P(\sigma_n \neq 0) - P(\sigma_n = 0)| \frac{L_{\text{bm}}}{L_0}, \quad (4.33)$$

where $L_{\text{bm}}/N(E_0)$ is the average distance/spectrum of the near detector for the RENO experiment.

To determine the sensitivity of different experiments to each decoherence parameter, we have created Fig. 4.5. In this figure, one can observe the red, blue, and yellow lines representing contours of $|P(\sigma_n \neq 0) - P(\sigma_n = 0)| = 10^{-6}$ for the solid lines and 10^{-4} for the dashed lines, where n denotes L , E , and \bar{p} , respectively. This figure provides valuable insights into which experiments are most suitable for detecting specific values of σ_n . For simplicity, we use P to denote the FTP on the third layer for the $\bar{\nu}_e \rightarrow \bar{\nu}_e$ channel in this section. From this figure, it is evident that decoherence effects are more pronounced at lower energies due to the denser oscillation structure along the \bar{p} and E axes, enhancing the PWO effect. Consequently, reactor neutrinos, which have lower energies in ground-based experiments, are more ideal candidates for detecting these effects. Furthermore, for vacuum oscillation, the influence of σ_L is minimal and independent of L_0 , making it suitable for experiments conducted close to the source with high statistical precision. Conversely, $\sigma_{\bar{p}}$ and σ_E effects become more pronounced at greater distances.

4.2.1 Reactor Neutrinos

For a more realistic representation of the sensitivity for reactor neutrinos, we have plotted Fig. 4.6 for each σ_n . In this figure, contour lines represent the rate difference between decoherent and coherent neutrino fluxes, denoted as $|\Phi(\sigma_n \neq 0) - \Phi(\sigma_n = 0)|$. We have taken into account the energy spectrum of neutrinos for the RENO experiment and considered the diffusion over distance using the following expression:

$$\Phi(\sigma_n; E_0, L_0) = \sqrt{N(E_0)} |P(\sigma_n \neq 0) - P(\sigma_n = 0)| \frac{L_{\text{bm}}}{L_0}, \quad (4.34)$$

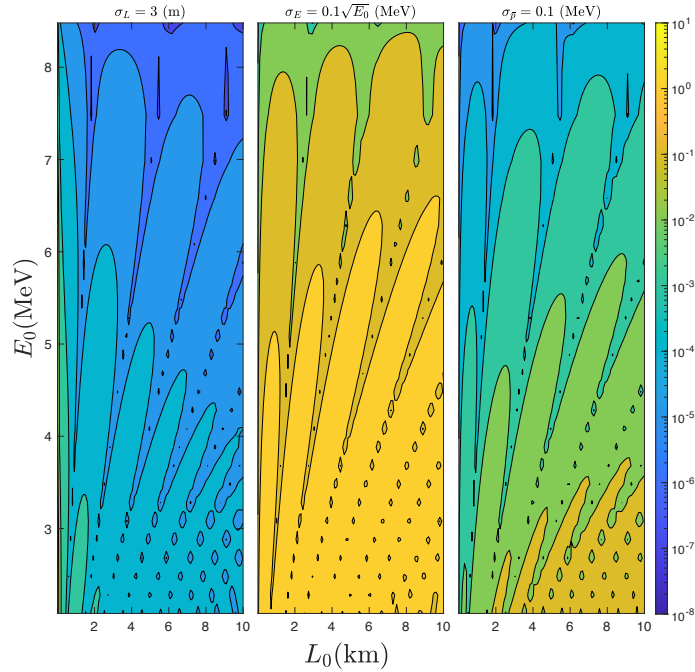


Figure 4.6: The contour plot of the flux difference, $|\Phi(\sigma_n \neq 0) - \Phi(\sigma_n = 0)|$ for reactor neutrinos, where the energy spectrum and the decrease with traveling distance for reactor neutrinos are taken into account. The formalism is given in Eq. (4.34).

Here, L_{bm} represents the average distance, and $N(E_0)$ represents the energy spectrum of the near detector for the RENO experiment.

We chose the RENO experiment as a benchmark to evaluate the amount of additional statistical data required for achieving sufficient sensitivity to each of the three decoherence parameters. Our sensitivity analysis was performed by fitting the decoherence parameters using the current RENO far-to-near ratio data from [65], following the approach outlined in Eq. (4.32). The results of our sensitivity analysis, obtained by fitting the decoherence parameters to the current RENO far-to-near ratio data [65], are presented in the three left plots of Fig. 4.7. In line with the formalism detailed in previous RENO publications [65–67] and in correspondence with Eq. (4.32), we define R_i^{data} as the observed far-to-near ratio of inverse beta decay candidates in the i -th energy bin after background subtraction, as provided in the supplementary material of [65]. The theoretical input for our analysis is given by:

$$R_i(\sigma_n, \vec{\alpha}) = (1 + \epsilon + f) \frac{1 + b^F}{1 + b^N} N_i^{\text{MC}}(\tau) \frac{\sum_{l=1}^6 P_i(L_{0,l}^{\text{far}}, \sin^2(2\theta_{13}), \Delta m_{ee}^2; \sigma_n)}{\sum_{l=1}^6 P_i(L_{0,l}^{\text{near}}, \sin^2(2\theta_{13}), \Delta m_{ee}^2; \sigma_n)}, \quad (4.35)$$

In this equation, f , ϵ , τ , b^F , and b^N represent the pull terms accounting for systematic uncertainties. Specifically, they address the uncorrelated reactor-flux systematic uncertainty, the uncorrelated detection uncertainty, the timing veto systematic uncertainty, and the background

uncertainties for the near and far detectors, respectively, as reported in [66]. The parameter τ denotes the uncorrelated energy-scale systematic uncertainty, introduced by scaling the energy as $E_0 \rightarrow (1 + \tau)E_0$. The term N_i^{MC} represents the near-to-far ratio without oscillation, derived from Monte Carlo data available in [65]. Additionally, $L^{\text{near}l}$ and $L^{\text{far}l}$ stand for the distances to the l -th near and far detectors, and $\sin^2(2\theta_{13})$ and Δm^2_{ee} are coherent oscillation parameters, where

$$\Delta m^2_{ee} = \cos^2 \theta_{12} \Delta m^2_{31} + \sin^2 \theta_{12} \Delta m^2_{32} \quad (4.36)$$

Finally, the three left plots in Fig. 4.7 were generated by minimizing the χ^2 -function using the Python package “iminuit” over two sets of parameters, $\vec{\alpha} = (\sin^2(2\theta_{13}), \Delta m^2_{ee}, f, \epsilon, \tau, b^F, b^N)$ and $\vec{\beta} = (\vec{\alpha}, \sigma_n)$, according to the equation:

$$\Delta\chi^2(\sigma_n) = \min_{\vec{\alpha}} \chi^2(\sigma_n) - \min_{\vec{\beta}} \chi^2. \quad (4.37)$$

To effectively marginalize the oscillation parameters, $\vec{\beta}$ is first minimized to obtain the best-fit values $s_0 = 0.087$ and $m_0 = 2.66 \times 10^{-3} \text{ eV}^2$, along with corresponding errors $\sigma_s = 0.023$ and $\sigma_m = 0.12 \times 10^{-3} \text{ eV}^2$ for $\sin^2(2\theta_{13})$ and Δm^2_{ee} , respectively. Two additional pull terms,

$$\chi^2 \rightarrow \chi^2 + \left(\frac{\sin^2(2\theta_{13}) - s_0}{\sigma_s} \right)^2 + \left(\frac{\Delta m^2_{ee} - m_0}{\sigma_m} \right)^2, \quad (4.38)$$

are then added to the χ^2 -function.

The results of the fitting process are presented in the three left plots of Fig. 4.7, and we consider the corresponding 90% CL limits as benchmark points. These benchmark values are as follows: $\sigma_E^{\text{bm}} = 0.12\sqrt{E_0} \text{ MeV}$, $\sigma_L^{\text{bm}} = 548 \text{ m}$, and $\sigma_p^{\text{bm}} = 1.6 \text{ MeV}$. Notably, the value of $\sigma_p^{\text{bm}} = 1.6 \text{ MeV}$ aligns with the analysis for the RENO experiment in [53, 54]. However, it is evident that σ_L^{bm} remains significantly larger than realistic values, which should be on the order of a few meters. In contrast, σ_E^{bm} appears to be in close agreement with the energy resolution, given by $\sigma_E/\sqrt{E_0} = 0.08\sqrt{E_0(\text{MeV})} + 0.3$ [66].

Additionally, in order to estimate the amount of additional statistical data required to achieve the desired sensitivity for a reasonable σ_n , we make the assumption that the statistical uncertainty will increase by a factor of $\sqrt{N_i}$ for each energy bin. Moreover, if the uncertainties associated with the pull parameters are sufficiently small and the signal count significantly outweighs the background count, it is feasible to consider only the statistical uncertainties in the χ^2 function. In such a scenario, we have:

$$\begin{aligned} \Delta\chi^2(\sigma_n) &\simeq \sum_{i \text{ bins}} N_i |P_i(\sigma_n) - P_i(\sigma_n = 0)|^2 \\ &= \sum_{i \text{ bins}} \lambda N_i^{\text{RENO}} \frac{L_{\text{RENO}}^2}{L_0^2} |P_i(\sigma_n^{\text{bm}}) - P_i(\sigma_n = 0)|^2 \frac{|P_i(\sigma_n) - P_i(\sigma_n = 0)|^2}{|P_i(\sigma_n^{\text{bm}}) - P_i(\sigma_n = 0)|^2}. \end{aligned} \quad (4.39)$$

Here, λ represents the factor by which we need to enhance the statistics to achieve a 90%

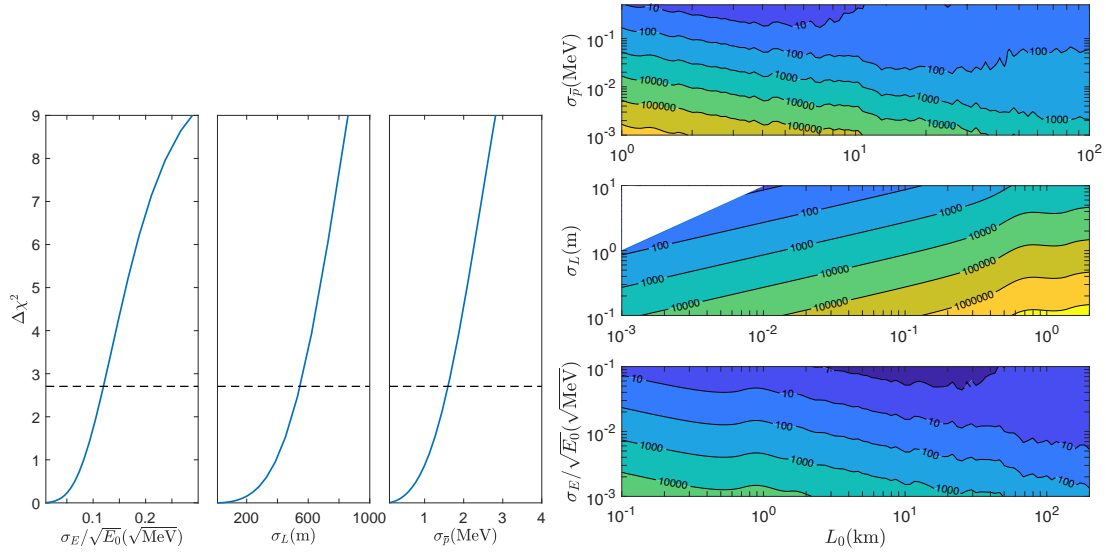


Figure 4.7: Taking RENO as a benchmark experiment for reactor neutrinos, the left three plots present the constraints on different decoherence parameters from a fit to RENO data. The right plot takes the obtained 90% CL limit on σ_n from the left plots. It shows the contour lines for evaluating how-many-times statistics compared to the current RENO data are needed to achieve a 90% CL sensitivity for some decoherence parameter and baseline, which is λ in Eq. (4.39). The white area in the middle figure is cut out since it would indicate that the detector is inside the reactor core.

confidence level signal for a specific value of σ_n . Moreover, when $\lambda = 1$, Eq. (4.39) implies summing over all the energy bins shown in Fig. 4.6 for a given σ_n^{bm} .

Therefore, using the benchmark values obtained from the three left plots in Fig. 4.7 and incorporating the flux difference from Fig. 4.6 into Eq. (4.39), we can examine the right plot in Fig. 4.7. This plot illustrates the extent to which we require additional statistical data (λ in Eq. (4.39)) compared to RENO in order to achieve a 90% confidence level sensitivity. Achieving this increment (λ) can be accomplished by several means, such as lowering the energy threshold for neutrino detection, increasing the reactor power, or simply allowing more data to accumulate over time. It is not surprising that we exhibit greater sensitivity to σ_E and σ_p at larger distances, despite the statistical decrease of $1/L_0^2$, while σ_L is more favorable for shorter propagation distances. Consequently, the ranges for L_0 have been selected accordingly in the plots. Furthermore, note that L_0 cannot be smaller than σ_L , which is why the triangular area in the upper left corner is left blank, and the edge of that area would be when the detector is located right by the source.

4.3 A Phase Measuring Proposal

In this section, we present a method for directly measuring the oscillation phase, which we refer to as the Phase Measuring Method (PMM). This method not only aims to quantify asymmetries

in the weighting functions but also provides a cleaner approach to measure neutrino oscillation signatures, as we will elaborate on in Section 4.3. Specifically, the measurement involves determining the shift of the coherent phase ψ_{jk} on the measurement layer by $\beta_{jk}(\vec{\sigma})$ as defined in Eq. (4.1) when there is an asymmetry in the weighting function. Technically, the key ingredient of this potentially realistic method, is to pinpoint the location of an oscillation extremum on the third layer. In terms of theoretical considerations, only the H_E -induced phase decoherence (PD) will make a non-negligible contribution for Gaussian-distributed weighting functions. Therefore, we assume a two-Gaussian distribution for $D_{\bar{p}}$ to introduce an asymmetry in the quantum uncertainties, while neglecting H_L -induced PD, as it has only a negligible impact on ground-based experiments. Finally, after introducing the PMM and evaluating the theoretical inputs and parametrizations (such as an asymmetry parameter denoted as "a" for the quantum uncertainties and the width σ_E for the energy uncertainty), we estimate the statistical and systematic uncertainties required to achieve a 90% confidence level (CL) sensitivity in the parameter space. This estimation is carried out while considering a π DAR neutrino source.

4.3.1 The Set Up

For some neutrino energy E_0 , the key point is to search for the deviation in distance (¹ L_{\min} - L_{osc}) caused by the phase shift. For the two-neutrino mixing scenario, we measure $L_{\min} = L_{\min}^{jk}$ in the equation

$$\psi_{jk}(L_{\text{osc}}^{jk}, E_0) = 2n\pi \rightarrow \psi_{jk}(L_{\min}^{jk}, E_0) + \beta_{jk}(L_{\min}^{jk}, E_0; \vec{\sigma}_n) = 2n\pi, \quad (4.40)$$

and observe how it deviates from $L_{\text{osc}}^{jk} = \frac{4\pi n E_0}{\Delta m_{jk}^2}$ due to an asymmetry in the decoherence effect. Furthermore, we can pinpoint the location of an extremum, and consequently, the signal is concentrated at a specific L_{\min} , rather than spanning an entire distribution. One notable advantage of this method is that, since we are seeking an extremum, the non-oscillating component of the event rate has minimal influence on the signal. Therefore, as long as other factors such as production rate, detection rate, background, etc., do not exhibit an extremum within the (L_0, E_0) range of interest, their contribution to the signal will be negligible.

In the context of a two-neutrino oscillation scenario, we focus on the first oscillation minimum and examine:

$$\Delta L_{\min}^{jk}(E_0; \vec{\sigma}_n) = L_{\min}^{jk}(E_0; \vec{\sigma}_n) - L_{\text{osc}}^{jk}(E_0) \simeq -\frac{2E_0}{\Delta m_{jk}^2} \beta_{jk}(E_0, \vec{\sigma}_n). \quad (4.41)$$

The above approximation of taking $\beta(L_{\min}^{jk}, E_0; \vec{\sigma}_n) \simeq \beta(L_{\text{osc}}^{jk}, E_0; \vec{\sigma}_n)$, is justified as we have verified that higher-order terms in the expansion of the left-hand side around the right-hand side can be safely neglected. For the three-neutrino mixing paradigm, in cases where we search around L_{osc}^{13} , the total L_{\min} corresponds to L_{\min}^{13} , because of the large difference between the atmospheric and solar mass splitting. As a result, complexities arising from interference between different mass splittings, including those from the damping terms, become negligible. However,

¹We will shortly explain why the local minimum would be more suitable for this method, therefore, we write L_{\min} as the extremum for now.

we still consider a complete three-neutrino mixing scenario in our simulations, even for the fully coherent case. Furthermore, in a similar manner, it is possible to find a specific E_{\min} for a given L_0 using Eq. (4.40). Nevertheless, attempting to discern effects by σ_E through ΔE_{\min} or σ_L through ΔL_{\min} is often infeasible, as the former is usually much larger than the latter. Consequently, while the uncertainties induce a phase shift, they are likely to diminish the sensitivity of the corresponding variable even further. Since σ_L is exceedingly small for ground-based neutrino sources, even with regard to ΔE_{\min} , we do not include it in this section.

For the purpose of this thesis, our focus is on the phase shift resulting from decoherence effects. However, it is important to note that the PMM exclusively measures the (effective) neutrino oscillation phase, encompassing measurements such as the neutrino mass splitting, CP phase, mass hierarchy, or even the presence of an additional sterile neutrino. Therefore, a comprehensive analysis of all pertinent experiments, incorporating decoherence effects, may be necessary. Fortunately, as we will demonstrate, the contributions to ΔL_{\min} from mass splitting uncertainties (which can also indicate the mass hierarchy) scale with E_0 , while those stemming from the asymmetry in intrinsic quantum uncertainties saturate to a constant value for E_0 above approximately 5-10 MeV. Consequently, these contributions exhibit distinct dependencies on E_0 . Additionally, we will show that the phase shift term resulting from quantum decoherence effects is insensitive to traditional measurements of the neutrino spectrum, whereas other fundamental oscillation parameters are determined with increasing precision through these measurements. As a simplification and for illustrative purposes, we adopt fixed neutrino masses determined by global analyses [52], assume a three-flavor oscillation with normal mass ordering, and set $\delta_{\text{CP}} = \pi$ in this section.

In practical terms, the process of finding L_{\min} involves scanning over L_0 (e.g., by adjusting the detector's position) around the expected location of the first local minimum for a given neutrino energy E_0 . To achieve this, we consider the counting of neutrinos within position bins of width ΔL_{bin} :

$$N_i(E_0; \vec{\sigma}_n) = N(E_0) \int_{L_i - \Delta L_{\text{bin}}/2}^{L_i + \Delta L_{\text{bin}}/2} dL_0 \frac{1}{4\pi L_0^2} P_{\nu_\alpha \rightarrow \nu_\beta}(L_0, E_0; \vec{\sigma}_n), \quad (4.42)$$

where $N(E_0)$ represents the number of produced neutrinos multiplied by the detection rate, which remains independent of the travel distance L_0 . While we have assumed no neutrino loss or gain during propagation, accounting for such effects would only trivially impact the signal of L_{\min} , provided they do not create significant bumps or dips at specific L_0 values within our region of interest. To determine L_{\min} , we examine when the normalized numerical derivative of N_i , given by

$$F_i(E_0; \vec{\sigma}_n) = \frac{1}{\bar{N}_i} \frac{N_{i+1}(E_0; \vec{\sigma}_n) - N_i(E_0; \vec{\sigma}_n)}{L_{i+1} - L_i}, \quad (4.43)$$

reaching zero.

The red dots in Fig. 4.8 represent F_i , while the vertical dashed lines denote the position bins, $L_i \pm \Delta L_{\text{bin}}/2$. Here, $\bar{N}_i = (N_{i+1}(E_0; \vec{\sigma}_n) + N_i(E_0; \vec{\sigma}_n))/2$ serves as the normalization

factor, eliminating correlated uncertainties between position bins, similar to the role of near-far detectors. It is important to note that the bin size must be much smaller than L_{osc} to observe a “local” minimum.

Consequently, L_{min} corresponds to the point where the blue line connecting all dots ($F(L_0)$) intersects with the black line $F(L_0) = 0$, with the uncertainty indicated by the red horizontal bars in Fig. 4.8. To determine this uncertainty:

1. Propagate the uncertainty of the count numbers N_i (both systematic and statistical, denoted as $\Delta_{\text{sys}}/\Delta_{\text{stat}}$) to the uncertainties of F_i using the relation in Eq.(4.43), as shown by the blue error bars in the left plot of Fig.4.8. This step retains only uncorrelated uncertainties due to the normalization factor \bar{N} .
2. Connect (or fit) the error bars of F_i (i.e. , $F_i \pm \sqrt{\Delta_{\text{sys}}^2 + \Delta_{\text{stat}}^2}$) and create an uncertainty band, as demonstrated in the left plot of Fig. 4.8.
3. The uncertainty of L_{min} is determined by the intersection between the uncertainty band and $F(L_0) = 0$, marked as red error bars in the left plot of Fig.4.8. In some cases, this intersection can be infinite if the error of the maximal $|F_i|$ exceeds its value, as illustrated in the right plot of Fig.4.8, where the sensitivity of ΔL_{min} becomes infinite when the statistics are too low.

Moreover, the uncertainties depend on the chosen bin size, as depicted in the middle plot of Fig. 4.8. When $\Delta L_{\text{bin}} \ll L_{\text{osc}}$, increasing the position bin size decreases the uncertainty. This is a two-fold reason for this effect: 1) the statistics within each bin increase, reducing the statistical uncertainty, and 2) the bin size enhances F_i , reducing the uncertainty of L_{min} . In fact, for an oscillatory function such as $\sin(L/L_{\text{osc}})$ (analogous to the FTP), its discrete derivative due to binning (corresponding to F_i) is:

$$\tilde{F}_i = \frac{1}{L_{\text{osc}}} \int_{L_i - \Delta L_{\text{bin}}/2}^{L_i + \Delta L_{\text{bin}}/2} dL \cos\left(\frac{L}{L_{\text{osc}}}\right) \simeq \frac{\Delta L_{\text{bin}}}{L_{\text{osc}}}. \quad (4.44)$$

This approximation is valid when $(L_i \pm \Delta L_{\text{bin}})/L_{\text{osc}} \sim 2n\pi$ for some integer n , which is well justified since we only search around the oscillation minimum. As such, we see that for a fixed bin size, the signal is smaller at higher energies, leading to larger uncertainties. For example, with $\Delta L_{\text{bin}} = \mathcal{O}(10)$ m and $\Delta_{\text{sys}} = \mathcal{O}(1)$, the energy range with finite sensitivity typically spans a few MeV. Furthermore, even though α_0 in the expansion $N_i = \sum_i \alpha_i L_0^i$ is canceled out for the signal, it still carries uncorrelated uncertainties. Therefore, in cases where $\alpha_0 \ll \alpha_i$ for some $i \neq 0$, the uncertainty of L_{min} significantly increases. This situation arises when observing neutrinos around the maximum oscillation value or when searching for disappearing neutrinos. Consequently, rare event measurements of appearance channels at minimum oscillation phases would be the preferred choice for our method.

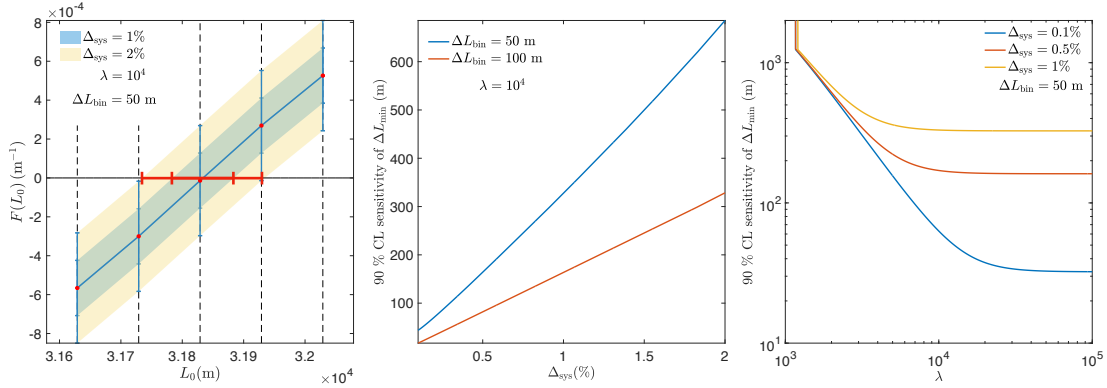


Figure 4.8: The left plot shows how we determine L_{min} for neutrinos with 30 MeV energy and its uncertainty (red error bars) from Eq. (4.43) (blue error bars) considering two different systematic uncertainties labeled in the plot. Here we consider the JSNS setup by taking Eq. (4.45) for $N(E_0)$ in Eq. (4.42), and each bin is separated by the black dashed lines, hence the parameters which would influence the uncertainty of L_{min} are the systematic uncertainty (Δ_{sys}), the statistical uncertainties (λ : increment w.r.t. the JSNS set up) and the bin size (ΔL_{bin}). The middle and right plot show how these parameters would influence the sensitivity for ΔL_{min} through simulating the uncertainties of L_{min} . In particular, the middle plot corresponds to Eq. (4.44), and the right plot shows when systematic/statistic uncertainties dominate over one another. Specific steps to determine L_{min} and more discussions on the plots are given in the text.

4.3.2 Decay at Rest Neutrinos

By taking a 50 m (around the detector size of Hyper-K [68] and the DUNE far detector [69]) bin size, only reactor neutrinos and DAR neutrino are in the energy range which leads to an appropriate oscillation length. In particular, the monochromatic neutrinos from π DAR are most suitable for the PMM with just one measurement, due to the following reasons:

- The monochromatic neutrinos are produced sharply around 30 MeV, which is suitable for a 50 m bin size as we have demonstrated in Fig. 4.8.
- It provides a detectable appearance channel by producing ν_μ which could oscillate into ν_e . On the other hand, reactors only produce $\bar{\nu}_e$, hence its appearance channels are not detectable since $\bar{\nu}_\mu$ will be below the Cerenkov threshold in the sub MeV range.
- Since we consider a fixed E_0 , the monochromatic feature automatically satisfies the condition without wasting any neutrinos spread out in the spectrum. Hence, statistics-wise, on top of the bright spallation source, it would be better than having μ DAR neutrinos if we only consider measurements of L_{min} at a single E_0 .
- The systematic uncertainty would also be strongly reduced for π DAR neutrinos. First of all, the timing structure of DAR experiments [70–72] would enable identification between π DAR neutrinos and μ DAR neutrinos. In fact, $\bar{\nu}_\mu \rightarrow \bar{\nu}_e$ from μ DAR would suffer from an intrinsic uncertainty since the $\bar{\nu}_\mu$ and $\bar{\nu}_e$ production are indistinguishable [70–72]. Sec-

only, the energy reconstruction would be highly accurate for monochromatic neutrinos. Discussions on this topic can be found in [73].

Similar to what we did for RMM, we consider a benchmark experiment, and ask how far we are to having enough sensitivity for some decoherence parameters. In particular, we take numbers from the existing JSNS experiment [70], i.e. 1.114×10^{23} proton-on-targets for 1 MeV power within 3 year, from which 64% would contribute to a π DAR process, producing monochromatic ν_μ which would oscillate into ν_e and be detected by a 17-ton gadolinium loaded liquid scintillator. Hence, for Eq. (4.42), we obtain

$$\frac{N(E_0)}{4\pi L_0^2} \simeq 0.43 \frac{1}{\text{m}^2} \left(\frac{P}{1 \text{ MeV}} \right) \left(\frac{T}{3 \text{ yr}} \right) \left(\frac{M_D}{17 \text{ ton}} \right) \left(\frac{31829 \text{ m}}{L_0} \right)^2. \quad (4.45)$$

Here, we adopted the cross-section for quasielastic scattering of ν_e on proton from [74] as $7.5 \times 10^{-41} \text{ cm}^{-2}$ at 30 MeV, and assume that the detector is moved to the oscillation minimum (the actual JSNS detector is placed 24 m from the source). In Fig. 4.8 we adjust the equation above by moving L_0 around its first oscillation minimum, then increase it λ times. In addition, similar to other DAR channels [70, 75], the systematic uncertainties should be dominated by intrinsic uncertainties, i.e. the $\bar{\nu}_e$ produced by μ DAR, which take up approximately 3% of total amount of neutrinos produced at 30 MeV. Furthermore, one could also identify whether a neutrino comes from π DAR from the timing structure, for instance, in the JSNS setup, $\bar{\nu}_e$ from μ DAR takes up only $< 10\%$ of the early time bin which is dominated by ν_e from π DAR [70]. Hence, we take various systematic uncertainties in the range of 0.1-2% in Fig. 4.8. From the middle and right plot of Fig. 4.8, we find the sensitivity for some ΔL_{\min} by first estimating the uncertainty of L_{osc} (i.e. when $\Delta L_{\min}=0$) for some systematic and statistical uncertainty (from Δ_{sys} and λ), then further identify what values of ΔL_{\min} would be rejected by such data at 90% CL. Theoretical estimates for decoherence effects which lead to such ΔL_{\min} will be shown in the following paragraph.

The phase shift from decoherence effect for ground-based neutrinos would mainly come from the asymmetry of quantum uncertainties decided by the weighting function $D_{\bar{p}}$ and the classical (statistical) energy uncertainty with weighting function H_E . In particular, we consider H_E being dominated by the energy resolution (i.e. H_E is Gaussian distributed) and $D_{\bar{p}}$ as a two-Gaussian distribution generically formalised as

$$D_{\bar{p}}(\bar{p} \equiv |\bar{p}|; E_0) = \frac{1}{2\sqrt{\pi}\sigma'_{\bar{p}}(1+rs)} \left\{ \exp\left(\frac{-(\bar{p}-E_0+dE_0)^2}{4\sigma_{\bar{p}}'^2}\right) + r \exp\left(\frac{-(\bar{p}-E_0-dE_0)^2}{4(s\sigma'_{\bar{p}})^2}\right) \right\}, \quad (4.46)$$

where the width is $\sigma_{\bar{p}} = (1+rs)\sigma'_{\bar{p}}$, according to the definition in Appendix A. This formalism represents scenarios such as neutrino produced or detected with two types of interactions simultaneously, with different probabilities and widths (r, s) and have slightly different expectation values for E_0 ($E_0 \pm dE_0$, in particular). Moreover, with the phase structure given in Eq. (4.25), the decoherence term is simply the Fourier transformation of $D(\bar{p}; E_0)$ from \bar{p} to

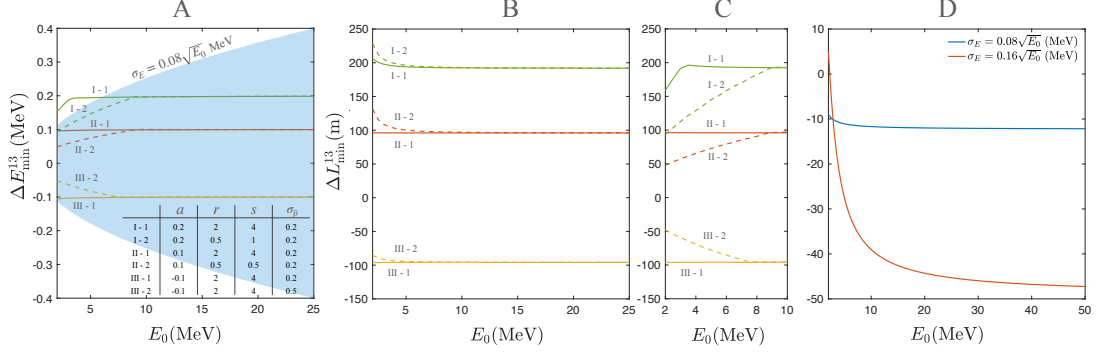


Figure 4.9: Plot A (B, C) shows the variation of E_{\min}^{13} (L_{\min}^{13}) for a number of quantum uncertainty parameters for Eq. (4.46). The labels for each line (as well as its colour and style) on all three plots (and also in Fig. 4.10) correspond to the table on Plot A, while Plot A and C consider a constrain by $\sigma_E = 0.08\sqrt{E_0}$ MeV (blue area in Plot A) in addition. Plot D shows the variation of L_{\min}^{13} caused by σ_E from a Gaussian distributed energy resolution.

$\alpha_{jk} = \Delta m_{jk}^2 L_0 / (2E_0^2)$, and the phase shift is

$$\beta_{jk}(E_0, \sigma_{\bar{p}}) = \tan^{-1} \left(\frac{1 - r s e^{-(s^2-1)\alpha_{\bar{p},jk}^2 \sigma_{\bar{p}}'^2}}{1 + r s e^{-(s^2-1)\alpha_{\bar{p},jk}^2 \sigma_{\bar{p}}'^2}} \tan(\alpha_{\bar{p},jk} dE_0) \right) \xrightarrow{\alpha_{\bar{p},jk} \ll 1} \frac{1 - r s}{1 + r s} \frac{\Delta m_{jk}^2 L_0}{2E_0^2} dE_0. \quad (4.47)$$

Furthermore, the fact that we search around the first minimum ($\psi = 2\pi$) and $\beta_{jk} \ll L_{\min}^{\text{osc}}$ implies that $\Delta m_{jk}^2 L_0 / (2E_0) \simeq 2\pi$, hence

$$\Delta L_{\min}^{jk} \simeq \frac{2\pi}{2.53 \Delta m_{jk}^2} a, \quad (4.48)$$

at high energies, where

$$a = \frac{1 - r s}{1 + r s} dE_0. \quad (4.49)$$

This can be seen in Fig. 4.9, where lines having the same a merge to one constant value at higher energies which is independent of both E_0 and $\sigma_{\bar{p}}$. Such property is not generic for all sources of decoherence effect, in fact, only $\alpha_{\bar{p},jk}$ from the phase structure $\eta_{jk} = i\alpha_{\bar{p},jk}\bar{p}$, cancels out the energy dependence with L_{osc}^{jk} in Eq. (4.41) exactly. For instance, in Plot D of Fig. 4.10, ΔL_{\min}^{13} increases with energy only because σ_E does as well. In fact, if σ_E is not energy dependent, it would approach zero at large E_0 . Moreover, from Eq. (4.48) we can see that when $s = 1$, i.e. the two bumps have the same width, $\sigma_{\bar{p}}$ would have no role in the phase shift. In addition, the variance of H_E (Δ_E , weighting function on the second layer with width σ_E) must be larger or equal to that of $D_{\bar{p}}$ ($\Delta_{\bar{p}}$). In fact, when they are equal to one another, the energy would be measured to a quantum level. Hence if one keeps on lowering Δ_E , $\Delta_{\bar{p}}$ would be forced to lower accordingly and the uncertainty of \bar{x} would increase in order to fulfil the uncertainty principle. In this case, if we consider $\sigma_E = 0.08\sqrt{E_0}$, and scale $D_{\bar{p}}$ by scaling $\sigma_{\bar{p}}$ and dE_0 simultaneously to fit the constrain $\Delta_{\bar{p}} = \Delta_E$, we find a change from Plot B to Plot A and C in Fig. 4.9. Plot B,

on the other hand, assumes that σ_E is large enough (in this case, $\sigma_E \geq 0.17\sqrt{E_0}$) such that the quantum uncertainties are un-squeezed. Furthermore, we can see that the dashed lines are more influenced by the constraint from Δ_E than the solid lines, since they either have a larger dE_0 or $\sigma_{\bar{p}}$, both indicating a larger $\Delta_{\bar{p}}$. From plot A, we can see that if σ_E is small, it would squeeze $D_{\bar{p}}$ and lower the phase shift; on the other hand, if σ_E is large, then the blue area covers all the lines and there will not be enough sensitivity. Therefore, while there is still a little space out of the sensitivity line, ΔE_{\min} it is also not a suitable approach to measure a $D_{\bar{p}}$ -induced phase shift.

Finally, we estimate the sensitivity for the benchmarks in Fig. 4.9 for the PMM in the right plot of Fig. 4.10. Furthermore, in the left plot, we demonstrate how the RMM is not as sensitive to the phase shift term compared to the damping term. The blue band is the range of $D_{\bar{p}}$ -induced state decoherence which is not constrained by the combined analysis of reactor experiments from [54], i.e. the upper edge of the band represents $W_{\bar{p}}$ as a Gaussian with width $\sigma_{\bar{p}} = 0.47$ MeV. On the other hand, while having $\mathcal{O}(100)$ m of ΔL_{\min} for the PMM, the colored lines (with the same parameter as those in Fig. 4.9) do not vary the FTP to an extent that is close to the limit set by the combined analysis (not to mention for just one single experiment). Moreover, while the RMM significantly depends on how the neutrino spectrum would be without oscillation, the phase shift, which slightly shifts the FTP, does not change the shape of the spectrum as the damping term does, hence, it can be easily compensated by non-oscillation related models. On the contrary, for the PMM, the signal is amplified by the oscillation length and is nearly independent of non-oscillation related models. The main disadvantage is the lack of statistics since we aim at searching for appearing flavors at the oscillation minimum. Nonetheless, from the right plot in Fig. 4.10, we see that with the increment mainly by the detector size, the statistics would be enough for a 90% CL sensitivity for a range of decoherence asymmetry parameters of the quantum and classical uncertainties. Specifically, compared to the 17 T detector mass and a cross section of 7.5×10^{-41} cm² of JSNS, the DUNE detector would have an increased detector mass of 40 kT, and the liquid argon material of the detector also enhances the cross section to 2.5×10^{-40} cm² at 30 MeV [76], hence $\lambda \simeq 7.8 \times 10^3$ in this case (red lines). As for the ESS setup proposed in [77], while using a water Cherenkov detector implies a lower cross section (3×10^{-42} cm² at 30 MeV [78]), the detector mass would be increased to 538 kT, and the spallation source is also brighter by having 2.7×10^{23} POT per year.

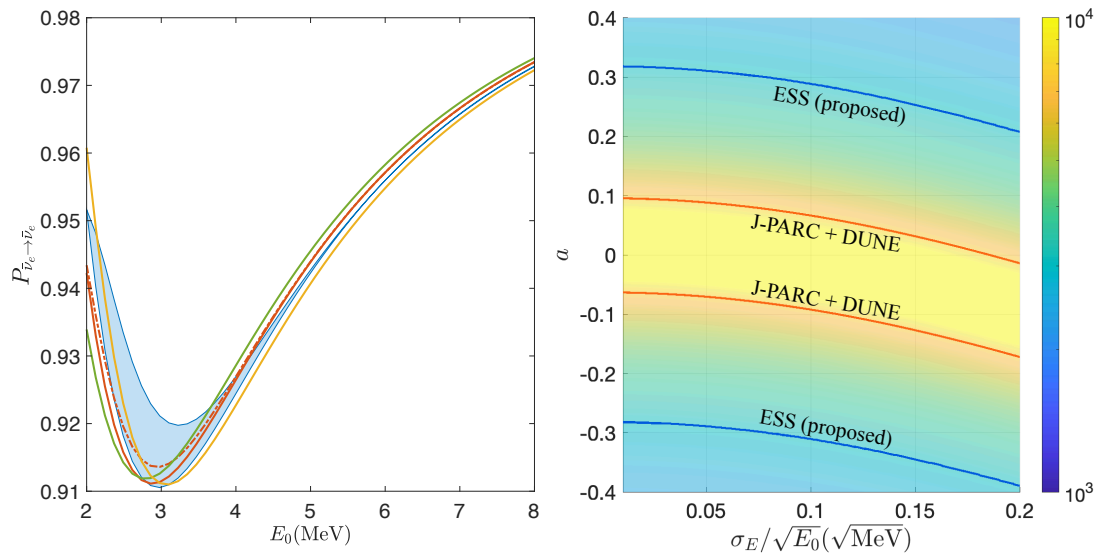


Figure 4.10: The left plot shows how the phase shift term is not sensitive to the rate measuring method compared to the damping term: The upper edge of the blue band represents the transition probability for $\sigma_{\bar{p}}$ at its upper limit given in [54] for a Gaussian distributed $D_{\bar{p}}$, and the lower edge is the fully coherent case. The colour code of the lines corresponds to the same decoherence parameters given in Fig. 4.9, which are within the parameter space in the right plot. The right plot shows values of λ in Eq. (4.45) required to achieve a 90% CL sensitivity for the decoherence parameter space by the colour bar. The red line labeled “J-PARC+DUNE” gives the required λ by assuming a J-PARC-like source combined with a DUNE-like detector; and similarly, the blue line labeled “ESS (proposed)” considers one year of data taking of the ESS source and the water Cherenkov detector proposed in [77]. Both cases are assumed to have the baseline L_0 at the first oscillation minimum at 30 MeV (31829 m).

Chapter 5

High Energy Neutrino Magnetic Moment

Contents

5.1 Production of High Energy Neutrinos	75
5.2 Neutrino Magnetic Moment Effect	84

In this chapter, we investigate the phenomenon of helicity flip due to the neutrino magnetic moment (ν MM) effect, as introduced in Sec. 2.1.2. By paying particular attention to neutrinos with energies exceeding 100 TeV, an astrophysical source is indicated. In such cases, it is anticipated that neutrinos at these extreme energies experience a significant magnetic field environment at their production sites, leading to the sizeable magnetic moment effects. Within this thesis, we investigate a simple yet heuristic model concerning neutrinos originating from a single source to illustrate this phenomenon.

In Section 2.1.3, we explore the characteristic length scales governing phenomena like neutrino mass splitting, MSW effect, and the ν MM effect. We specify the conditions under which these effects can be considered independent of another. In particular, we find that the ν MM effect can be considered decoupled from mass splitting. More specifically, within the upper bound imposed by current experimental constraints ($\mu_\nu \lesssim 10^{-12} \mu_B$, represented by the red line) and the benchmark point arising from standard model loop effects for SM extended massive Dirac neutrinos ($\mu_\nu \sim 10^{-19} \mu_B$, indicated by the purple line), there exist two length scales, denoted as L_1 and L_2 , such that the ν MM effect dominates when $\ell < L_1$, the state remains constant when $L_1 < \ell < L_2$, and mass splitting becomes dominant beyond $L_2 < \ell$. Here, ℓ denotes the neutrino's propagation distance. If $\mu_\nu \ll 10^{-19} \mu_B$, the decouple condition would still hold, however, the ν MM effect might be negligible. This situation applies to neutrinos produced by a single source with a strong dipolar magnetic field, which decreases by ℓ^{-3} , such as those emitted

by neutron stars. Thus, as long as neutrinos are generated within a distance of approximately 10^7 km above the star, the transition from $L_{\text{mag}}^{-1} \gg L_{\text{mass}}^{-1}$ to $L_{\text{mag}}^{-1} \ll L_{\text{mass}}^{-1}$ will occur within region (I) of the neutrino propagation. Consequently, the ν MM effect will dominate in region (I), while mass splitting will dominate in region (II) up to the decoherence length scale, where the transition probability remains constant over time in region (III).

Having established that the decouple limit is reached for Majorana neutrinos from Fig. 5.1, Eq. (2.15) can be adopted as:

$$P_{\alpha\beta}^{hh'} \simeq \sum_{\delta} P_{\alpha\delta}^{hh'} (\mathcal{H} = \mathcal{H}_{\nu\text{MM}}) \times P_{\delta\beta}^{h'h'} (\mathcal{H} = \mathcal{H}_{\text{mass}}). \quad (5.1)$$

Since neutrinos are fully decohered upon the arrival at earth, the latter term is $P_{\delta\beta}^{h'h'} = \sum_{j,k} U_{\delta j}^* U_{\beta j} U_{\delta k} U_{\beta k}^*$ when h' denotes neutrinos, and $P_{\delta\beta}^{h'h'} = \sum_{j,k} U_{\delta j} U_{\beta j}^* U_{\delta k}^* U_{\beta k}$ when h' denotes anti-neutrinos. As for the former term in Eq. (5.1), we will adopt the results obtained in Eq. 2.23, restating them here for convenience:

$$P_{\alpha\beta}^{\text{HC}} = \sum_{j,k} \tilde{U}_{\alpha j}^* \tilde{U}_{\beta j} \tilde{U}_{\alpha k} \tilde{U}_{\beta k}^* \phi_{jk}^{\text{HC}} \cos \theta_j \cos \theta_k, \quad (5.2)$$

$$P_{\alpha\beta}^{\text{HF}} = \sum_{j,k,\gamma,\delta} \hat{\mu}_{\alpha\gamma}^* \hat{\mu}_{\alpha\delta} \tilde{U}_{\gamma j}^* \tilde{U}_{\beta j} \tilde{U}_{\delta k} \tilde{U}_{\beta k}^* \phi_{jk}^{\text{HF}} \sin \theta_j \sin \theta_k, \quad (5.3)$$

where ‘‘HC’’ means helicity is conserved ($h = h'$), and ‘‘HF’’ stands for helicity flipped ($h \neq h'$). For a closed quantum system, $\phi_{jk}^{\text{HC}} = \phi_{jk}^{\text{HF}} = 1$ for all j, k , and the effect will be determined by the oscillation phase:

$$\theta_\nu = \mu_\nu \int_0^{L_{\text{cut}}} d\ell B_\perp(\ell) e^{i\phi(\ell)}, \quad (5.4)$$

for any $L_1 < L_{\text{cut}} < L_2$. Here, $\theta_2 = \theta_3 = \theta_\nu$ while $\theta_1 = 0$, and the mixing matrix, \tilde{U} , determines the flavour structure plotted in Fig. 2.1.

As for Dirac neutrinos, there will be modes where $\Delta m_{jk}^2 = 0$ from the cancellation between $\mathcal{H}^{11/22}$ and $\mathcal{H}^{33/44}$ in Eq. (2.6) and Eq. (2.8). Therefore, ν MM effect could be relevant in all regions. However, the ν MM effect for Dirac neutrino can only cause a loss of the neutrino flux, $\phi_\alpha \rightarrow \phi_\alpha(1 - f_\alpha)$, since only left handed neutrinos (ν_L and $\bar{\nu}_L$) are visible to detection via weak interaction. Therefore, since we only look at the flavour and/or helicity ratio for neutrino above 100 TeV in the adiabatic limit, this effect would cancel out if either 1) $\mu_{\alpha\beta}$ is symmetric 2) $f_\alpha \ll 1$ or 3) the ν MM is large enough such that $f_\alpha \rightarrow 1/2$. In other words, the parameters would have to lie in a sweet spot: being both non-symmetric and within a certain range of values, to have a detectable effect from the ratio. Nonetheless, if one goes to a lower energy where there will be some interplay between the mass-splitting and/or matter effect, then there could be signature in the spectrum [79]. However, this is not the focus of this thesis, as we concentrate on high-energy neutrinos and examines ratios rather than full spectra. It should be mentioned that there is a possibility of detecting flavor ratio signatures from Dirac neutrinos at high energies, as demonstrated in [79]. This phenomenon is induced by the galactic magnetic

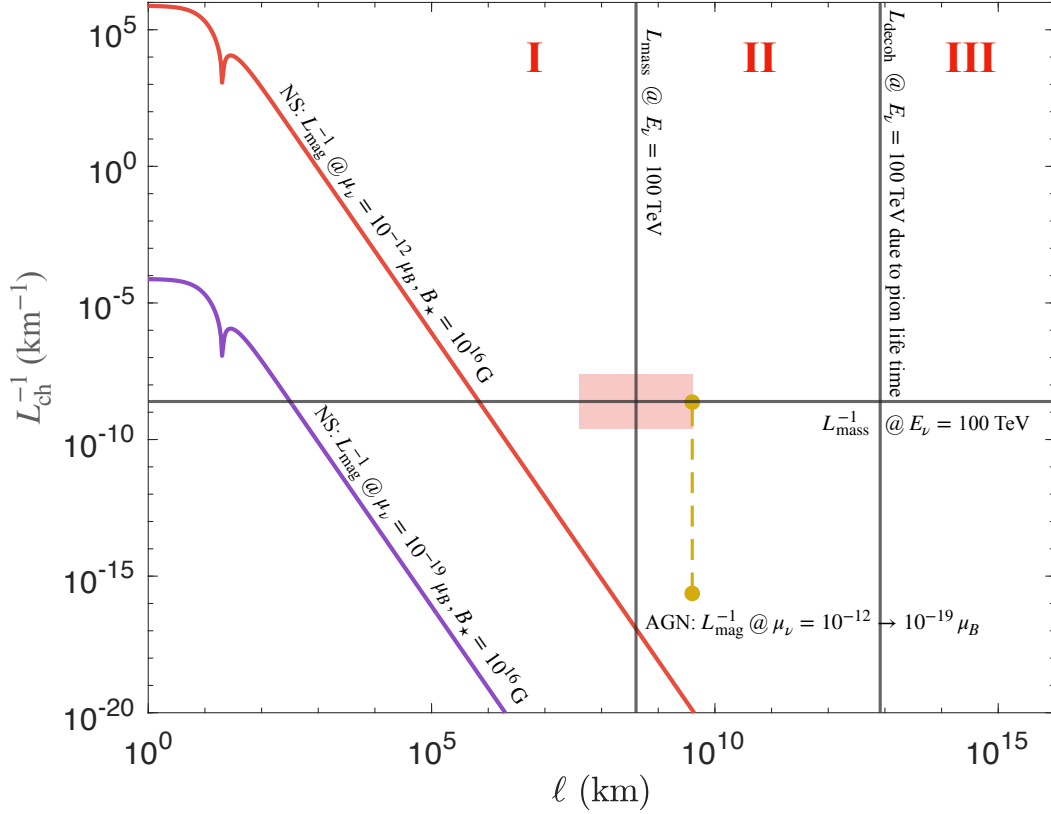


Figure 5.1: Length-scales for ν MM effect (colorful solid lines), mass-splitting(left vertical line), and decoherence (right vertical line) as functions of propagation distance of neutrinos ℓ .

field under specific conditions: 1) there exists an asymmetry in the ν MM matrix (e.g., only ν_μ is non-zero), 2) the evolution is not entirely adiabatic, and 3) the neutrinos come solely from a single source. However, this scenario is not the primary focus of this work since we examine ν MM induced by the magnetic field at the source, which, as we will discuss in the next section, may be considered as adiabatic. Naturally, there may be additional contributions from the galactic magnetic field after region (III); however, due to the flavor ratio's accumulation of contributions from multiple sources, such effects tend to cancel out as demonstrated in [79].

5.1 Production of High Energy Neutrinos

To fuel a neutrino to a PeV level or more, the powering sources are expected to be highly dynamical at least over the period when the neutrinos are produced. Relativistic protons p are long-thought as triggers of processes producing such high-energy neutrinos via $p-p$ or $p-\gamma$ collisions [80]. Although the sources as well as the acceleration mechanism for such high energy

particles are still unknown, there is a requirement that the protons be confined in region to be accelerated sufficiently. Such requirement is dictated as the Hillas condition [81, 82], protons in an acceleration region with the comoving size of R , threaded by a magnetic field with a strength of B , could acquire energy up to the upper limit given by

$$E_{\max}^p = \eta^{-1} e B L \Gamma \simeq 10^5 \left(\frac{\eta}{10^2} \right) \left(\frac{B}{3 \times 10^5 \text{G}} \right) \left(\frac{R}{10^5 \text{km}} \right) \text{PeV} \quad (5.5)$$

where η is the acceleration efficiency which depends on acceleration mechanism and the velocity of the moving source (i.e., the Lorentz factor).

On top of the above necessary condition, the energy acquisition of the rendered ν 's is limited by various cooling processes experienced by protons as well as the mesons during hierarchical decays. In systems threaded by a strong magnetic field and the collision of particles is active, as the scenario considered here, the most relevant ones are the synchrotron and adiabatic coolings with the timescales [83]

$$t_{\text{syn}} = \frac{q^4 B^2 E}{9\pi m^4}, \quad (5.6)$$

and

$$t_{\text{ad}}^{-1} = \frac{R}{v}, \quad (5.7)$$

respectively. Here q , m , and E are the charge, mass, and the energy of the particle, v is the characteristic speed of the generation site, and B is the characteristic magnetic strength. The dissipation time is then defined through

$$t_{\text{dis}}^{-1} = t_{\text{syn}}^{-1} + t_{\text{ad}}^{-1} + \dots, \quad (5.8)$$

where the dots symbolically denote other minor contributions, e.g., hadronic processes. It shall be explained later that the synchrotron cooling, which scales with the square of magnetic strength, plays the major role for the present study (cf. Fig. 5.2).

The generation channel of neutrinos can be divided into three possibilities depending on the acceleration (t_{acc}) and cooling ($t_{\text{dis,p}}$) timescales of protons, and the cooling ($t_{\text{dis,m}}$) and decay (t_{decay}) timescale of the mesons: (i) For $t_{\text{acc}} > t_{\text{dis,p}}$, the protons are unable to be sufficiently accelerated, thus no high energy neutrino is expected. (ii) For $t_{\text{acc}} < t_{\text{dis,p}}$, and $t_{\text{decay}} > t_{\text{dis,m}}$, protons can be highly accelerated then generate mesons through p - p and/or p - γ collisions, while the mesons will not have enough time to pass over their energy to daughter particles before being cooled down. (iii) For $t_{\text{acc}} < t_{\text{dis,p}}$, and $t_{\text{decay}} < t_{\text{dis,m}}$, protons can be energetic to render mesons, and the latter decays to create neutrinos with a portion of its energy. For each of aforementioned scenarios, the balance between several time scales will amount to a suppression in neutrinos' energy, which we phenomenologically describe as an efficiency parameter $f = f_p f_m (< 1)$ that are a combination of factors of proton acceleration, f_p , and meson decay, f_m . The introduced

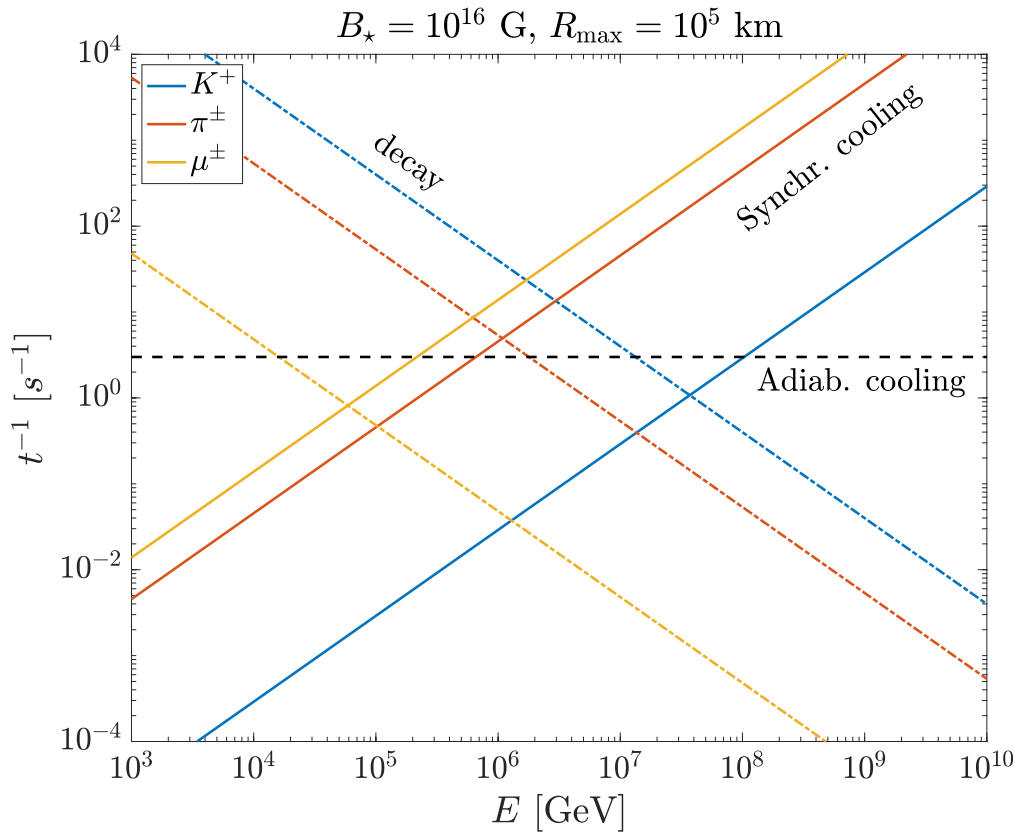


Figure 5.2: Adiabatic (black dashed) and synchrotron (colorful solid) cooling timescales for secondary mesons, viz. μ^\pm , π^\pm , and K^+ . Their decay timescales are overplotted (colorful dash-dotted). We assume that neutrinos are produced on a shell surrounding a magnetar (see the main text for details) with radius $R_{\max} = 10^5$ km, and the magnetar is embedded with a dipolar magnetic field with the magnetic strength at the pole being $B_\star = 10^{16}$ G. The geometry of the scenario can be found in Fig. 5.3.

f accounts for the cutoff in the higher end of the spectrum, while the flavour and neutrino-antineutrino ratios are mutually decided by both f_p and f_m (e.g., [84]).

Our main goal here is not to simulate a realistic flux including due details, but rather to illustrate qualitatively how a non-trivial NMM nature (anti)neutrinos can adjust the pattern of signal on triangle plots. To this end, we specify ourselves to the remnant systems of BNS mergers, where the SGRB may be launched at radius $r = 10^5$ km assuming the fireball model [REFs]. It is generally assumed that the dominant dissipations in proton's energy are the adiabatic loss due to the expansion of the shell and the synchrotron loss of the protons due to the magnetic fields present in the shells. Considering that the remnant system harbors a dipolar magnetic field with the strength $B_\star = 10^{16}$ G at the pole of the central massive NS, and taking the radius R_{\max} of the neutrino's generation site, we plot the timescales of the above two cooling effects, where we have assumed that the shell expands at the speed of light to obtain the most conservative bound while noting the realistic value should be a fraction of this. We see that μ 's with energy \gtrsim TeV will be damped by synchrotron radiation before their decay, while π 's upto \lesssim 10 TeV can run out their lifetime before cooled. Due to their much higher decay rate, on the other hand, decay channel of K 's can manifest unless the energy is \gtrsim 100 TeV.

Without specifying a particular system, we can gain insight into the magnetic environment experienced by high-energy neutrinos near their source by examining the acceleration requirements, decay time scales, and cooling effects. In Section 5.2, our investigation will focus on the magnetic moment effects induced by such environments, aiming to answer the question of "how likely is it for a high-energy neutrino to exhibit such an effect". In this section, we consider a class of the systems obeying the Hillas condition with a large but localized magnetic field, particularly those involving a magnetar as listed below. In Section 5.1.2, we will introduce a simplified model that provides scanning parameters. This model serves the purpose of estimating the probability density function (PDF) of θ_ν as defined in Eq. (5.4) for neutrinos originating from such point sources.

5.1.1 Systems involving a magnetar

Among possible emitters, we consider scenarios where a magnetar is involved. Some candidates are summarised below:

1. Young magnetars tend to bear a rapid, and differential rotation, and possess a strong magnetic with non-trivial multipolar structure. It can therefore be imagined that the spin axis may defer from the magnetic axis. The unipolar induction of a rotating, magnetised NS will render a electric potential, which can possibly reach a magnitude of

$$\Phi_{\max} = \frac{\Omega^2 B_\star R_\star^3}{2c^2} \quad (5.9)$$

in the vicinity of the stellar surface [85]. Here Ω denotes the stellar spin, B_\star sets the magnetic strength, and R_\star is the radius of the NS. The associated electromotive force then accelerates the charge particles that constitute a plasma. For the cases where the

magnetic field \mathbf{B} and the stellar spin $\mathbf{\Omega}$ satisfy the condition $\mathbf{B} \cdot \mathbf{\Omega} < 0$, the positive charge particles will be unleashed along the open field lines in the polar regions [86], including protons [87, 88]. In particular, the injection rate of protons to the stellar wind [89] may be approximated by the Goldreich-Julia rate [90]. Depending on the surface temperature of the pulsar, the relativistic protons are expected to hit photons and generate high-energy neutrinos via Δ -resonance [91, 92],

$$p\gamma \rightarrow \Delta \rightarrow n\pi^+ \rightarrow n\nu_\mu\mu^+ \rightarrow n\nu_\mu e^+ \nu_e \bar{\nu}_\mu, \quad (5.10)$$

whereby protons lose their energy and get “cooled” down (among other cooling mechanisms, e.g., synchrotron and inverse Compton scattering [93, 94]). It should be noted also that the pions and muons in the middle stages will also undergo several cooling effect thus only able to hand over a fraction of the energy to the resulted neutrinos [93] (see also below). The authors of [91, 92] also pointed out that the production site of neutrinos via this effect should be near the stellar surface since the collision angle is less for increasing distance thus higher the required energy of proton’s.

2. Within fireballs [80, 95] that scintillate gamma-ray bursts – both long and short ones – protons and electrons will undergo the Fermi acceleration by the threading magnetic field. If the protons can be sufficiently expedited, proton-photon (p - p) collisions may compose mesons that then decay to produce neutrino transients [96–99] while depending on the properties of fireballs (see, e.g., [100] and the references therein). This p - p collisions mainly lead to pion productions with production other mesons (e.g., kaons) on the side [101, 102]. The majority of pions however does not necessarily imply that they are the main source for neutrinos; the less efficient radiative cooling and the shorter lifetime of kaons arguably make them more important source of neutrinos with a energy larger than TeV [103] (see however below for the charmed mesons). In addition, the proton-photon (p - γ) collisions are also at play for production of photomesons. On top of the process (5.10), kaons may also serve as a proxy for producing high-energy neutrinos through the process [103, 104],

$$p\gamma \rightarrow \Lambda^0 K^+, \Sigma^0 K^+, \Sigma^+ K^0. \quad (5.11)$$

3. At the early stages of millisecond magnetars, ensuing either a binary merger or a supernova, the relativistic wind spewed from the central remnant will be braked by its interaction with ejecta, producing shocks heating up the ponderable medium. Within these pulsar wind nebula, inelastic p - p collisions are expected to effectively operate, giving rise to a copious of mesons [105], e.g., neutral and charged pions [106, 107]. These volatile mesons may, at least in principle, decay to generate high-energy neutrinos after enjoying their temporal lifetime, while no such event has been detected so far [108].
4. The p - p collisions within cocoon systems, formed atop the remnant magnetar of binary merger [109], or of supernova [110], will seed middle stage mesons such as pions and kaons.

The decay of them into highly energetic neutrinos may however be stagnated considerably since the accelerated mesons will be cooled via several mechanism (e.g., [93, 103]) thus dissipating away their energy. Owing to the longer cooling times and shorter lifetime of charmed mesons, therefore, some study speculate that charm contribution to the neutrino population may be more important than expected [90]. Adding to that, the non-production of charm-involve particles is empirically shown to be unlikely [111].

5. On top of the aforementioned proton-involved collision, neutrons in the relativistic outflow may activate production of metastable mesons (e.g., [112]). Such event may be detected in a recent outburst, GRB221009A, from a supernova [113].

Although it is definitely inconclusive that magnetar is an essential engine to power neutrinos to $E_\nu = [0.1, 100]$ PeV, systems harboring a magnetar seem to be tied to production of high energy neutrinos. In this thesis, our main goal is not to investigate one of the listed systems in a realistic manner, which will be too involved given the complexity of modeling the post-merger system and the magnetosphere of pulsars. Instead, we aim to illustrate qualitatively how the flavor ratio of high energy neutrinos will be adjusted by the ν MM effects. To this end, we adopted a simple model for NSs processing a dipolar magnetic field (Sec. 5.1.2), which may approximate to some extent magnetars that are isolated or in a close binary.

5.1.2 Magnetic Field Structure and Numerical Results

In this section, we consider neutrino being produced by a source with a dipolar structured magnetic field. As illustrated in Fig. 5.3, the neutrinos are produced at distance R_{\max} above the source on the dark and light blue shell then propagates along $\vec{\ell}$, where $|\vec{\ell}| = \ell$, towards earth at an angle θ_E relative to the axis of the magnetic field. Therefore, neutrino produced on the upper (lower) shell will be in-going (out-going) with respect to the star. Furthermore, the production site of neutrinos can be projected along the direction of $\vec{\ell}$ on to an plane crossing the stellar center (orange region). The projected point can be expressed through the angle θ_B to an arbitrary reference axis on the plane, and the radius $R_i = R_{\max} \cos \theta_R$ to the stellar center. In other words, R_{\max} determines the maximum value of R_i , and since, in general, the magnetic field strength is larger for smaller R_i , R_{\max} roughly decides the minimal ν MM effect for in-going neutrinos. To summarize, for a certain magnetic field structure, the parameters which determines θ_ν in Eq. (5.4), aside from the ν MM, would be θ_E , θ_B , θ_R and R_{\max} . Furthermore, from the previous section, we learn that high energy neutrinos are typically produced far above the star surface, such as $R_{\max} = 10^4\text{--}10^6$ km, to acquire acceleration as well as to avoid significant cooling effects. Therefore, the R_{\max} and θ_R dependence in B_\perp would be governed by a R^{-3} relation, where R denotes the distance from the center source. On the other hand, the θ_E and θ_B dependence in θ_ν would reflect on the specific magnetic field structure. In the following, we will demonstrate the case for a slowing rotating magnetar, which can be analytically approached.

Additionally, note that for a specific source, θ_E and R_{\max} would, in principle, be fixed, but all possibilities of θ_B and θ_R would still be included. For multiple sources having a similar

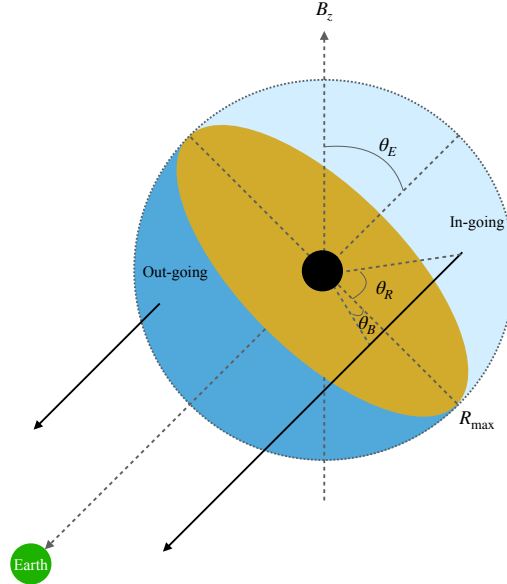


Figure 5.3: Model for single source produced neutrinos. The neutrinos are produced on the shell at distance R_{\max} above the stellar surface, described by θ_B and $R_i = R_{\max} \cos \theta_R$ on the orange plane for both in-going and out-going cases. The magnetic field axis is relative to earth by θ_E .

system, R_{\max} may still be fixed, but θ_E becomes arbitrary in addition to θ_B and θ_R . In the case where multiple systems for multiple sources are included, R_{\max} would also gain arbitrariness. For signatures from diffusive high energy neutrinos, we only consider the latter two cases. Furthermore, we consider neutrinos produced uniformly on the shell in Fig. 5.3, and at each point on the shell, the neutrinos are isotropically emitted. The former assumption, which may describe shock accelerated systems such as the first example in Sec. 5.1.1, leads to θ_R being arbitrary within $(0, \pi/2]$ and θ_B within a full 2π range. Here, $\theta_R \neq 0$, since we consider neutrinos being fully absorbed once it enters the (neutron) star. For systems where neutrinos are not uniformly produced on the shell, one may limit the range of θ_R and θ_B . The angular-distribution of the neutrino emission is sensitive to the collision processes, and it is extremely involved to model the precise procedure. We assume an isotropic emission, i.e., we consider the same amount of in-going and out-going neutrinos. Varying the in-going to out-going ratios could account for the anisotropy of emission.

We take the magnetic field structure for a slowly rotating source where the magnetic energy density is significantly smaller than the gravitational binding energy (e.g., a slowly rotating NS) as an example. In this case, the magnetic field can be treated as perturbations over a spherically-symmetric equilibrium, where the spacetime can be described by the line element,

$$ds^2 = -e^{-2\Phi} dt^2 + e^{2\lambda} dr^2 + r^2 d\theta^2 + r^2 \sin^2 \theta \phi^2, \quad (5.12)$$

in the rest-frame of the star (cf. Fig. 5.3), where Φ is the lapse function and λ is connected to

the mass of the remnant M_\star via

$$e^{-2\lambda} = 1 - \frac{2M_\star}{r} \quad (5.13)$$

outside the star. In fact, NS provide systems aligned with such condition. Denoting the unit vector normal to a space-like hypersphere as n_a , the contravariant, dipolar magnetic field inside a NS can be expressed as [114, 115]

$$B^a \equiv \frac{1}{2} n_c \epsilon^{cabd} F_{bd} = B_\star \left(0, \frac{e^{-\lambda}}{r^2 \sin \theta} \frac{\partial \psi}{\partial \theta}, -\frac{e^{-\lambda}}{r^2 \sin \theta} \frac{\partial \psi}{\partial r}, -\frac{\zeta(\psi) \psi e^{-\Phi}}{r^2 \sin^2 \theta} \right), \quad (5.14)$$

which is associated with the 3-vector

$$\vec{B} = \sqrt{g_{ii}} B^i = \frac{B_\star}{\sin \theta} \left(\frac{1}{r^2} \frac{\partial \psi}{\partial \theta}, -\frac{e^{-\lambda}}{r} \frac{\partial \psi}{\partial r}, -\frac{\zeta(\psi) \psi e^{-\Phi}}{r} \right), \quad (5.15)$$

with γ being the trace of the spatial metric $\gamma_{ab} = g_{ab} + n_a n_b$. Here B_\star sets the canonical strength of magnetic field, R_\star is the radius of the remnant NS, and the stream function ψ for dipolar field has the form [116, 117],

$$\psi = f(r) Y'_{20}(\theta) \sin \theta \quad (5.16)$$

with $f(r)$ being some function to be catered to certain boundary conditions, and Y_{20} being the $\ell = 2, m = 0$ components of spherical harmonics. The exterior part is characterised by the stream function

$$\psi_2(r, \theta) = \frac{3R_\star^3}{8M_\star^3} \left[r^2 \ln \left(\frac{r}{r - 2M_\star} \right) - 2M_\star r - 2M_\star^2 \right] \sin^2 \theta. \quad (5.17)$$

The form admits that the field is force-free and has zero-current on the stellar surface. There remains a function ζ to be determined, which controls the toroidal component of the magnetic field. We consider $\zeta = 0$ for simplicity in this work. In addition, such magnetic field structure indicates that the adiabatic condition, $|\nabla \phi / \phi| \ll \mu B_\perp$, where $\phi = \tan^{-1}(B_x/B_y)$, is met. This is because the self similarity of dipole field lines (in the Newtonian limit, the field strength is $\propto \sin^2 \theta$) gives that the largest field gradient along some unit vector is $|\nabla \phi / \phi|$ scales as r^{-1} . The transverse component, on the other hand, decreases at the third power of radius. Therefore, the ν MM effect will hardly have enough time to ‘feel’ such non-adiabatic evolution before it is weakened to a negligible extent. As a result, $e^{i\phi}$ in Eq. (5.4) can be factored out, leaving no physical influence.

In the considered scenario of Fig. 5.3, the strength of the magnetic field transverse to the neutrinos’ propagation is plotted in Fig. 5.4. Here, $\tilde{\ell} = \ell - R_{\max} \sin \theta_B$, denote a shifted ℓ , such that $\tilde{\ell} = 0$ when the neutrino falls on the orange plane in Fig. 5.3. The structural dependence on θ_E shows the symmetry of a dioplar magnetic field with respect to the pole (B_z in Fig. 5.3), while the dependence on θ_B demonstrates that the antipodal (i.e., θ_B and $\pi - \theta_B$) trajectories undergo patterns that are symmetric about $\tilde{\ell} = 0$. For three canonical θ_E , the dependence of

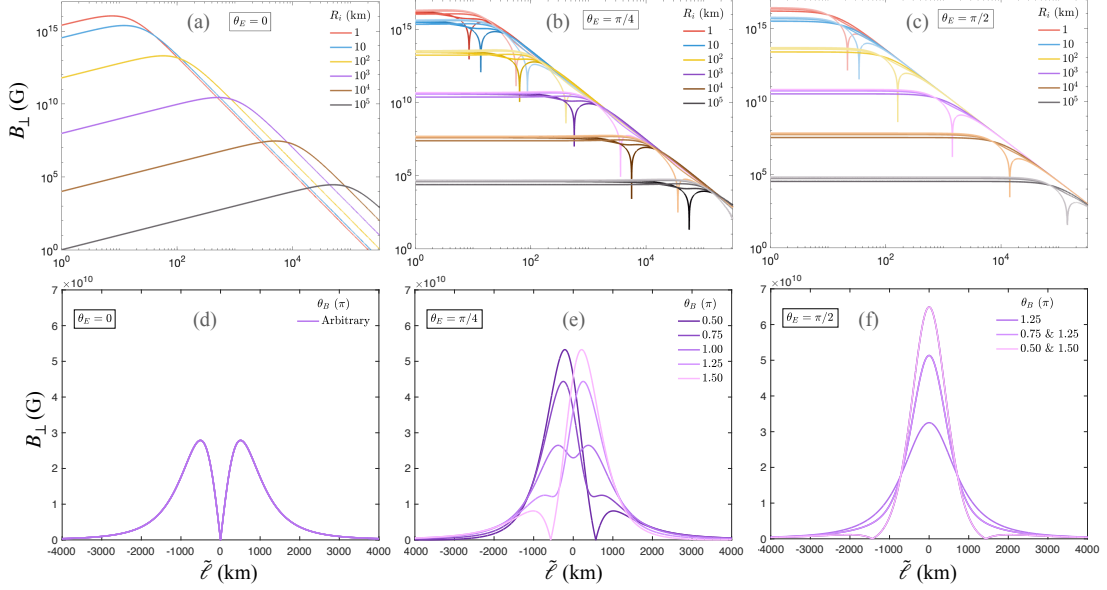


Figure 5.4: The perpendicular component of the magnetic field as a function of $\tilde{\ell}$ for the head-on (left panels) and edge-on (right panels) emissions, and the case in between (middle panels). Here R_{\max} may be arbitrary as long as it is larger than $R_i = R_{\max} \cos \theta_E$. In all plots, different colour tones represent different R_i , while different colour gradient are for different θ_B . We assume $B_\star = 10^{16}$ G and $M_\star = 2.5 M_\odot$.

B_\perp on R_i is observed through different colour patches in the upper panels. When $\theta_E \neq 0$, aside from the dip caused by B being parallel to $\vec{\ell}$, there is no significant change when $\tilde{\ell} \lesssim R_i$, and converges to a line $\propto \ell^{-3}$ once $\tilde{\ell} \gtrsim R_i$. Furthermore, the dependence on θ_B is illustrated in the bottom panels. In all subplots of Fig. 5.4, the color gradation reflects the magnitude of θ_B (the lighter the larger θ_B , as given in the lower panels) for any colour patch.

Fig. 5.5, Fig. 5.6 and Fig. 5.7 show the probability distribution function (PDF) of θ_ν set at a benchmark point: $\mu_\nu = 3.7 \times 10^{-11} \mu_B$. This values is only chosen for the sake for demonstration in this section, and will be varied in the next. In particular, Fig. 5.5 is determined by the magnetic field structure for a slowly rotating magnetar for $R_i = R_{\max} = 10^5$ km. Furthermore, at different $R_i \gtrsim 100$ km, one can adopt the fitting result of scaling:

$$\theta_\nu(\theta_E, \theta_B; R_i) = \theta_\nu(\theta_E, \theta_B; R_i = R_0) \left(\frac{R_i}{R_0} \right)^{-2.0457}. \quad (5.18)$$

This fit has uncertainty $\sigma^2 = 0.0022$, where,

$$\sigma^2 = \frac{1}{N} \sum_{\theta_E, \theta_B; R_i} [\theta_\nu^{\text{num}}(\theta_E, \theta_B; R_i) - \theta_\nu^{\text{fit}}(\theta_E, \theta_B, R_i)]^2, \quad (5.19)$$

$N = 2 \times 10^4$ points, and θ_ν^{fit} denotes Eq. (5.18) for $R_0 = 100$ km while θ_ν^{num} denotes the numerical result for the same θ_E, θ_B, R_i parameters. Therefore, for different $R_i \gtrsim 100$ km, θ_ν in Fig. 5.5

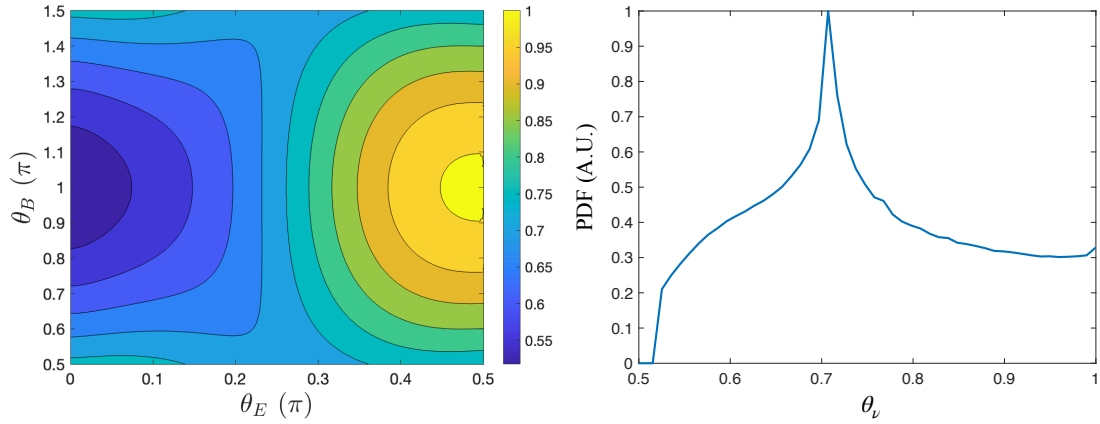


Figure 5.5: Magnetic field structure. The left plot shows the structure of θ_ν when $\mu_\nu = 3.7 \times 10^{-11} \mu_B$ for $R_i = R_{\max} = 10^5$ km. The right plot shows the probability distribution function of each θ_ν when θ_E and θ_B is scanned over within the range from the left plot. At other $R_i \gtrsim 100$ km, θ_ν can be re-scaled according to the fit result in Eq. (5.18).

can be re-scaled according to Eq. (5.18), leaving the structure unchanged. In other words, the magnetic field structure can be described through a dependence θ_E and θ_B as show in the left plot of Fig. 5.5.

In addition, we scan over θ_R for $R_i = R_{\max} \cos \theta_R$ for the in-going contribution in Fig. 5.6. The grey lines denote the case for a fixed R_{\max} , as labeled on the plot, while the red line demonstrates a scan over $10^4 \leq R_{\max} \leq 10^6$ km. Note that since θ_ν includes an integration over ℓ , the expectation value $\langle \theta_\nu \rangle \propto R_{\max}^{-2}$, and the distributions are also shifted accordingly. Finally, Fig. 5.7 demonstrates the full scan of parameters by considering the out-going (blue line) contributions in addition to the in-going ones given in Fig. 5.6. Since B_\perp converges to a value $\propto \tilde{\ell}^{-3}$ when $\tilde{\ell} \gtrsim R_i$, as show in Fig. 5.4, the out-going neutrinos would have

$$\theta_\nu \simeq \mu_\nu B_\perp^{\text{shell}} \int_{R_{\max}}^{\infty} dr \left(\frac{r}{R_{\max}} \right)^{-3} = \frac{1}{2} \mu_\nu \times B_\perp^{\text{shell}} \times R_{\max}, \quad (5.20)$$

when the neutrino is produced on a certain point on the shell of some R_{\max} , on which $B_\perp = B_\perp^{\text{shell}}$. In this case, the scan over the shell would be equivalent to scanning over θ_E and θ_B , therefore, the distribution shown in Fig. 5.5 would inherit the shape in Fig. 5.7 for out-going neutrinos.

5.2 Neutrino Magnetic Moment Effect

The Hillas condition in Eq. (5.5) provides a $B \times R$ condition for the production of high energy neutrinos. At the same time, the $B \times R_{\max}$ value would also determine the expectation value of θ_ν , explicitly though Eq. (5.20) for out-going neutrinos, and also for in-going neutrinos, as shown in Fig. 5.7. Since R_{\max} represents the height at which the neutrinos are produced, it

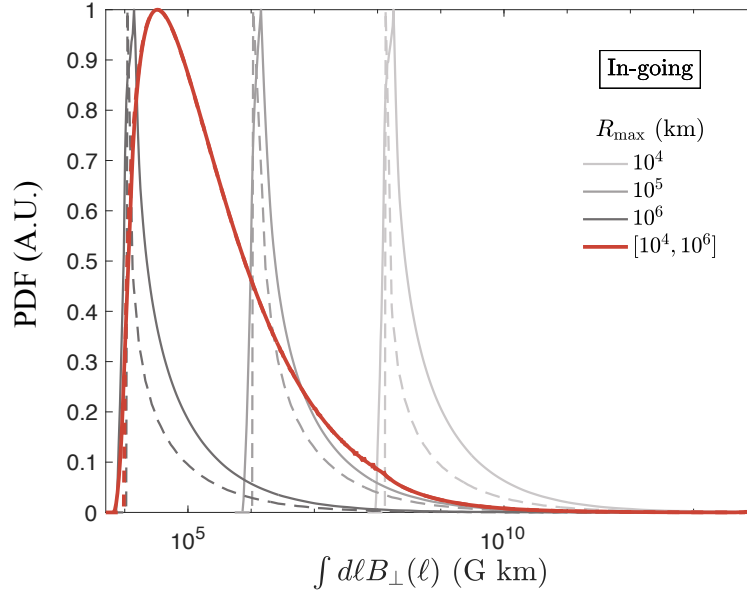


Figure 5.6: Same as Fig. 5.5 but also scanning θ_R for certain R_{\max} for in-going neutrinos. The solid lines are for when θ_E and θ_B are also scanned over, while the dashed lines is when $\theta_\nu(\theta_E, \theta_B, R_i = 10^5 \text{ km})$ is fixed to the mean value in Fig. 5.5 at 0.75.

would roughly coincide with the comoving length of where the protons accelerate in, namely, R . In addition to the acceleration (Hillas) condition, there are other factors influencing the νMM effect. Incorporating cooling limits as well as specific systems, we include lines where the νMM effect is optimized in Fig. 5.8. These lines, which denotes the value of μ_ν such that $\theta_\nu(\mu_\nu^{\text{opt}}) = \pi/2$, where

$$\theta_\nu \sim \frac{\pi}{2} \left(\frac{\mu_\nu}{3 \times 10^{-12} \mu_B} \right) \left(\frac{B}{5 \times 10^5 G} \right) \left(\frac{R}{10^5 \text{ km}} \right), \quad (5.21)$$

would overlap with the acceleration lines.

Nonetheless, the value of μ_ν only shows when $\theta_\nu = \pi/2$ for the case where the magnetic field is uniformly distributed over a distance R , or when $\theta_\nu = \pi/4$ for the out-going case a specific θ_E and θ_B in Fig. 5.8. For a single source with a dipolar magnetic field structure, a scan of parameters, leading to a PDF such as Fig. 5.7, is necessary according to the previous section. In fact, with the distribution in Fig. 5.7, we have plotted the PDF of θ_ν for different values of μ_ν in the left plots of Fig. 5.9. The darker purple lines correspond to the values labeled on the Hillas plot, for instance, when $R_{\max} = 10^5 \text{ km}$, $\langle B^{\text{shell}} \rangle = 0.75 \times 3.6 \times 10^5 \text{ G}$, this correspond to the red dot in Fig. 5.8 where $\mu_\nu = 3 \times 10^{12} \mu_B$ would result in $\theta_\nu = \pi/2$ according to Eq. (5.21). Since θ_ν results in an oscillation phase in Eq. (5.4), we plot the PDF of the remainder of θ_ν divided by 2π , denoted as $\theta_{\nu, \text{eff}}$ in Fig. 5.9. From plot (a), we can see that $4.5 \times$ the point on the Hillas plot ($\mu_\nu = 1.0 \times 10^{11} \mu_B$) results in the PDF to peak at $\theta_\nu = \pi/2$. However, we can also see that the

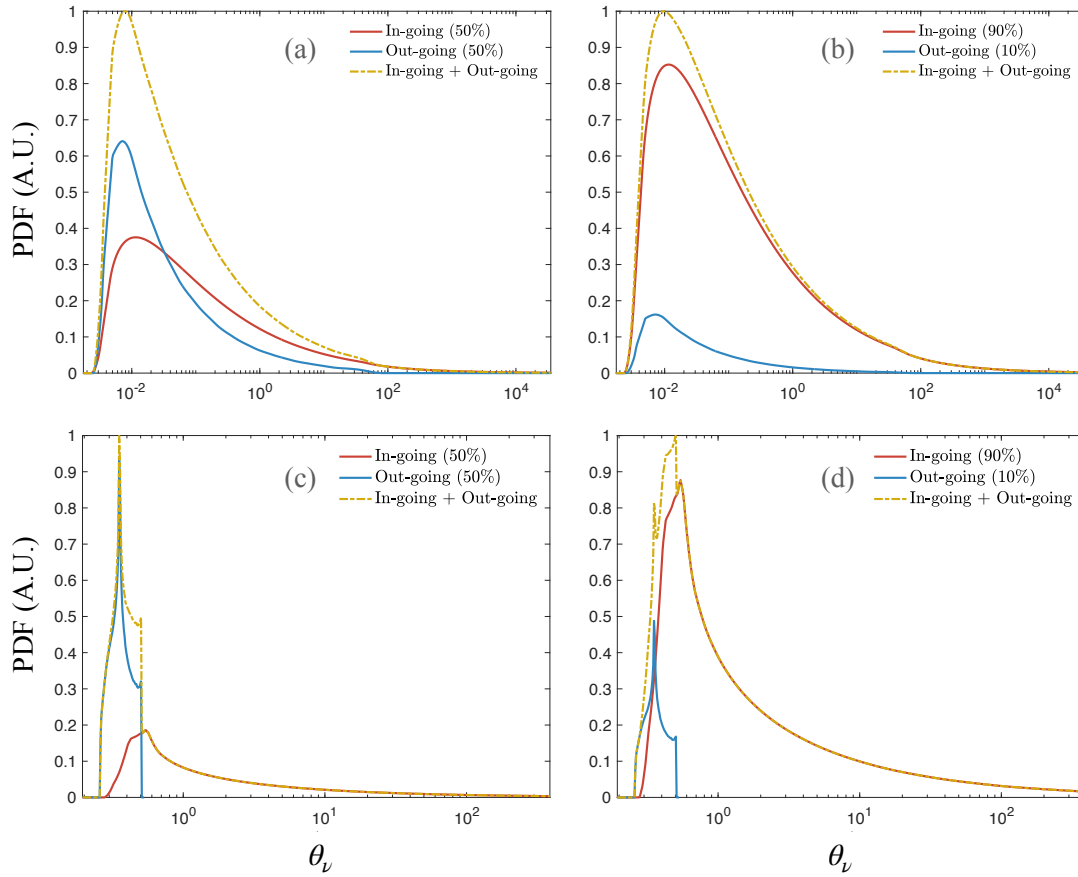


Figure 5.7: The red lines in the upper plots correspond to the red line in Fig. 5.6. The red lines in the lower plot correspond to the solid grey lines in Fig. 5.6. The blue lines show the distribution from out-going neutrinos, which inherit the shape from the distribution in Fig. 5.5.

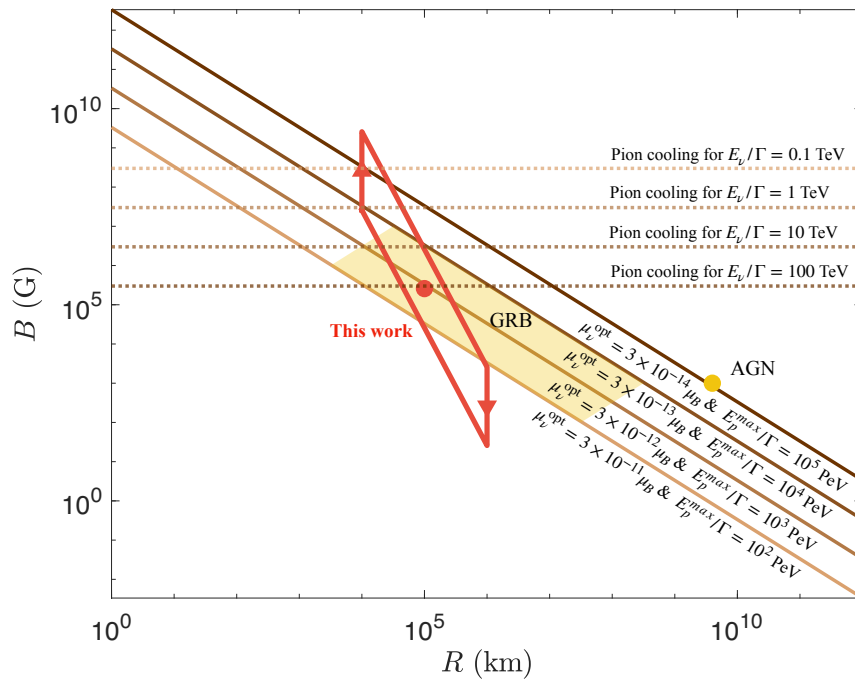


Figure 5.8: Hillas plot. the solid lines are from Eq. (5.5) and 5.21 such that $\theta_\nu = \pi/2$. The dashed lines represent the minimal magnetic field of which neutrinos above 100 TeV from pion decay, as well as the secondary muon decay, would start to suffer from a significant cooling effect. The yellow regions show two of the typical candidates for producing high energy neutrinos, namely, point sources accompanied by a gamma ray burst (GRB) and the active galactic nuclei (AGN). The red points are region correspond region considered in this section.

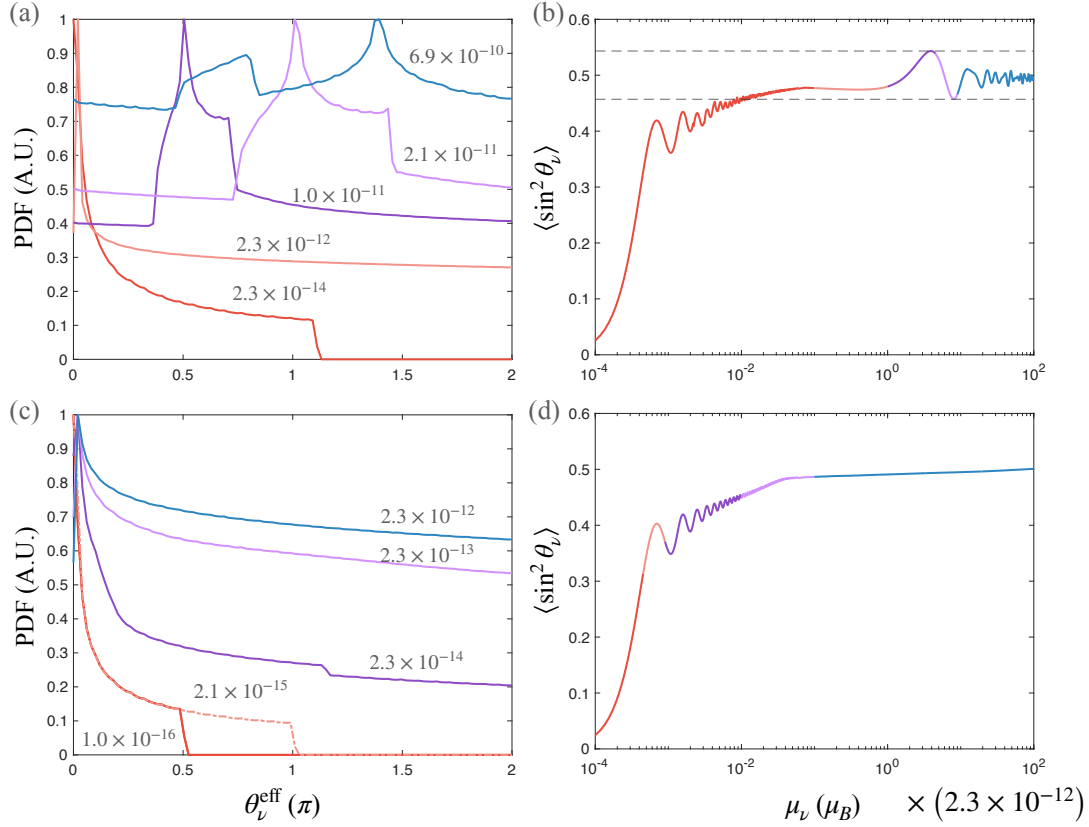


Figure 5.9: The upper plots are for R_{\max} fixed at 10^5 km (the case for plot (c) in Fig. 5.7). The lower plots scan over $10^4 \leq R_{\max} \leq 10^6$ km (the case for plot (a) in Fig. 5.7). The labels for different colored lines represent μ_ν in ν_B in the left plots. The right plot takes Eq. (5.4) into consideration, showing the probability of obtaining an helicity flip from ν MM effect.

probability of having other values of θ_ν are all non-zero once $\mu_\nu \geq 2.3 \times 10^{-12} \mu_B$ (i.e., the red dot on Fig. 5.8 for $\theta_\nu = 1$). This is due to the in-going contribution in Fig. 5.7 where θ_ν would cause a rapid oscillation at large values. Therefore, taken into account that the in-going and out-going each contributes 50%, the ν MM we can probe may be two orders of magnitude smaller than what we have expected from the Hillas plot. However, for this same reason, the probability of having an helicity flip would not reach the optimal value: $\sin^2(\pi/2) = 1$ but it saturates to 0.5 instead. This feature is shown in plot (b) where the red region is non-zero because of the in-going contributions, and the purple and blue region saturates to 0.5. As expected, such smearing phenomenon is even more pronounced when a range of R_{\max} is taken into account, as we can see from the plot (d) in Fig. 5.9. In fact, this would imply that although we have assumed the magnetic field structure of a slowly rotating NS, the resulting probability of helicity flip due to ν MM would not be sensitive to such structure once various values of R_{\max} are considered.

5.2.1 Signatures at IceCube

Finally, in Fig. 5.10–5.12, we show how the ν MM would affect the flavour and/or helicity ratio for five types of initial state ($\nu_e : \nu_\mu : \nu_\tau : \bar{\nu}_e : \bar{\nu}_\mu : \bar{\nu}_\tau$):

- pp (blue, dashed): Neutrinos are produced through $p - p$ collision followed by pion decay and muon decay. The initial state would be (1:2:0:1:2:0).
- $p\gamma$ (blue): Neutrinos are produced through $p - \gamma$ collision followed by pion decay and muon decay. The initial state would be (1:1:0:0:1:0).
- pp -damped (green, dashed): Neutrinos are produced through $p - p$ collision followed by pion decay, but the cooling time scale is smaller than the muon decay time scale, resulting in neutrinos from muon decay having energy smaller 100 TeV. The initial state would be (0:1:0:0:1:0).
- $p\gamma$ -damped (green): Neutrinos are produced through $p - \gamma$ collision followed by pion decay, but the cooling time scale is smaller than the muon decay time scale, resulting in neutrinos from muon decay having energy smaller 100 TeV. The initial state would be (0:1:0:0:0:0). This scenario has currently been disfavoured the Glashow resonance event observed at IceCube []. In this work we show that such observation can be explained by ν MM effect, as shown in Fig. 5.10.
- n (purple): Neutrinos are produced through neutron decay, which would, in general, be produced at a lower energy compared to the above cases. However, it barely suffers from cooling effects. The initial state would be (0:0:0:1:0:0). This scenario has currently been disfavoured at a 90% confidence level by the flavour ratio observed at IceCube [118]. In this work we show that such observation can be explained by ν MM effect, as shown in Fig. 5.12 and Fig. 5.11.

In fact, from Fig. 5.11 and Fig. 5.12, we can see the flavour ratio being pulled to the center as μ_ν increase as a rule, while having some dependence on the ν MM's mixing matrix (or flavour structure) shown in Fig. 2.1. Note that the $p\gamma$ -damped scenario is particularly motivated for high energy neutrino as listed in Sec. 5.1.1, because not only would it involve processes such as the Δ -resonance in Eq. (5.10), it is also in a strong magnetic field environment which cause muons to be damped. However, without helicity flip, no electron anti-neutrino is expected for observation at earth, hence, the even observing one Glashow resonance event would disfavor this scenario. Therefore, the explaining the detected Glashow resonance event is particularly motivated. To sum up, the flavour ratio and Glashow resonance detection has been used to trace back the initial state (and hence the production mechanism) of the neutrinos [119]. However, we have shown that the ν MM effect should also be taken into account if the neutrino has a Majorana nature, since 1) it overlaps with the Hillas condition as shown in Fig. 5.8 2) the non-zero neutrino mass indicates a non-zero μ_ν .

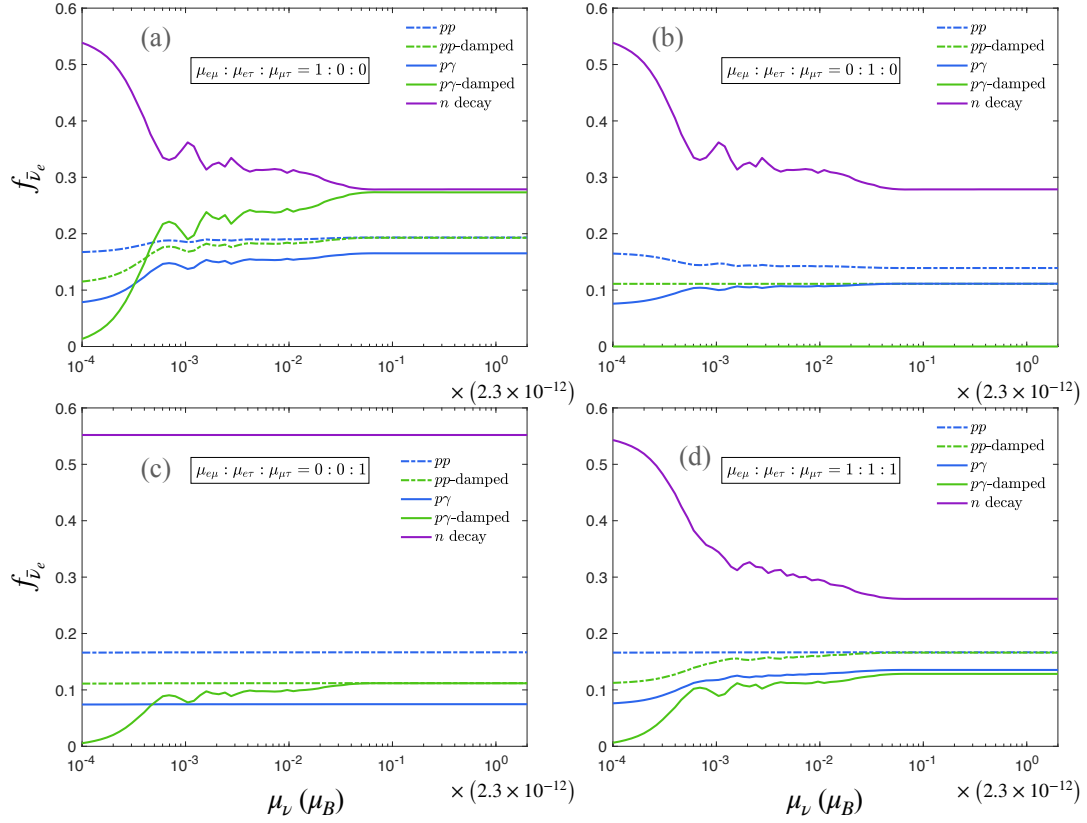


Figure 5.10: The fraction of anti-electron neutrino relevant for detection through Glashow resonance. Plots (a)-(d) show case for different mixing matrix of ν MM demonstrated in Fig. 2.1. The different colored lines represent different initial states for different production processes listed in the text.

As for the theoretic interest in particle physics, of determining the value of μ_ν , mixing matrix \tilde{U} in Eq. (5.2) and the Dirac/Majorona nature of the neutrinos, we also look at Fig. 5.10-5.12. Following the previous discussion, if the high energy neutrinos are generated through a $p\gamma$ -damped process, then the observation of one Glashow resonance event already point towards neutrinos having a Majorona nature with $\mu_\nu \gtrsim \mathcal{O}(10^{-15})$ with $\mu_{e\mu} \neq 0$ and/or $\mu_{e\tau} \neq 0$ for the mixing matrix. Similar argument may be applied for different initial states as well as for the flavour triangles in Fig. 5.11 and 5.12. However, the $p\gamma$ -damped case would be the best channel for Glashow resonance detection since zero events are expected when $\mu_\nu = 0$ or when only $\mu_{\mu\tau}$ is non-trivial. Similarly, for a positive signature, the n -decay be the best channel for the flavour rations, since a nontrivial ν MM effect would pull the ratio towards the middle. On the other hand, if future observation, such as IceCube Gen2, show a significant asymmetry among flavors and/or helicity, it would indicate that neutrinos either have a Dirac nature or set a bound on μ_ν and \tilde{U} for the Majorona neutrinos.

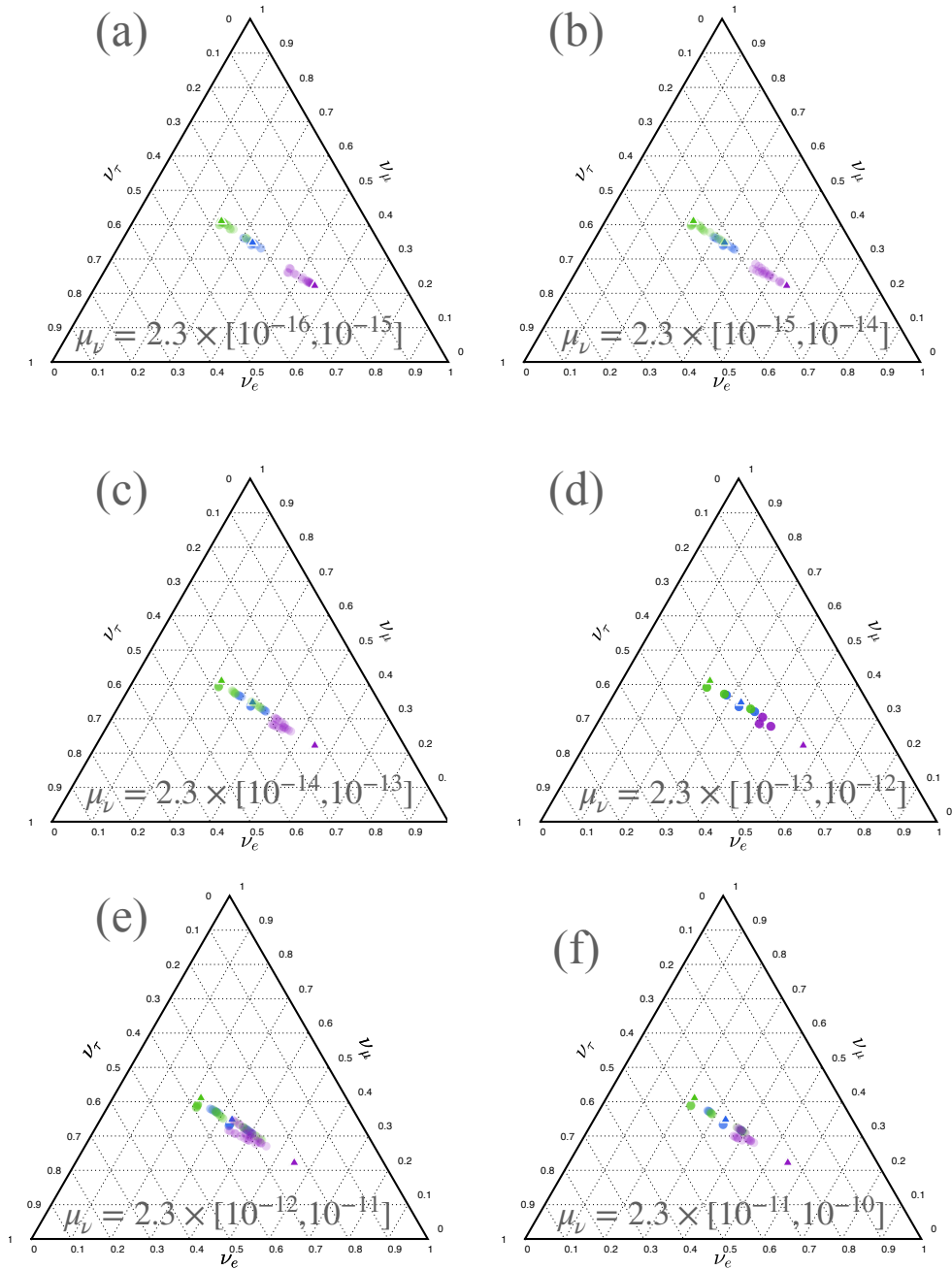


Figure 5.11: The flavour ratio for different ranges of μ_ν for neutrinos produced at the red dot in Fig. 5.8 and magnetic field structure modeled in Sec. 5.1.2. This corresponds to plot (a) and (b) in Fig. 5.9. The ν MM mixing matrix include all four benchmark points listed in Fig. 5.10.

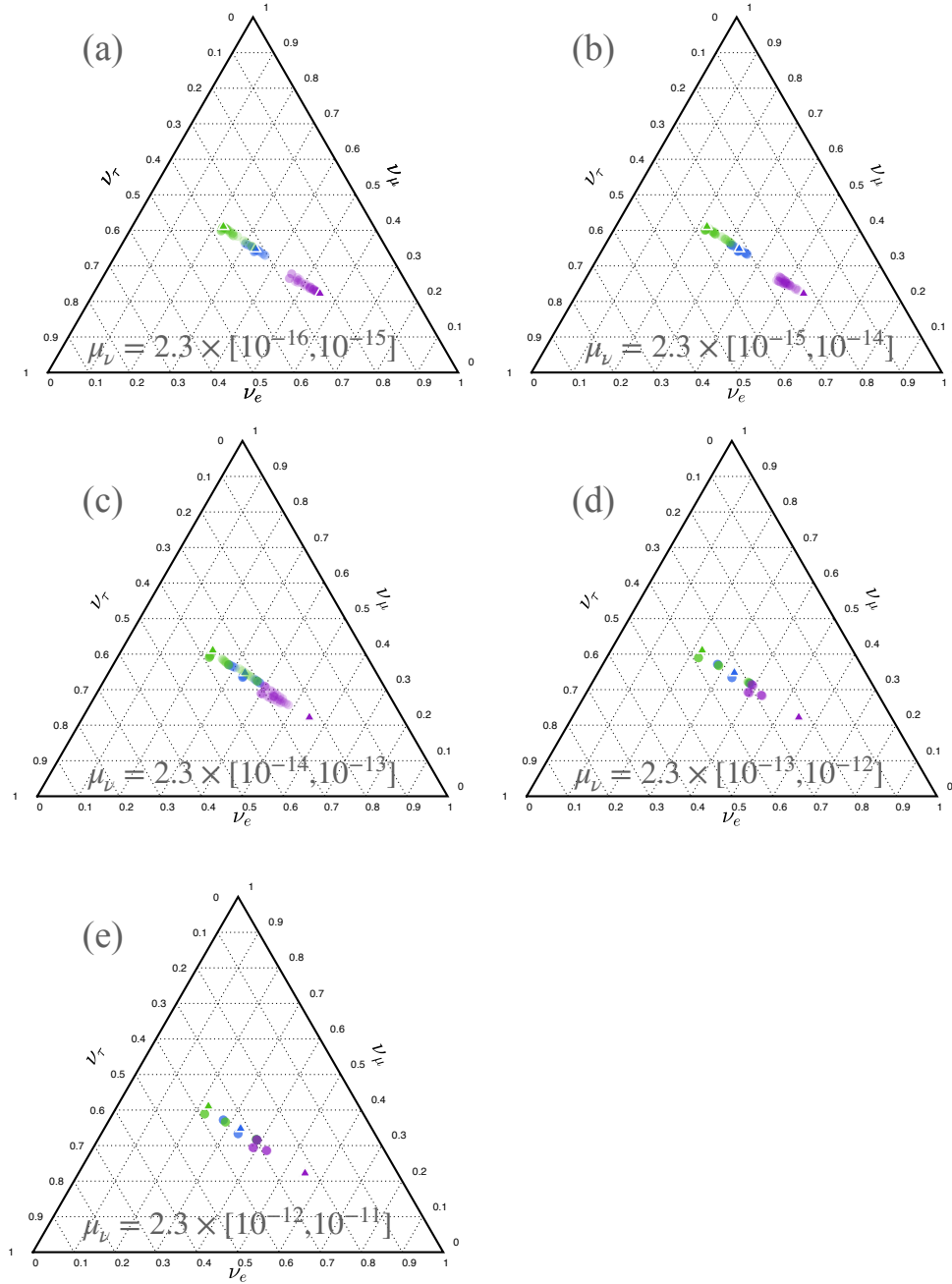


Figure 5.12: The flavour ratio for different ranges of μ_ν for neutrinos produced at the region circled by the red line in Fig. 5.8, and magnetic field structure modeled in Sec. 5.1.2. This corresponds to plot (c) and (d) in Fig. 5.9. The ν MM mixing matrix include all four benchmark points listed in Fig. 5.10.

Chapter 6

Conclusions

The unique properties of neutrinos make them an exceptional portal to quantum effects. In this thesis, we have explored how quantum effects may leave imprints on neutrino decoherence signatures in terrestrial experiments, and how specific coherence effects of high-energy neutrinos from astrophysical environments can be observed. The relevant quantum coherence and decoherence framework is outlined in Chapter 2. Coherent effects of neutrinos, including neutrino oscillations and those resulting from interactions with low momentum transfer, are described by a closed quantum system in Section 2.1, where coherence is fully preserved. However, all observable effects of mixed quantum states, coherence is expected to be lost at some point. This leads us to Section 2.2, where an open quantum system is considered and incorporated into a Quantum Field Theory framework.

Thanks to the increasing precision of neutrino oscillation experiments, the study of neutrino decoherence effects may become feasible in future experiments, opening up a new avenue for probing new physics. In Chapter 3, we introduce the "layer structure" (illustrated in Fig. 3.1), which incorporates the concept of an open quantum system and classical statistics while maintaining Quantum Field Theory as the fundamental theory. This structure is particularly useful for understanding mechanisms behind decoherence signatures in neutrino oscillation experiments. We demonstrate that decoherence effects arise from distributions that characterize uncertainties, referred to as "weighting functions" at each layer. At the quantum level (layer 1), the sources of these weighting functions are categorized into two groups: those carried by external on-shell particles, such as the lifetimes of these particles, and those originating from internal off-shell processes, such as loop effects. To quantify the decoherence effect as a parameter, we consider the widths of these distributions. Consequently, external uncertainties are combined and parameterized as σ_p , representing the uncertainty arising from the wavepacket sizes of external particles. Internal uncertainties are parameterized as σ_x , accounting for coordinate uncertainties around the vertices. Since the uncertainty distributions are rearranged on the Wigner-PS, so will the uncertainty parameters. On the other hand, classical uncertainties

resulting from a lack of knowledge also contribute to decoherence signatures. These uncertainties include factors such as the production profile of neutrinos, energy resolution, and errors in the energy reconstruction model. Similar to the weighting functions in layer one, we can also parametrize these distributions based on their width. In this context, production profile dominates the uncertainty parameter σ_L while the energy resolution, and errors in the energy reconstruction model are included in σ_E .

In Section 4.1, we show that decoherence effects from all the uncertainty distributions (or uncertainty parameters) come from phase wash-out effects, which are determined by a phase structure and some distribution. For each uncertainty parameter, there is a certain phase structure and some localized distribution with width as the corresponding parameter, resulting in a phase wash-out effect suppressing and/or causing a phase shift in the oscillation signature. The phase structure also characterises dependence on the traveling distance (L_0) and energy spectrum (E_0) for each uncertainty parameter, hence, enables us to identify the mechanisms behind decoherence signatures by analysing these parameters in the neutrino detection profile and/or spectrum. The phase structures are given in Eq. (4.17) and Eq. (3.30) (Eq. (4.23) and Eq. (3.33)) for uncertainties on the Wigner phase space and the relativistic phase space, respectively, for the time dependent (independent) case. Furthermore, we have classified neutrino decoherence in terms of its mechanism as state decoherence and phase decoherence. The former represents the separation of superposition (mass) states, and is dominated by quantum uncertainties; while the latter indicate averaging effect due to the information loss, and is mainly decided by macroscopic classical uncertainties. In particular, we calculate the case of Gaussian distributed weighting functions and estimate how much more statistics we need for certain $\sigma_{\bar{p}}$, σ_L and σ_E , to be sensitive to them at 90% CL in Fig. 4.7, by taking the RENO experiment as a benchmark in Section 4.2. In addition, the requirement of systematic uncertainties can be seen by whether we will be able to identify decoherence signatures between quantum uncertainties and classical uncertainties. For instance, in recent literature [120, 121], it has been shown that quantum decoherence from WP separation cannot be observed for reactor neutrinos since the damping factor approximately have the same L and E dependence for that from the energy resolution within current the baselines. Therefore, as they have estimated that the WP size from the uncertainties of the nuclear fission are orders of magnitude larger than that required to be able to compete with the energy resolution, they reach the non-observational conclusion. In our framework, this result would translate to: the decoherence scale from nuclear fission would not result in a signature distinguishable to σ_E (energy resolution) within the range (in terms of L_0 and E_0) of interest.

Furthermore, we propose a novel method in Section 4.3, the phase measuring method, to measure the asymmetry of weighting functions by searching an oscillation minimum. Particularly, we estimate the sensitivity of this method for a two-Gaussian distributed, $D_{\bar{p}}$ -induced, quantum mechanical uncertainty as well as the statistical uncertainty from the energy resolution in Fig. 4.10. While the energy resolution ranges typically from $1 - 10\%/\sqrt{E_0}(\sqrt{\text{MeV}})$ for neutrino detectors, the asymmetry parameter a , could be caused by the quantum effect of having

a superposition of different processes. For instance, having simultaneously quasi-elastic scatterings and inelastic scatterings for neutrinos scattering on nucleons, or by nuclear effects such as the Fermi motion [122]. In fact, quantitative estimation of the asymmetry parameter would need further investigation. To sum up, while the four uncertainty parameters σ_x , σ_p , σ_L and σ_E in our structure can be determined by some theoretical mechanisms, such as the wavepacket size of the external particles, the type of collisions, matter effect, exotic effects like space-time fluctuation, etc; it could also be potentially measured experimentally through rate or phase measuring methods. Our considerations presented here provide the theoretical background for such analyses and can be applied to any experiment. Experimental improvements are necessary, for instance via better energy resolution or larger event numbers, or by other detection techniques made possible by e.g. developments in coherent elastic neutrino-nucleus scattering.

Taking advantage of the extreme magnetic field environment required to accelerate particles, we study the coherence effect from neutrino magnetic moment (ν MM) of high energy neutrinos in Chapter 5. The Hillas condition, as expressed in Eq. 5.5, indicates the magnetic field environment necessary for the acceleration of protons. These accelerated protons subsequently participate in proton-proton or proton-photon collisions, ultimately giving rise to the production of neutrinos. Such condition would roughly overlap with the ν MM effect in the Hillas plot as shown in Fig. 5.8. For a more detailed analysis, we constructed a model illustrated in Fig. 5.3. This model incorporates various parameters, including R_{\max} , which specifies the distance relative to the star's surface where neutrinos are generated, and θ_E representing the relative position of Earth. These two parameters together with θ_B determines the trajectory of neutrinos' across the magnetic field. Additionally, varying in-going to out-going ratio accounts for the configuration of neutrino production; for the considered simple model, we assume an isotropic production of neutrinos (i.e., in-going to out-going ratio is unity). For the ν MM effect, the crucial parameter is R_{\max} , which is restricted by the Hillas condition and the cooling effects shown in Fig. 5.2. We computed the anticipated flavor ratio (Fig. 5.12) and the anti-electron neutrino fraction (Fig. 5.10) for a variety of ν MM values for diffusive neutrinos originating from gamma-ray-burst sources by scanning over the aforementioned parameters within the framework of an analytical dipolar magnetic field structure.

Appendix A

Fourier Transformation and Convolution Properties

We review some useful properties of Fourier transformation (FT) and convolution in this section. These properties are particularly useful in our structure, for the layer moving operators involve integrations of complex functions, which can be parameterized as a plane wave term $\exp(i\eta(x, p))$ and a normalized-real probability density function (PDF) term. In particular, we will show how the layer variables are connected with each other via FT properties, how two sources of uncertainties are combined to an effective one with convolutional properties, and demonstrate the phase washout effect. Below, we will outline the properties in bold front followed by a more detailed demonstration.

- **Property 1: The FT of an even function is real, while that of an odd function is purely imaginary.** For an even function $f(x)$,

$$\begin{aligned} \int_{-\infty}^{\infty} dx e^{-ipx} f(x) &= \frac{1}{2} \int_{-\infty}^{\infty} dx e^{-ipx} \{f(x) + f(-x)\} \\ &= \frac{1}{2} \int_{-\infty}^{\infty} dx e^{-ipx} f(x) - \frac{1}{2} \int_{-\infty}^{\infty} dx e^{ipx} f(x) = \int_{-\infty}^{\infty} dx f(x) \cos(px) \in \mathbb{R}, \end{aligned} \quad (\text{A.1})$$

and similarly for odd functions being imaginary after Fourier transformation.

- **Property 2: For any probability density function (PDF), $W(x; L)$, the FT can be written as**

$$P(L, p) = \int_{-\infty}^{\infty} dx e^{-ipx} W(x; L) = e^{-ipL} \tilde{W}(p) \equiv e^{-i(pL - \beta(p))} |\tilde{W}(p)|, \quad (\text{A.2})$$

where the damping term $|\tilde{W}(p)| \leq \tilde{W}(0) = 1$ and the phase shift term $\beta(p)$ is non-zero and non- π only when $W(x; L)$ is symmetric w.r.t. L . If the shape of $W(x)$ is symmetric, $W(x + L)$ would be even for $L = \int dx x W(x)$. Then, after shifting

$x \rightarrow x + L$, we obtain Eq. (A.2) with $\tilde{W}(p) \in \mathbb{R}$ and no phase shift, i.e. $\beta = 0$. On the other hand, if the shape of $W(x)$ is not symmetric, we can always write it in terms of an even function and an odd function, i.e. $W(x + L) = W_{\text{even}}(x + L) + W_{\text{odd}}(x + L)$. Hence on top of the even part, which is treated in the same manner as the symmetric case, the odd part would give rise to an imaginary part in $\tilde{W}(p)$, or in terms of rotation coordinate, a phase shift $\beta(p) \neq 0$ and π relative to the oscillation phase, pL , on the next layer. Moreover, $W(x)$ being a PDF indicates that $\int dx W(x) = 1$, and $W(x) \geq 0$, therefore, $|\tilde{W}(p)| \leq \int dx W(x) = \tilde{W}(0) = 1$. A list of examples is given in Table 4.3, showing how the asymmetry of the PDF induces a non-zero and non- π phase shift. Additionally, it is also clear from the plots that, in most cases, the larger the width (labeled as σ_n , for $n = \{p, L, E\}$) is for the PDF, the smaller will the width of $\tilde{W}(p)$ be. Henceforward, since $|\tilde{W}(p)| \leq \tilde{W}(0) = 1$, the larger σ_n is, the smaller $|\tilde{W}(p)|$ will be, for some $p \neq 0$, and the more suppressed $P(L, p)$ will be. Another way to look at this effect is that a wider width of the PDF indicates that there is a wider range for e^{ipx} to be averaged out upon the integration over x , namely, the PWO effect.

- **Property 3: The PWO effect is the generic case of Eq. (A.2), for a complex function $\Gamma(x; L) \equiv |\Gamma(x; L)|e^{i\eta(x)}$, and Eq. (A.2) is simply when $\eta(x)$ is linear in x .** The PWO effect is written as

$$\frac{\int dx \Gamma(x; L)}{\int dx |\Gamma(x; L)|} = e^{i(\eta(x)|_{x=L-\beta})} \Phi(L), \quad (\text{A.3})$$

where L is the central value of $\Gamma(x)$, such that $\Gamma_{\text{even}}(x + L)$ is even. In fact, according to the layer structure presented in the main text, L would also be the next level PS variable in our structure corresponding to x . Hence, similar to property 2, $|\Phi| \leq 1$ and β is non-zero only when $\Gamma(x; L)$ is symmetric w.r.t. L . In fact, this is why we call Φ the damping term and β the phase shift term in this paper. Moreover, the wider $\Gamma(x)$ is relative to the wavelength for the phase structure $\eta(x)$, the smaller will Φ become.

- **Property 4: For two distributions $f(x)$ and $g(x)$ with width σ_f and σ_g , respectively, the width of $(f * g)(L)$, σ_{f*g} is larger than either σ_f or σ_g , where “*” represents the convolution of two distributions.** Whenever two function are related with the form

$$\int dx f(x)g(x - L) \equiv (f * g)(L), \quad (\text{A.4})$$

there is a convolution between these two functions. This usually occurs when there are multiple sources of uncertainties taken into consideration, for instance, the total uncertainties of the PS variables from both the initial state and the final state (Eq. (2.32)), the production site and the detection site (Eq. (2.39)), or the external process and the internal process (Eq. (2.53)). The width of an arbitrary localized function $f(x)$ is defined here as

$$\sigma_f = \frac{1}{2\sqrt{\pi}} \int dx |f'(x)|, \quad (\text{A.5})$$

where $f'(x)$ is the normalized function of $f(x)$, and $f'(x) = f(x)/\max\{|f(x)|\}$, such that its global maximum is unitary. Also, $1/2\sqrt{\pi}$ is inserted such that width of a Gaussian distributed function would have the width at one standard deviation and the other distributions are then defined accordingly. On the other hand, the width of the product of two function, σ_{fg} , will be smaller than the individual widths of the functions σ_f and σ_g , since

$$\begin{aligned} 4\pi\sigma_{fg} &= \int dx |f'(x)g'(x)| \leq \int dx |f'(x)||g'(x)| \\ &\leq \int dx |f'(x)| = 2\sqrt{\pi}\sigma_f \text{ and } \int dx |g'(x)| = 2\sqrt{\pi}\sigma_g, \end{aligned} \quad (\text{A.6})$$

for $|f'(x)| \leq 1$ and $|g'(x)| \leq 1$. Moreover, by the convolution theorem,

$$f * g = \mathcal{FT}^{-1}[\mathcal{FT}(f)\mathcal{FT}(g)], \quad (\text{A.7})$$

we can see that comparing to the trivial case where g is a delta function, and we have $f = \mathcal{FT}^{-1}[\mathcal{FT}(f)]$, the width of $\mathcal{FT}(f)\mathcal{FT}(g)$ would decrease when the width of g is no longer zero, and hence σ_{f*g} would increase. For example, if $f(x)$ and $g(x)$ are Gaussian distributions, then $\sigma_{f*g}^2 = \sigma_f^2 + \sigma_g^2$.

- **Property 5: Convolution of a complex function, $h(x) = f(x)e^{ipx}$, and a real function, $g(x)$, is**

$$(h * g)(y) = \int e^{ip'y} \tilde{f}(p' - p) \tilde{g}(p') \equiv e^{ipY(y)} I_1(y) I_2(p), \quad (\text{A.8})$$

where $\tilde{f} = \mathcal{FT}[f]$, $\tilde{g} = \mathcal{FT}[g]$ and the width of $I(y) \in \mathbb{R}$ is the same as that of $(f * g)(y)$.

By the convolution theorem,

$$\mathcal{FT}[h * g] = \mathcal{FT}[h]\mathcal{FT}[g] = \int dx f(x)e^{-i(p'-p)x} \int dx g(x)e^{-ip'x} = \tilde{f}(p' - p)\tilde{g}(p'). \quad (\text{A.9})$$

Then by doing an inverse Fourier transformation from p' to y on Eq. (A.9), we arrive at Eq. (A.8). Furthermore, the width of the product of two functions, $\tilde{f}(p' - p)\tilde{g}(p')$ is independent of the parallel shift from p , i.e. the width of $\tilde{f}(p' - p)\tilde{g}(p')$ is the same as $\tilde{f}(p')\tilde{g}(p')$, which is the case where the convolution is between f and g . For example, if $f(x)$ and $g(x)$ are Gaussian distributed, i.e.

$$f(x) = \exp\left[\frac{-(x - \mu_f)^2}{4\sigma_f}\right], \quad g(x) = \exp\left[\frac{-(x - \mu_g)^2}{4\sigma_g}\right], \quad (\text{A.10})$$

Type (notation for σ_h)	Function relation	Width relation	Gaussian case
FT type ($\bar{\sigma}_f$)	$h = \mathcal{FT}(f)$	NC	$\sigma_h = \frac{1}{2\sigma_f}$
Product type (σ_{fg})	$h = f \times g$	PC, $\sigma_h < \{\sigma_f, \sigma_g\}$	$\frac{1}{\sigma_h^2} = \frac{1}{\sigma_f^2} + \frac{1}{\sigma_g^2}$
Convolution type I (σ_{f*g})	$h = f * g$	PC, $\sigma_h > \{\sigma_f, \sigma_g\}$	$\sigma_h^2 = \sigma_f^2 + \sigma_g^2$

Table A.1: Properties of the width of the function h in terms of the original real function(s) f (and g). Here NC/PC means that σ_h is negatively/positively correlated to σ_f (and σ_g).

Function (width notation), Type	Width relation	Gaussian case
$H(y)$ (σ_H), Convolution type I	PC, $\sigma_H > \{\sigma_f, \sigma_g\}$	$\sigma_H = \sigma_{f*g}$
$I(p)$ (σ_I), Convolution type II	NC	$\sigma_I = 1/\sigma_{fg}$

Table A.2: Properties of the width of functions H and I for convolution with an additional complex phase in terms of their origin functions f and g , giving rise to an additional term $I(p)$.

then $\tilde{f}(p') = \exp(-ip'\mu_f - p'^2\sigma_f^2)$, $\tilde{g}(p') = \exp(-ip'\mu_g - p'^2\sigma_g^2)$, and

$$\tilde{f}(p' - p)\tilde{g}(p') = e^{-ip'(\mu_f + \mu_g)} \exp\left[-(\sigma_f^2 + \sigma_g^2)\left(p' - \frac{p}{\Delta}\right)^2 - \sigma_f^2 p^2 \left(1 - \frac{1}{\Delta}\right)\right], \quad (\text{A.11})$$

where $\Delta = (\sigma_f^2 + \sigma_g^2)/\sigma_f^2$. We can see that the width of Eq. (A.11) w.r.t. p' is independent of p . Therefore, according to Eq. (A.8), the convolution of h and g is then to do a Fourier transformation from p' to $y - (\mu_f + \mu_g)$, giving us

$$(h * g)(y) = e^{i\frac{p}{\Delta}(y - \mu_f - \mu_g)} \exp\left[-\frac{(y - \mu_f - \mu_g)^2}{4(\sigma_f^2 + \sigma_g^2)} - \sigma_f^2 p^2 \left(1 - \frac{1}{\Delta}\right)\right]. \quad (\text{A.12})$$

Hence, the width w.r.t. y is $\sigma_f^2 + \sigma_g^2$, which is the same the width of $(f * g)(y)$ shown in Property 4. Moreover, when $\sigma_f = 1/\sigma_p$ and $\sigma_g = 2\sigma_x$, it follows $\Delta = 1 + 4\sigma_x^2\sigma_p^2$, which agrees with Eq. (3.13).

- **Property 6: In Table A.1 & A.2 we classify how the width would evolve after Fourier transformation, product of functions, convolution of real functions and convolution of complex functions as in “property 5”.** By the properties above, we summarize the width evolution of the first three types in the Table A.1, specifying its relation with the original function(s) and give the example of assuming all original functions are Gaussian distributed.

As for the last type, two functions are generated under such combination, namely, $H(y)$ and $I(p)$ in

$$\left| \int dx f(x) e^{ipx} g(x - y) \right| = H(y)I(p). \quad (\text{A.13})$$

By property 5, we see that the width of $H(y)$ and $I(p)$ has properties shown in Table A.2.

Appendix B

Factorization Condition

In this appendix, we derive the conditions under which a function can be factorized out of some integration, i.e.

$$\int_{-\infty}^{\infty} dX_2 S(X_2) Y(X_2; X_3) \simeq S(X_3) \int_{-\infty}^{\infty} dX_2 Y(X_2; X_3), \quad (\text{B.1})$$

where $S(X_2)$ and $Y(X_2; X_3)$ are both localized, i.e. $S(X_2) = Y(X_2) = 0$ as $X_2 \rightarrow \pm\infty$. This is useful for describing state decoherence as a phase wash-out effect on the Wigner-PS in Eq. (4.18), and disentangling σ_E and σ_L in Eq. (4.30). Intuitively, the condition where $S(X_2)$ can be factorized out of the integral as Eq. (B.1) is when the width of $S(X_2)$ is much larger than $Y(X_2)$, since the product of the two functions would be dominated by the function which is more localized. Nevertheless, in order to see if this condition is sufficient and to have a more concrete idea, we derive Eq. (B.1) as follows:

$$LHS = - \int_{-\infty}^{\infty} dX_2 \frac{dS(X_2)}{dX_2} \int_{-\infty}^{X_2} dX'_2 Y(X'_2; X_3) \quad (\text{B.2})$$

$$\simeq - \int_{X_3-\Lambda}^{\infty} dX_2 \frac{dS(X_2)}{dX_2} \int_{X_3-\Lambda}^{X_2} dX'_2 Y(X'_2; X_3) \quad (\text{B.3})$$

$$\begin{aligned} &\simeq - \int_{X_3-\Lambda}^{\infty} dX_2 \frac{dS(X_2)}{dX_2} \int_{-\infty}^{\infty} dX'_2 Y(X'_2; X_3) \\ &\quad + \int_{X_3-\Lambda}^{X_3+\Lambda} dX_2 \frac{dS(X_2)}{dX_2} \int_{X_2}^{X_3+\Lambda} dX'_2 Y(X'_2; X_3) = RHS. \end{aligned} \quad (\text{B.4})$$

Eq. (B.2) is achieved by doing integration by parts with the boundary terms vanishing due to the localization property of $S(X_2)$. In Eq. (B.3) and Eq. (B.4), we use the localization property of $Y(X_2)$ to make a cut at Λ w.r.t. X_3 such that the cumulative distribution function $\int_{-\infty}^{X_3-\Lambda} dX'_2 Y(X'_2; X_3) = 0$ and $\int_{-\infty}^{X_3+\Lambda} dX'_2 Y(X'_2; X_3)$ converges to a constant, so that $\int_{X_3+\Lambda}^{\infty} dX'_2 Y(X'_2; X_3) = 0$, as shown in Fig. B.1. Finally, if $S(X_2)$ varies slowly in the interval $(X_3 - \Lambda, X_3 + \Lambda)$, i.e. the width of $S(X_2)$ (σ_S), is much larger than that of $Y(X_2)$ (Λ),

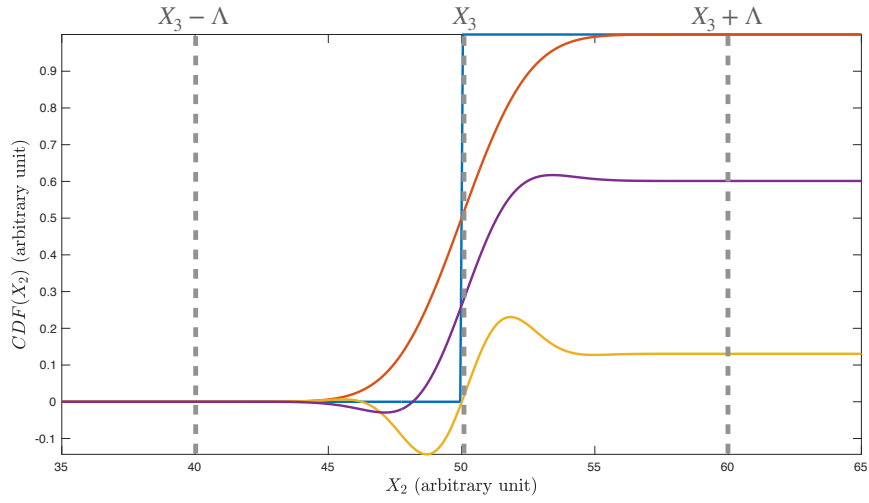


Figure B.1: The cumulative distribution function (CDF) of $Y(X_2; X_3 = 50)$ as a Gaussian PDF with width = 2 AU (arbitrary units of X_2), centered at 50 AU: $N(X_2)$ for the red line; a delta function centered at 50 AU for the blue line; and $N(X_2) \cos(X_2)/N(X_2) \cos(X_2/2)$ for the yellow/purple line; Λ is the cutoff value in Eq. (B.3).

then the latter part in Eq. (B.4) can be neglected and we arrive at the *RHS* of Eq. (B.1), where $S(X_3 - \Lambda) \rightarrow S(X_3)$ can be taken out of the integral if $X_3 \gg \Lambda$. Furthermore, $Y(X_2; X_3)$ could be any distribution as long as it is localized, even if it includes a non-zero phase term, as we can see from the orange and purple lines in Fig. B.1.

Appendix C

Phase Decoherence for Discrete Neutrino Sources

In this section, we show the formalism of phase decoherence effect including a damping term and a phase shift term for neutrino detection coming from multiple sources. In other words, we formulate the case where the weighting function on layer 2 for the coordinate uncertainty is composed of multiple delta functions discretely scattered. We start with the simple case where there are only two point-like sources located at x_1 and x_2 , contributing neutrino flux A and B , then the phase decoherence term in Eq. (4.27) is simply

$$\Phi_{jk} = e^{-i\alpha_{jk}L_3} (a e^{i\alpha_{jk}x_1} + b e^{i\alpha_{jk}x_2}) \equiv \phi^{(1)} e^{i\alpha_{jk}(x_{\text{eff}}^{(1)} - L_3)}, \quad (\text{C.1})$$

where $a = A/(A+B)$, $b = B/(A+B)$ and $0 \leq c \leq 1$, are real. This requires

$$A \sin(\alpha_{jk}\delta_1) + B \sin(\alpha_{jk}\delta_2) = 0, \quad (\text{C.2})$$

where $x_1 = x_{\text{eff}}^{(1)} + \delta_1$ and $x_2 = x_{\text{eff}}^{(1)} + \delta_2$. Hence, by solving Eq. (C.2) for $\Delta x^{(1)} = x_1 - x_2 = \delta_1 - \delta_2$, we have

$$\delta_1 \equiv f_{jk}(\Delta x, \frac{a}{b}) = \frac{1}{\alpha_{jk}} \tan^{-1} \left[\frac{-\sin(\alpha_{jk}\Delta x)}{\frac{a}{b} + \cos(\alpha_{jk}\Delta x)} \right], \quad (\text{C.3})$$

and thus

$$\begin{aligned} x_{\text{eff}}^{(1)} &= x_1 + f_{jk}(\Delta x^{(1)}, \frac{a}{b}), \\ \phi^{(1)} &= a \cos \left[\alpha_{jk} f_{jk}(\Delta x^{(1)}, \frac{a}{b}) \right] + b \cos \left[\alpha_{jk} (f_{jk}(\Delta x^{(1)}, \frac{a}{b}) + \Delta x^{(1)}) \right], \end{aligned} \quad (\text{C.4})$$

indicating that the damping term $\phi \leq 1$ as expected since $a + b = 1$. In the case where the detector is placed far from all the sources, $x_1, x_2 \gg \Delta x$, then $x_{\text{eff}} = x_2$, and $c = a + b \cos(\Delta x)$.

Similarly, if there are three point like neutrino sources,

$$\Phi_{jk} = e^{-i\alpha_{jk}L_3} (a e^{i\alpha_{jk}x_1} + b e^{i\alpha_{jk}x_2} + c e^{i\alpha_{jk}x_3}) \equiv \phi^{(2)} e^{i\alpha_{jk}(x_{\text{eff}}^{(2)} - L_3)}, \quad (\text{C.5})$$

the damping term ($\phi^{(2)}$) and the phase term ($x_{\text{eff}}^{(2)}$) are obtained by replacing $x_1 \rightarrow x_{\text{eff}}^{(1)}$, $\Delta x \rightarrow x_{\text{eff}}^{(1)} - x_3$, $a \rightarrow \phi^{(1)}$ and $b \rightarrow c$ in Eq. (C.4), and so on for more point-like sources.

Bibliography

- [1] Ting Cheng, Manfred Lindner, and Werner Rodejohann. Microscopic and macroscopic effects in the decoherence of neutrino oscillations. *JHEP*, 08:111, 2022.
- [2] Ting Cheng, Manfred Lindner, and Manibrata Sen. Implications of a matter-antimatter mass asymmetry in Penning-trap experiments. *Phys. Lett. B*, 844:138068, 2023.
- [3] Mohammad Sajjad Athar et al. Status and perspectives of neutrino physics. *Prog. Part. Nucl. Phys.*, 124:103947, 2022.
- [4] Florian Bonnet, Martin Hirsch, Toshihiko Ota, and Walter Winter. Systematic study of the d=5 Weinberg operator at one-loop order. *JHEP*, 07:153, 2012.
- [5] Ferruccio Feruglio. Pieces of the Flavour Puzzle. *Eur. Phys. J. C*, 75(8):373, 2015.
- [6] André De Gouvêa, Ivan Martinez-Soler, Yuber F. Perez-Gonzalez, and Manibrata Sen. Fundamental physics with the diffuse supernova background neutrinos. *Phys. Rev. D*, 102:123012, 2020.
- [7] Jun Wang et al. Damping signatures at JUNO, a medium-baseline reactor neutrino oscillation experiment. 12 2021.
- [8] Valentina De Romeri, Carlo Giunti, Thomas Stuttard, and Christoph A. Ternes. Neutrino oscillation bounds on quantum decoherence. *JHEP*, 09:097, 2023.
- [9] H. D. Zeh. On the interpretation of measurement in quantum theory. *Foundations of Physics*, 1:69–76, 1970.
- [10] Alexander Streltsov, Gerardo Adesso, and Martin B. Plenio. Quantum Coherence as a Resource. *Rev. Mod. Phys.*, 89:041003, 2017.
- [11] Maximilian Schlosshauer. Quantum Decoherence. *Phys. Rept.*, 831:1–57, 2019.
- [12] Wojciech Hubert Zurek. Decoherence, einselection, and the quantum origins of the classical. *Rev. Mod. Phys.*, 75:715–775, 2003.
- [13] Stefan Antusch, Jan Hajer, and Johannes Roskopp. Decoherence effects on lepton number violation from heavy neutrino-antineutrino oscillations. 7 2023.
- [14] Dimitrios Karamitros and Apostolos Pilaftsis. Toward a localized S-matrix theory. *Phys. Rev. D*, 108(3):036007, 2023.
- [15] G. Lindblad. On the generators of quantum dynamical semigroups. *Commun. Math. Phys.*, 48:119, 1976.

-
- [16] E. Lisi, A. Marrone, and D. Montanino. Probing possible decoherence effects in atmospheric neutrino oscillations. *Phys. Rev. Lett.*, 85:1166–1169, 2000.
- [17] Rasmus Sloth Lundkvist Hansen and Alexei Yu. Smirnov. The Liouville equation for flavour evolution of neutrinos and neutrino wave packets. *JCAP*, 12:019, 2016.
- [18] F. Benatti and R. Floreanini. Open system approach to neutrino oscillations. *JHEP*, 02:032, 2000.
- [19] Tobias Stirner, Günter Sigl, and Georg Raffelt. Liouville term for neutrinos: Flavor structure and wave interpretation. *JCAP*, 05:016, 2018.
- [20] João A. B. Coelho and W. Anthony Mann. Decoherence, matter effect, and neutrino hierarchy signature in long baseline experiments. *Phys. Rev. D*, 96(9):093009, 2017.
- [21] A. L. G. Gomes, R. A. Gomes, and O. L. G. Peres. Quantum decoherence and relaxation in neutrinos using long-baseline data. 1 2020.
- [22] Yasaman Farzan, Thomas Schwetz, and Alexei Yu Smirnov. Reconciling results of LSND, Mini-BooNE and other experiments with soft decoherence. *JHEP*, 07:067, 2008.
- [23] B. J. P. Jones. Dynamical pion collapse and the coherence of conventional neutrino beams. *Phys. Rev. D*, 91(5):053002, 2015.
- [24] E. P. Wigner. On the quantum correction for thermodynamic equilibrium. *Phys. Rev.*, 40:749, 1932.
- [25] Alexey Vlasenko, George M. Fuller, and Vincenzo Cirigliano. Neutrino Quantum Kinetics. *Phys. Rev. D*, 89(10):105004, 2014.
- [26] J. Rich. Quantum mechanics of neutrino oscillations. *Phys. Rev. D*, 48:4318–4325, Nov 1993.
- [27] C. Giunti and C. W. Kim. Coherence of neutrino oscillations in the wave packet approach. *Phys. Rev. D*, 58:017301, 1998.
- [28] Evgeny Kh. Akhmedov and Joachim Kopp. Neutrino Oscillations: Quantum Mechanics vs. Quantum Field Theory. *JHEP*, 04:008, 2010. [Erratum: *JHEP* 10, 052 (2013)].
- [29] Ken Kiers, Shmuel Nussinov, and Nathan Weiss. Coherence effects in neutrino oscillations. *Phys. Rev. D*, 53:537–547, 1996.
- [30] Boris Kayser. On the Quantum Mechanics of Neutrino Oscillation. *Phys. Rev. D*, 24:110, 1981.
- [31] Mikael Beuthe. Oscillations of neutrinos and mesons in quantum field theory. *Phys. Rept.*, 375:105–218, 2003.
- [32] C. Giunti. Neutrino wave packets in quantum field theory. *JHEP*, 11:017, 2002.
- [33] E. Kh. Akhmedov and A. Yu. Smirnov. Neutrino oscillations: Entanglement, energy-momentum conservation and QFT. *Found. Phys.*, 41:1279–1306, 2011.
- [34] Naumov V.A Naumov D.V. Quantum Field Theory of Neutrino Oscillations. *Phys. Part. Nuclei*, 51:1–106, 2020.
- [35] Walter Grimus. Revisiting the quantum field theory of neutrino oscillations in vacuum. *J. Phys. G*, 47(8):085004, 2020.
- [36] M. Blasone and Giuseppe Vitiello. Quantum field theory of fermion mixing. *Annals Phys.*, 244:283–311, 1995. [Erratum: *Annals Phys.* 249, 363–364 (1996)].

- [37] C. Giunti, C. W. Kim, and U. W. Lee. Remarks on the weak states of neutrinos. *Phys. Rev. D*, 45:2414–2420, Apr 1992.
- [38] Evgeny Akhmedov. Neutrino oscillations in matter: from microscopic to macroscopic description. *JHEP*, 02:107, 2021.
- [39] G. L. Sewell R. N. Sen. Fiber bundles in quantum physics. *J. Math. Phys.*, 43:1323–1339, 2002.
- [40] W. B. Case. Wigner functions and Weyl transforms for pedestrians. *Am.J.Phys.*, 76(10):937, 2008.
- [41] R. Jacob and R. G. Sachs. Mass and Lifetime of Unstable Particles. *Phys. Rev.*, 121:350, 1961.
- [42] Evgeny Akhmedov, Daniel Hernandez, and Alexei Smirnov. Neutrino production coherence and oscillation experiments. *JHEP*, 04:052, 2012.
- [43] Joern Kersten and Alexei Yu. Smirnov. Decoherence and oscillations of supernova neutrinos. *Eur. Phys. J. C*, 76(6):339, 2016.
- [44] M. Martini, M. Ericson, and G. Chanfray. Energy reconstruction effects in neutrino oscillation experiments and implications for the analysis. *Phys. Rev. D*, 87(1):013009, 2013.
- [45] Valentina De Romeri, Enrique Fernandez-Martinez, and Michel Sorel. Neutrino oscillations at DUNE with improved energy reconstruction. *JHEP*, 09:030, 2016.
- [46] Evgeny Kh. Akhmedov and Alexei Yu. Smirnov. Paradoxes of neutrino oscillations. *Phys. Atom. Nucl.*, 72:1363–1381, 2009.
- [47] Carlo Giunti and Chung W. Kim. Quantum mechanics of neutrino oscillations. *Found. Phys. Lett.*, 14(3):213–229, 2001.
- [48] Yasaman Farzan and Alexei Yu. Smirnov. Coherence and oscillations of cosmic neutrinos. *Nucl. Phys. B*, 805:356–376, 2008.
- [49] Andreu Esteban-Pretel, Sergio Pastor, Ricard Tomas, Georg G. Raffelt, and Gunter Sigl. Decoherence in supernova neutrino transformations suppressed by deleptonization. *Phys. Rev. D*, 76:125018, 2007.
- [50] Evgeny Akhmedov, Joachim Kopp, and Manfred Lindner. Collective neutrino oscillations and neutrino wave packets. *JCAP*, 09:017, 2017.
- [51] Dan Hooper, Dean Morgan, and Elizabeth Winstanley. Probing quantum decoherence with high-energy neutrinos. *Phys. Lett. B*, 609:206–211, 2005.
- [52] Ivan Esteban, M. C. Gonzalez-Garcia, Michele Maltoni, Thomas Schwetz, and Albert Zhou. The fate of hints: updated global analysis of three-flavor neutrino oscillations. *JHEP*, 09:178, 2020.
- [53] Andre de Gouvea, Valentina de Romeri, and Christoph Andreas Ternes. Probing neutrino quantum decoherence at reactor experiments. *JHEP*, 08:018, 2020.
- [54] André de Gouvêa, Valentina De Romeri, and Christoph A. Ternes. Combined analysis of neutrino decoherence at reactor experiments. *JHEP*, 06:042, 2021.
- [55] Thomas Stuttard and Mikkel Jensen. Neutrino decoherence from quantum gravitational stochastic perturbations. *Phys. Rev. D*, 102(11):115003, 2020.
- [56] Daniel Boriero, Dominik J. Schwarz, and Hermano Velten. Flavour composition and entropy increase of cosmological neutrinos after decoherence. *Universe*, 5(10):203, 2019.

- [57] Jose Carpio, E. Massoni, and A. M. Gago. Revisiting quantum decoherence for neutrino oscillations in matter with constant density. *Phys. Rev. D*, 97(11):115017, 2018.
- [58] J. A. Carpio, E. Massoni, and A. M. Gago. Testing quantum decoherence at DUNE. *Phys. Rev. D*, 100(1):015035, 2019.
- [59] G. Balieiro Gomes, D. V. Forero, M. M. Guzzo, P. C. De Holanda, and R. L. N. Oliveira. Quantum Decoherence Effects in Neutrino Oscillations at DUNE. *Phys. Rev. D*, 100(5):055023, 2019.
- [60] Pilar Coloma, Jacobo Lopez-Pavon, Ivan Martinez-Soler, and Hiroshi Nunokawa. Decoherence in Neutrino Propagation Through Matter, and Bounds from IceCube/DeepCore. *Eur. Phys. J. C*, 78(8):614, 2018.
- [61] L. Alvarez-Ruso et al. NuSTEC White Paper: Status and challenges of neutrino–nucleus scattering. *Prog. Part. Nucl. Phys.*, 100:1–68, 2018.
- [62] Boris Kayser and Joachim Kopp. Testing the Wave Packet Approach to Neutrino Oscillations in Future Experiments. 5 2010.
- [63] Mattias Blennow, Tommy Ohlsson, and Walter Winter. Damping signatures in future neutrino oscillation experiments. *JHEP*, 06:049, 2005.
- [64] P. A. Zyla et al. Review of Particle Physics. *PTEP*, 2020(8):083C01, 2020.
- [65] G. Bak et al. Measurement of Reactor Antineutrino Oscillation Amplitude and Frequency at RENO. *Phys. Rev. Lett.*, 121(20):201801, 2018.
- [66] S. H. Seo et al. Spectral Measurement of the Electron Antineutrino Oscillation Amplitude and Frequency using 500 Live Days of RENO Data. *Phys. Rev. D*, 98(1):012002, 2018.
- [67] J. K. Ahn et al. RENO: An Experiment for Neutrino Oscillation Parameter θ_{13} Using Reactor Neutrinos at Yonggwang. 3 2010.
- [68] K. Abe et al. Letter of Intent: The Hyper-Kamiokande Experiment — Detector Design and Physics Potential —. 9 2011.
- [69] Babak Abi et al. Deep Underground Neutrino Experiment (DUNE), Far Detector Technical Design Report, Volume II: DUNE Physics. 2 2020.
- [70] S. Ajimura et al. Technical Design Report (TDR): Searching for a Sterile Neutrino at J-PARC MLF (E56, JSNS2). 5 2017.
- [71] D. Baxter et al. Coherent Elastic Neutrino-Nucleus Scattering at the European Spallation Source. *JHEP*, 02:123, 2020.
- [72] J. Alonso et al. Expression of Interest for a Novel Search for CP Violation in the Neutrino Sector: DAEdALUS. 6 2010.
- [73] Roni Harnik, Kevin James Kelly, and Pedro A. N. Machado. Prospects of Measuring Oscillated Decay-at-Rest Neutrinos at Long Baselines. *Phys. Rev. D*, 101(3):033008, 2020.
- [74] Alessandro Strumia and Francesco Vissani. Precise quasielastic neutrino/nucleon cross-section. *Phys. Lett. B*, 564:42–54, 2003.
- [75] S. Ajimura et al. Proposal: JSNS²-II. 12 2020.
- [76] D. Akimov et al. First Measurement of Coherent Elastic Neutrino-Nucleus Scattering on Argon. *Phys. Rev. Lett.*, 126(1):012002, 2021.

- [77] A. Alekou et al. Updated physics performance of the ESSnuSB experiment: ESSnuSB collaboration. *Eur. Phys. J. C*, 81(12):1130, 2021.
- [78] E. Kolbe, K. Langanke, and P. Vogel. Estimates of weak and electromagnetic nuclear decay signatures for neutrino reactions in Super-Kamiokande. *Phys. Rev. D*, 66:013007, 2002.
- [79] Joachim Kopp, Toby Opferkuch, and Edward Wang. Magnetic Moments of Astrophysical Neutrinos. 12 2022.
- [80] Svenja Hummer, Philipp Baerwald, and Walter Winter. Neutrino Emission from Gamma-Ray Burst Fireballs, Revised. *Phys. Rev. Lett.*, 108:231101, 2012.
- [81] A. M. Hillas. The Origin of Ultra-High-Energy Cosmic Rays. *ARA&A*, 22:425–444, January 1984.
- [82] Jörg P. Rachen and P. Mészáros. Photohadronic neutrinos from transients in astrophysical sources. *Phys. Rev. D*, 58(12):123005, December 1998.
- [83] S. Hummer, M. Maltoni, W. Winter, and C. Yaguna. Energy dependent neutrino flavor ratios from cosmic accelerators on the Hillas plot. *Astropart. Phys.*, 34:205–224, 2010.
- [84] S. Hümmer, M. Maltoni, W. Winter, and C. Yaguna. Energy dependent neutrino flavor ratios from cosmic accelerators on the Hillas plot. *Astroparticle Physics*, 34(4):205–224, November 2010.
- [85] Peter Goldreich and William H. Julian. Pulsar Electrodynamics. *ApJ*, 157:869, August 1969.
- [86] M. A. Ruderman and P. G. Sutherland. Theory of pulsars: polar gaps, sparks, and coherent microwave radiation. *ApJ*, 196:51–72, February 1975.
- [87] Bing Zhang, Z. G. Dai, and P. Meszaros. High-energy neutrinos from magnetars. *Astrophys. J.*, 595:346–351, 2003.
- [88] S. Hümmer, M. Rügner, F. Spanier, and W. Winter. Simplified Models for Photohadronic Interactions in Cosmic Accelerators. *ApJ*, 721(1):630–652, September 2010.
- [89] Jonathan Arons. Magnetars in the Metagalaxy: An Origin for Ultra-High-Energy Cosmic Rays in the Nearby Universe. *ApJ*, 589(2):871–892, June 2003.
- [90] Jose Alonso Carpio, Kohta Murase, Mary Hall Reno, Ina Sarcevic, and Anna Stasto. Charm contribution to ultrahigh-energy neutrinos from newborn magnetars. *Phys. Rev. D*, 102(10):103001, November 2020.
- [91] Bennett Link and Fiorella Burgio. TeV μ Neutrinos from Young Neutron Stars. *Phys. Rev. Lett.*, 94(18):181101, May 2005.
- [92] Bennett Link and Fiorella Burgio. Flux predictions of high-energy neutrinos from pulsars. *MNRAS*, 371(1):375–379, September 2006.
- [93] Soebur Razzaque, Peter Mészáros, and Eli Waxman. TeV Neutrinos from Core Collapse Supernovae and Hypernovae. *Phys. Rev. Lett.*, 93(18):181101, October 2004.
- [94] Katsuaki Asano. Cooling of Accelerated Nucleons and Neutrino Emission in Gamma-Ray Bursts. *ApJ*, 623(2):967–972, April 2005.
- [95] T. Piran. Gamma-ray bursts and the fireball model. *Phys. Rep.*, 314(6):575–667, June 1999.
- [96] G. Q. Li, C. H. Lee, and G. E. Brown. Kaons in dense matter, kaon production in heavy-ion collisions, and kaon condensation in neutron stars. *Nucl. Phys. A*, 625:372–434, February 1997.

- [97] Eli Waxman and John Bahcall. High Energy Neutrinos from Cosmological Gamma-Ray Burst Fireballs. *Phys. Rev. Lett.*, 78(12):2292–2295, March 1997.
- [98] Kohta Murase and Shigehiro Nagataki. High energy neutrino emission and neutrino background from gamma-ray bursts in the internal shock model. *Phys. Rev. D*, 73(6):063002, March 2006.
- [99] Shigeo S. Kimura, Kohta Murase, Peter Mészáros, and Kenta Kiuchi. High-energy Neutrino Emission from Short Gamma-Ray Bursts: Prospects for Coincident Detection with Gravitational Waves. *ApJ*, 848(1):L4, October 2017.
- [100] Hao-Ning He, Ruo-Yu Liu, Xiang-Yu Wang, Shigehiro Nagataki, Kohta Murase, and Zi-Gao Dai. Icecube Nondetection of Gamma-Ray Bursts: Constraints on the Fireball Properties. *ApJ*, 752(1):29, June 2012.
- [101] G. J. Alner, K. Alpgård, P. Anderer, R. E. Ansorge, B. Åsman, K. Böckmann, C. N. Booth, L. Burow, P. Carlson, J. L. Chevalley, C. Declercq, R. S. Dewolf, B. Eckart, G. Ekspong, I. Evangelou, A. Eyring, J. P. Fabre, K. A. French, L. Fröbel, J. Gauden, C. Geich-Gimbel, M. Gijssen, K. Von Holt, R. Hospes, D. Johnson, K. Jon-And, Th. Kokott, M. Langer, R. Meinke, Th. Müller, D. J. Munday, J. E. V. Ovens, J. G. Rushbrooke, H. Schmickler, F. Triantis, L. Van Hamme, Ch. Walck, C. P. Ward, D. R. Ward, T. O. White, G. Wilquet, N. Yamdagni, and UA5 Collaboration. Multiplicity distributions in different pseudorapidity intervals at a CMS energy of 540 GeV. *Physics Letters B*, 160(1-3):193–198, October 1985.
- [102] Clark S. Lindsey, T. Alexopoulos, C. Allen, E. W. Anderson, V. Balamurali, S. Banerjee, P. D. Beery, P. Bhat, N. N. Biswas, A. Bujak, D. D. Carmony, T. Carter, P. Cole, Y. Choi, R. DeBonte, V. DeCarlo, A. R. Erwin, C. Findeisen, A. T. Goshaw, L. J. Gutay, A. S. Hirsch, C. Hojvat, J. R. Jennings, V. P. Kenny, C. S. Lindsey, C. Loomis, J. M. LoSecco, T. McMahon, A. P. McManus, N. Morgan, K. Nelson, S. H. Oh, N. T. Porile, D. Reeves, A. Rimai, W. J. Robertson, R. P. Scharenberg, B. C. Stringfellow, S. R. Stampke, M. Thompson, F. Turkot, W. D. Walker, C. H. Wang, J. Warchol, D. K. Wesson, Y. Zhan, and E735 Collaboration. Results from E735 at the tevatron proton-antiproton collider with $\sqrt{s} = 1.8$ TeV. *Nucl. Phys. A*, 544(1):343–356, July 1992.
- [103] Shin’ichiro Ando and John F. Beacom. Revealing the Supernova Gamma-Ray Burst Connection with TeV Neutrinos. *Phys. Rev. Lett.*, 95(6):061103, August 2005.
- [104] K. Asano and S. Nagataki. Very High Energy Neutrinos Originating from Kaons in Gamma-Ray Bursts. *ApJ*, 640(1):L9–L12, March 2006.
- [105] Kohta Murase, Peter Mészáros, and Bing Zhang. Probing the birth of fast rotating magnetars through high-energy neutrinos. *Phys. Rev. D*, 79(10):103001, May 2009.
- [106] E. Amato, D. Guetta, and P. Blasi. Signatures of high energy protons in pulsar winds. *A&A*, 402:827–836, May 2003.
- [107] Ke Fang and Brian D. Metzger. High-Energy Neutrinos from Millisecond Magnetars formed from the Merger of Binary Neutron Stars. *Astrophys. J.*, 849(2):153, 2017.
- [108] M. G. Aartsen et al. IceCube Search for High-Energy Neutrino Emission from TeV Pulsar Wind Nebulae. *Astrophys. J.*, 898(2):117, 2020.
- [109] Shigeo S. Kimura, Kohta Murase, Imre Bartos, Kunihito Ioka, Ik Siong Heng, and Peter Mészáros. Transejecta high-energy neutrino emission from binary neutron star mergers. *Phys. Rev. D*, 98(4):043020, 2018.

-
- [110] Kohta Murase and Kunihiro Ioka. TeV-PeV Neutrinos from Low-Power Gamma-Ray Burst Jets inside Stars. *Phys. Rev. Lett.*, 111(12):121102, September 2013.
- [111] M. G. Aartsen et al. Measurements using the inelasticity distribution of multi-TeV neutrino interactions in IceCube. *Phys. Rev. D*, 99(3):032004, 2019.
- [112] Kohta Murase, Kazumi Kashiyama, and Peter Mészáros. Subphotospheric Neutrinos from Gamma-Ray Bursts: The Role of Neutrons. *Phys. Rev. Lett.*, 111(13):131102, September 2013.
- [113] Kohta Murase, Mainak Mukhopadhyay, Ali Kheirandish, Shigeo S. Kimura, and Ke Fang. Neutrinos from the Brightest Gamma-Ray Burst? *arXiv e-prints*, page arXiv:2210.15625, October 2022.
- [114] H. Sotani, A. Colaiuda, and K. D. Kokkotas. Constraints on the magnetic field geometry of magnetars. *MNRAS*, 385(4):2161–2165, April 2008.
- [115] Hao-Jui Kuan, Arthur G. Suvorov, and Kostas D. Kokkotas. General-relativistic treatment of tidal g-mode resonances in coalescing binaries of neutron stars – I. Theoretical framework and crust breaking. *Mon. Not. Roy. Astron. Soc.*, 506(2):2985–2998, 2021.
- [116] A. Mastrano, P. D. Lasky, and A. Melatos. Neutron star deformation due to multipolar magnetic fields. *MNRAS*, 434(2):1658–1667, September 2013.
- [117] A. G. Suvorov and K. D. Kokkotas. Young magnetars with fracturing crusts as fast radio burst repeaters. *MNRAS*, 488(4):5887–5897, October 2019.
- [118] M. G. Aartsen et al. Detection of a particle shower at the Glashow resonance with IceCube. *Nature*, 591(7849):220–224, 2021. [Erratum: *Nature* 592, E11 (2021)].
- [119] M. G. Aartsen et al. IceCube-Gen2: the window to the extreme Universe. *J. Phys. G*, 48(6):060501, 2021.
- [120] Raphael Krueger and Thomas Schwetz. Decoherence effects in reactor and Gallium neutrino oscillation experiments: a QFT approach. *Eur. Phys. J. C*, 83(7):578, 2023.
- [121] Evgeny Akhmedov and Alexei Y. Smirnov. Damping of neutrino oscillations, decoherence and the lengths of neutrino wave packets. *JHEP*, 11:082, 2022.
- [122] A. Bodek and J. L. Ritchie. Fermi Motion Effects in Deep Inelastic Lepton Scattering from Nuclear Targets. *Phys. Rev. D*, 23:1070, 1981.